University of Science and Technology of China

Hefei, CHINA

J/ψ production at high transverse momentum in $p+p$ and A+A collisions

A dissertation submitted

for the degree of

Doctor of Philosophy in Physics

by

Zebo Tang

唐泽波

Co-supervisors: Cheng Li and Zhangbu Xu

2009

Dedicated to my family

Acknowledgments

First of all, my gratitude goes to Prof. Cheng Li and Hongfang Chen. They have been my adviser since I was a undergraduate student. They gave me a very good start on the high energy physics and continue to supervise and support me in the last six years. I would like to thank Dr. Timothy Hallah, Prof. Zhangbu Xu and the China Scholarship Council for offering the opportunity to work at BNL, the wonderful place for relativistic heavy-ion physics research. I am greatly thankful for Zhangbu's help. He is the co-adviser of my PhD research. He guided me through all the detailed analysis in my research. I am very impressed by his enormous physics knowledge, enthusiasm on the research and numerous ideas. I benefits a lot from his guidance and tons of fruitful discussions with him.

My special thanks goes to Dr. Xin Dong, who introduced me into this heavy-ion physics filed and guided me for two years on my K^* analysis. My special thanks also goes to Dr. Lijuan Ruan. She and her husband Shengli Huang help me a lot on my research and living at BNL. I would like to thank my classmate Yichun Xu for enjoyable corporation on work and living and abundant helpful discussions.

I appreciate many assistances from the STAR group at BNL, especially Prof. Thomas Ullrich, for valuable discussions. I also appreciate many assistances from the High Energy Physics Group at USTC, especially Prof. Zizong Xu, Prof. Xiaolian Wang, Prof. Ziping Zhang, Prof. Qun Wang, Prof. Ming Shao, Mr. Hui Zeng, Dr. Yongjie Sun, Dr. Shaohui An, Dr. Yan'e Zhao, Mr. Yi Zhou, Ms. Congrong Wang.

I would like to thank the STAR Spectra and Heavy Flavor physics working group especially the convenors. Thank all other STAR collaborators for providing beautiful detector performance and data. I also thank Dr. Nu Xu, Prof. Fuqiang Wang, Dr. Bedanga Mohanty, Prof. Huan.Z. Huang and Dr. Aihong Tang for many helpful suggestions.

I would like to thank all my friends for their support. Without you, the life is meaningless. I would like to thank all the physicists who I met and discussed with.

Finally, I express my deep gratitude to my family. I'll never forget tens of years of unceasing self-giving sacrifices from my parents. I'll never forget continuous support and understanding from my sisters.

Abstract of the Dissertation

J/ψ production at high transverse momentum in $p+p$ and A+A collisions

by

Zebo Tang

唐泽波

Doctor of Philosophy in Physics

University of Science and Technology of China, Hefei, 2009

A Quark-Gluon Plasma (QGP) is believed to have existed before the universe cooled and free quarks and gluons combined into protons and neutrons, which then bound together to form light nuclei. Lattice QCD calculations predict a phase transition from hadronic matter to the deconfined and locally thermalized QGP state at high temperature and small baryon density. The Relativistic Heavy Ion Collider (RHIC) is built to search for the QGP in laboratory through the high energy heavy ion collisions. Suppression of the $c\bar{c}$ bound state J/ψ meson production in relativistic heavy-ion collisions arising from J/ψ dissociation due to color screening of the $c\bar{c}$ binding potential in the deconfined medium has been proposed as a signature of QGP formation.

Beside the color screening effect, other mechanisms may contribute to the J/ψ suppression in heavy-ion collisions. For example, the decreasing J/ψ suppression with increasing p_T observed in $Pb+Pb$ collisions at $\sqrt{s_{NN}} = 17.3$ GeV at CERN-SPS can be explained by initial state effects of finite J/ψ formation time and the finite space time extent of the hot dense medium. At higher beam energy, RHIC observes similar J/ψ suppression at lower p_T at 200 GeV Au + Au and Cu + Cu collisions with that at CERN-SPS, even though the energy density is significant higher at RHIC. This may be due to the counter-balancing of dissociation by the recombination of thermal c and $\bar{c}$ in the medium, which are abundant at higher energy. The strong suppression of non-photonic electrons from

heavy-flavor decay observed at RHIC suggests that the J/ψ may be also suppressed due to loss energy in the medium if its formation proceeds through a channel carrying color.

The medium generated in RHIC heavy-ion collisions is thought to be strongly coupled, making accurate QCD calculations of quarkonium propagation difficult. The AdS/CFT duality for QCD-like theories may provide insight into heavy fermion pair propagating in a strongly coupled liquid. One such calculation predicts that the dissociation temperature decreases with increasing J/ψ p_T (or velocity). The temperature achieved at RHIC (~ 1.5 T_c) is below this dissociation temperature at low J/ψ p_T, and above it at $p_T \gtrsim 5$ GeV/c. Consequently, J/ψ production is predicted to be more suppressed at high p_T, in contrast to the standard suppression mechanism. This prediction can be tested with measurements of J/ψ over a broad kinematic range, in both $p+p$ and nuclear collisions.

The interpretation of J/ψ suppression observed at the SPS and by the PHENIX collaboration requires understanding of the quarkonium production mechanisms in hadronic collisions, which include direct production via gluon fusion and color-octet (CO) and color-singlet (CS) transitions, as described by Non-Relativistic Quantum ChromoDynamics (NRQCD); parton fragmentation; and feeddown from higher charmonium states (χ_c, $\psi(2S)$) and B meson decays. No model at present day fully explains the J/ψ systematics observed in elementary collisions. J/ψ measurements at high-p_T both in $p+p$ and nuclear collisions may provide additional insights into the basic processes underlying quarkonium production.

In this thesis, we reports the measurement of J/ψ in high transverse momentum in $p+p$ and Cu + Cu collisions at $\sqrt{s_{NN}} = 200$ GeV at STAR. The inclusive cross section and J/ψ-hadron correlations are presented.

The high-p_T J/ψ is reconstructed through the $J/\psi \rightarrow e^+e^-$ channel (Branching ratio = 5.9%). One electron daughter is triggered online by the Barrel Electromagnetic Calorimeter by requiring its deposit energy above certain threshold. This trigger enriches the high p_T electron sample. The electron identification for this triggered electron is provide by the combination of ionization energy loss dE/dx measured by the Time Projection

Chamber (TPC), shower energy measured by the BEMC and shower shape measured by the Barrel Shower Maximum Detector (BSMD). Its purity is > 70 % with high efficiency. The other electron daughter has no BEMC trigger requirement. It is identified by using the dE/dx alone. This J/ψ reconstruction method allows us to measurement the J/ψ at high p_T ($p_T > 5$ GeV/c) with good signal to background (S/B) ratio. The J/ψ cross section at high-p_T is extracted using RHIC 2005 $p+p$ and Cu + Cu data and RHIC 2006 $p+p$ data, and compared to model calculations. Its x_T scaling behavior is also tested. We found the J/ψ production in $p+p$ collisions obey x_T scaling at $p_T \gtrsim 5$ GeV/c with power value $n = 5.6 \pm 0.2$. The low p_T J/ψ significantly deviates the x_T scaling, suggesting the soft process could affect the J/ψ production at low p_T although it must originate from a hard process due to the mass scale.

The J/ψ nuclear modification factor R_{AA} in Cu + Cu is found to increase from low to high p_T. The average of R_{AA} at $p_T > 5$ GeV/c is $1.4 \pm 0.4(stat.) \pm 0.2(syst.)$ and is $1.1 \pm 0.3 \pm 0.2$ from combined RHIC data. This is consistent with no J/ψ suppression, in contrast to the prediction from a theoretical model of quarkonium dissociation in a strongly coupled liquid using an AdS/CFT approach. The two-component model including color screening, hadronic phase dissociation, statical $c\bar{c}$ coalescence at the hadronization transition, J/ψ formation time and B-meson feeddwon can describe the overall trend of the data.

Thanks to the high S/B ratio, we measured the azimuthal correlation between high p_T J/ψ and charged hadrons. We observed an absence of charged hadrons accompanying high p_T J/ψ on the near side, in contrast to the dihadron correlation. From comparison with the model simulations, we estimate the fraction of J/ψ from B-meson decay to be $13 \pm 5\%$ at $p_T > 5$ GeV/c.

中文摘要

RHIC能区高横动量J/ψ 产生

唐泽波

中国科学技术大学，2009 年6 月

宇宙大爆炸理论认为在宇宙形成的最初阶段存在一种极其特殊的物质形态–夸克胶子等离子体(QGP)。格点量子色动力学预言在高温和低重子密度的条件下会产生从普通的强子物质到这种夸克解紧闭、局部达到热平衡的夸克胶子等离子体的相变。位于美国布鲁克海汶国家实验室(BNL)的相对论重离子对撞机(RHIC)是目前最高能量的重离子对撞机，其通过极高能的重离子束流对撞来寻找QGP并研究其特性。在这种解紧闭的物质中，粲夸克和其反夸克组成的束缚态J/ψ中夸克和反夸克之间的作用力会由于色荷的德拜屏蔽而降低从而使得J/ψ束缚态不复存在。因此，J/ψ在相对论重离子对撞中产额的抑制是QGP形成的一个非常重要的信号。

然而除了色荷屏蔽会造成J/ψ的产额降低外，还有一些其它的效应会造成类似的影响。例如，CERN-SPS 17.3 GeV 铅核-铅核对撞中观测到的J/ψ的产额抑制的程度随着动量的增加而减少的趋势可以用J/ψ的形成时间这一初始状态的效应来解释。在更高能量–RHIC能区的200 GeV 金核-金核和铜核-铜核对撞中，尽管RHIC能区产生的物质的能量密度要高得多，低横动量的J/ψ的产额抑制和CERN-SPS的测量结果非常类似。可能的解释是:1)RHIC能区产生的热化的粲夸克及其反夸克在热力学冻结附近会再组合成J/ψ从而部分抵消由于色荷屏蔽造成的产额的抑制；2) 目前观测到的J/ψ的抑制都来自高阶的粲夸克和其反夸克的束缚态例如ψ'和χ_c, CERN和RHIC产生的物质的温度都能使得这些态分解而都不能使得直接产生的J/ψ分解。对于高横动量的J/ψ, 其再组合产生的比重会与低横动量有所差异，更重要的是，最近的AdS/CFT理论计算表明直接产生的J/ψ的分解温度会随着动量的增加而减少。在5 GeV/c以上，J/ψ的分解温度会降低到RHIC达到的温度。因此高横动量的J/ψ的测量能对J/ψ 的产额抑制机制的研究以

及QGP的寻找和特性的研究提供独特而又极为重要的帮助。

事实上，在J/ψ被发现的20多年后，人们对其产生机制依然不是非常清楚。目前人们认为其可能的来源为：1）通过色单态或是色八重态的粲夸克和其反夸克对的直接产生；2）部分子的碎裂过程；3）高阶粲偶素和B粒子的衰变。目前没有任何一个模型能完全解释基本粒子对撞中产生的J/ψ的特性。质子-质子和原子核对撞产生的高横动量的J/ψ的测量会给J/ψ产生机制的研究提供额外的信息。

本文在RHIC能区首次测量了高横动量J/ψ在200 GeV 质子-质子和铜核-铜核对撞中的产生。我们通过$J/\psi \to e^+e^-$ 来重建J/ψ. 其中一个高能的电子由电磁量能器触发。该触发系统能大大提高高能电子的产额从来提高记录到的亮度。对于这种电子，我们通过综合利用时间投影谱仪测量到的电磁能损(dE/dx)和电磁量能器提供的总能量以及电磁簇射的形状来鉴别。该种鉴别方法高效地提供很纯的高能电子样本。对于另外一个电子，我们挑选能量稍微低一些的可以直接由时间投影谱仪单独鉴别的电子以提高重建效率。通过这种重建方法，我们得到了高信噪比的、高横动量的J/ψ。并进而得到了其微分产生截面，和模型其进行了比较，测试了x_T标度。我们发现横动量高于5 GeV/c的J/ψ遵循x_T标度，其指数为$n = 5.6 \pm 0.2$。而低横动量的J/ψ违背这一标度，该发现表明，尽管低横动量的J/ψ必然来源于硬过程，但是软过程能会影响J/ψ的产生。

我们发现铜核-铜核对撞中J/ψ的核修正因子R_{AA}随着横动量的增长而增长。其在5 GeV/c以上的平均值为$1.4 \pm 0.4 \pm 0.2$。这表明J/ψ产额没有抑制，与AdS/CFT的理论预言正好相反。而2-component模型能解释这一趋势。

由于高信噪比，我们在RHIC能区首次测量了高横动量J/ψ和带电强子之间的方位角关联。我们发现在高横动量J/ψ附近几乎没有带电强子产生，这与强子-强子的关联结果完全不一样。通过与模型作比较，我们得到了在高横动量区，B介子对总的J/ψ的贡献为$13\% \pm 5\%$。

Table of Contents

List of Figures

List of Tables

CHAPTER 1

Introduction

1.1 Standard Model and Quantum Chromo-Dynamics

1.1.1 Standard Model

The Standard Model (SM) of particle physics is a theory of three known fundamental interactions (strong, weak and electromagnetic interactions) and the elementary particles that take part in these interactions. It is a simple and comprehensive theory that explains all of hundreds of particles and complex interactions. It is well confirmed by the experiments, for example the discovery of W and Z bosons and the precise measurements on their masses.

The Standard Model is a Lagrangian Quantum Filed Theory based upon the idea of local gauge invariance. The gauge symmetry group of the Standard Model is $SU(3)_C \times SU(2)_L \times U(1)_Y$. $SU(3)_C$ is the symmetry group describing the strong interactions, whereas $SU(2)_L \times U(1)_Y$ represents the symmetry group of the electro-weak sector describing the weak and electromagnetic interactions.

The particle content of the model may be broadly classified in terms of two groups, namely the fundamental fermions and the gauge vector bosons. The fermions are defined as elementary particles having spin = 1/2. There are 12 known fermions, each with a corresponding antiparticle. They are 6 quarks (up (u), down (d), charm (c), strange (s), top (t) and bottom (b)) and 6 leptons (electron (e), muon (μ), tauon (τ), and their corresponding neutrinos). Pairs from each classification are grouped together to form a generation as shown in Fig 1.1, with corresponding particles exhibiting similar

physical behavior.

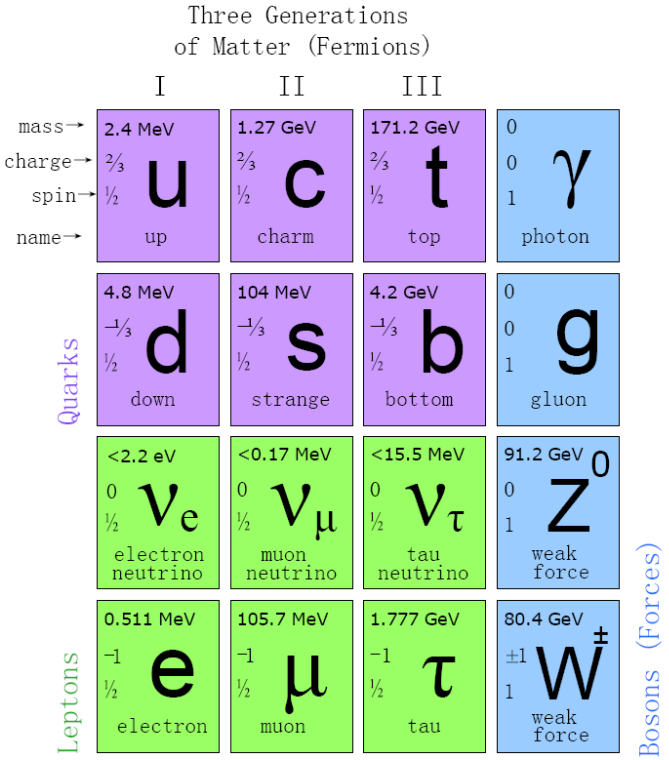

Figure 1.1: Particle content in the Standard Model.

The defining property of the quarks is that they carry color charge, and hence, interact via the strong force. Quarks also carry electric charge and weak isospin. Hence they also interact with other fermions both electromagnetically and via the weak nuclear interaction.

The remaining six fermions do not carry color charge. e, μ and τ carries electric charge thus interact electromagnetically. The three neutrinos do not carry electric charge so their motion is directly influenced only by the weak nuclear force.

The forces between these fermions are mediated by the gauge vector bosons (the last column of Fig. 1.1). The electromagnetic force between electrically charged particles is mediated by photons, which is massless and well described by the theory of quantum electrodynamics (QED). The weak interactions between particles of different flavors are mediated the massive gauge bosons $W^{\pm}$ and Z. The strong or color force interaction between quarks is described in terms of the gauge particles of $SU(3)_C$. These gauge

vector bosons are $3^2 - 1 = 8$ in number and are called gluons. These eightfold multiplicity of gluons is labelled by a combination of color and an anticolor charge. Because the $SU(3)_C$ symmetry of the color interaction is believed to be exact, the gluons are massless particles. The effective color charge of gluons allow them to interact among themselves. The gluons and their interactions are described by the theory of quantum chromodynamics (QCD).

1.1.2 Quantum Chromo-Dynamics

QCD is introduced by Gell-Mann and Fritzsch in 1972 [FG72]. It is a renormalizable nonabelian gauge theory based on the ground $SU(3)_C$ to describe the strong interaction. It Lagrangian can be written as:

$$\mathcal{L}_{QCD} = -\frac{1}{4} F^{(a)}_{\mu\nu} F^{(a)\mu\nu} + i \sum_q \bar{\psi}^i_q \gamma^\mu (D_\mu)_{ij} \psi^j_q - \sum_q m_q \bar{\psi}^i_q \psi_q i, \tag{1.1}$$

$$F^{(a)\mu\nu} = \partial A^a_\nu - \partial A^a_\mu - g_s f_{abc} A^b_\mu A^b_\nu, \tag{1.2}$$

$$(D_\mu)_{ij} = \delta_{ij} \partial_\mu + i g_s \sum_a \frac{\lambda^a_{i,j}}{2} A^a_\mu, \tag{1.3}$$

where g_s is the QCD coupling constant, and the f_{abc} are the structure constants of the $SU(3)_C$ algebra, The $\psi^i_q(x)$ are the 4-component Dirac spinors associated with each quark filed of(3) color i and flavor q, and the $A^a_\mu(x)$ are the (8) Yang-Mills (gluon) filed.

QCD has two peculiar properties: 1) Asymptotic freedom; and 2) Confinement.

1.1.2.1 Asymptotic freedom

The effective QCD coupling constant $\alpha_s = g_s^2/4\pi$ is dependent on the renormalization scale, similar to that in QED (running coupling). It can be written as:

$$\alpha_s(\mu) \approx \frac{4\pi}{\beta_0 \ln(\mu^2/\Lambda^2_{QCD})}, \tag{1.4}$$

where β_0 is a constant dependent on the number of quarks with mass less than μ and Λ_{QCD} is one of the important QCD parameters. Unlike the QED effective coupling which is increase with the energy scale μ, the QCD effective coupling α_s is opposite. $\alpha_s \to 0$ as $\mu \to \infty$ and QCD becomes strongly coupled at $\mu \sim \Lambda_{QCD}$. The α_s has to be determined from experiment. The world average α_s at common energy scale $\mu = M_Z$ is $\alpha_s(M_Z) = 0.1176 \pm 0.002$, and the QCD scale $\Lambda_{QCD} \sim 200$ MeV. Figure 1.2 shows α_s at different momentum transfer scale [Ams08].

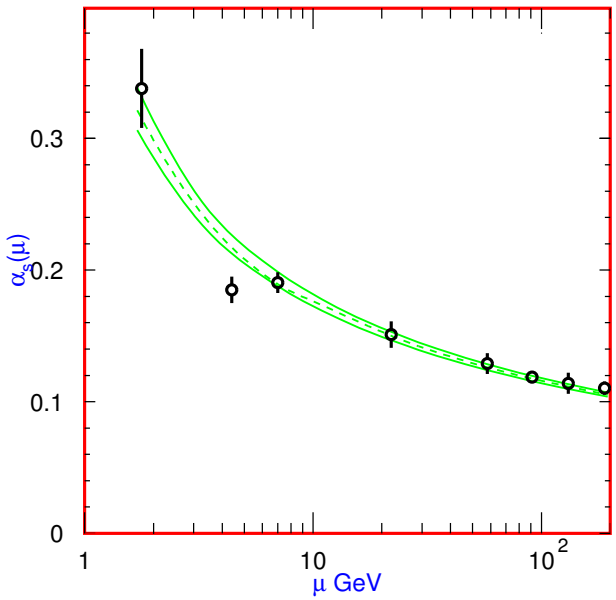

Figure 1.2: QCD effective coupling α_s as a function of momentum transfer scale μ. The figure is taken from [Ams08]

Due to the asymptotic freedom, the QCD is handled with different method at different energy scale. The QCD can only be calculated perturbatively in high momentum transfer or short distance approach (pQCD). At the strong coupling case, pQCD is irrelevant and some other methods are needed, for example Lattice QCD and AdS/CFT.

pQCD Since at high momentum transfer, the $\alpha_s \ll 1$ and decrease logarithmically (very slowly), physics quantities, such as cross sections, can be calculated to a truncated series with different α_s dependence (α_s^{n+2}). Since α_s is very small, the terms with lowest

power n ($n = 0$) is usually have the largest contribution and called *Leading order (LO)*. The higher order terms usually have smaller contribution and involves more complicate diagrams which cause the calculation more difficult. Depend on the power n, the corrections are called *Next-to-Leading Order (NLO)*, $n = 1$, *Next-to-Next-to-Leading Order (NNLO)*, $n = 2$, etc.

But this is only on parton level, for the process on hadron level, the hadron structure which involved nonperturbative nature has to be take into account. A QCD *factorization theorem* was develop to calculate the cross section on hadron level, which separate the cross section into 2 parts: the process dependent pQCD calculate short distance parton cross section, and the universal long distance functions. For example, the cross section for a process $A + B \to C + ...$ where A, B and C are hadrons, can be written as:

$$\sigma_{AB\to C} = f_{a/A}(x_a, \mu_F^2) f_{b/B}(x_b, \mu_F^2) \otimes \hat{\sigma}_{ab\to c}(\hat{s}, \mu_F^2, \mu_R^2, \alpha_s) \otimes D_{c\to C}(z, \mu_F^2). \tag{1.5}$$

Only the middle term $\hat{\sigma}_{ab\to c}$, the parton cross section, can be calculated in pQCD from Feynman diagrams. The first term $f_{a/A}(x_a, \mu_F^2)$ or$f_{b/B}(b_a, \mu_F^2)$ is the hadron *Parton Distribution Function* (PDF) and the last term $D_{c\to C}(z, \mu_F^2)$ is the *Fragmentation Function* (FF) that describes the transition from a parton to a hadron. For leptons, these two terms do to contribute in this formula. Hence, we can measure PDFs through lepton-nucleon DIS interactions and FFs through high energy e^+e^- collisions. μ_R is the renormalization scale, originate from the need to regularize divergent momentum integrals in calculating high order diagram loops. μ_F is the factorization scale, at which the parton density are evaluated. $\hat{s}$ is the partonic center of mass energy squared.

Lattice QCD At low momentum transfer, the QCD coupling constant α_s approach unity quickly as decreasing momentum transfer. In this case the high order processes will have large contributions and can not be neglected. The pQCD is not valid any more. Instead, the Lattice QCD is the most well established approach in this case. In

Lattice QCD, space time is represented not as continuous but as a crystalline lattice, vertices connected by lines. Quarks may reside only on vertices and gluons can only travel along lines. As the spacing between vertices is reduced to zero, the theory will approach continuum QCD. As this is computationally impossible, lattice QCD calculations often involved analysis at different lattice spacing to determine the lattice-spacing dependence, which can then be extrapolated to the continuum. This technique is only applicable in the domain of low density and high temperature. At higher densities, the fermion sign problem renders the results useless.

Other Non Perturbative QCD There are some other non perturbative methods in the market, such as 1/N expansion and Effective theories. The 1/N expansion, a well known approximate scheme, starts from the premise that the number of colors is infinite, and makes a series of corrections to account for the fact that it is not. The AdS/CFT (anti-de-Sitter space/conformal field theory) is one of the popular 1/N expansions. It is the conjecture equivalence between a string theory defined on one space, and a quantum filed theory without gravity defined on the conformal boundary of this space, whose dimension is lower by one or more. An example is the duality between Type IIB string theory on $AdS_5 \times S^5$ space (a product of give dimensional AdS space with a five dimensional sphere) and a supersymmetric $\mathcal{N} = 4$ Yang-Mills gauge theory (which is a conformal field theory) on the 4-dimensional boundary of AdS_5.

In some specific case, the QCD Lagrangian can be systematically expanded in some parameters. For example the heavy quark effective theory which expands around heavy quark mass near infinity.

1.1.2.2 Confinement

Isolated quarks have never been observed, as particle with fractional electric charge, for example. While all of the hadrons are found to be in color neutral states. Nowadays, people believe that the quarks with color are confined into hadrons, no free quarks and/or colors can be observed. This is why quarks can never be studied in any more

direct way that at a hadron level.

The reason for quark/color confinement are somewhat complicate. There is no analytic proof that QCD should be confining, but intuitively confinement is due to the force-carrying gluons having color charge. As any two electrically-charge particles separate, the electric fields between the them diminish quickly, allowing electrons to become unbound from nuclei. However, as two quarks separate, due to the property of asymptotic, the gluon fields form narrow tubes (or strings) of color charge, which tend to bring the quarks together as though they were some kind rubber band. When two quarks have large enough energies and become separated, at some point it is more energetically favorable for a new quark/anti-quark pair to spontaneously appear out of the vacuum, than to allow the quarks to separate further. As a result of this, when quarks are production at high energy, instead of seeing the individual quarks, many color-neutral particles clustered together are observed, called *jet*. The process is called hadronization.

1.2 Quark Gluon Plasma and Relativistic Heavy Ion Collision

1.2.1 QCD phase transition and QGP

At ordinary condition, the quarks are confined and can not be isolated. But at extreme conditions like high temperature and high energy density, the Lattice QCD predicted a phase transition from normal QCD matter to a new matter, named *Quark Gluon Plasma* (QGP), with new color *degrees of freedom* (DOF). In this new phase, the mesons and baryons lose their identities and dissolve into a fluid quarks and gluons. The quarks and gluons can move around in a large distance rather than confined in hadrons, which is called *deconfinement*.

Figure 1.3 depicts the potential between two heavy quarks in different temperature conditions calculated by the 3 flavor Lattice QCD [KLP01]. It shows that at high temperature, the rampart of the potential between two heavy quarks which causes the

confinement will bend down due to the Debye color screening, approximately flat at high distance, thus liberate quarks from the trap. In addition, the continuous bending without sudden change indicates a crossover transition at high temperature and vanishing net quark density.

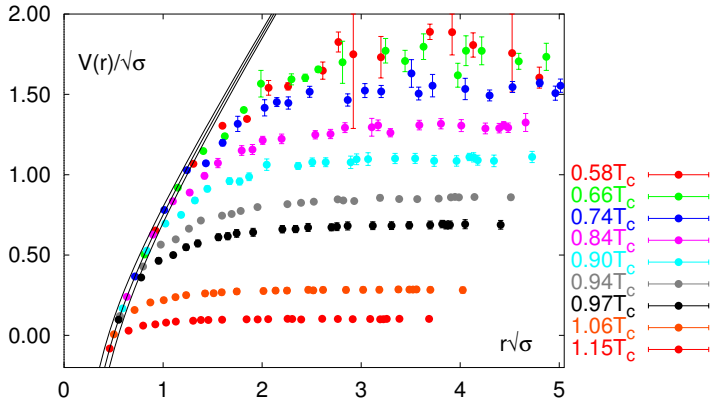

Figure 1.3: Temperature dependence of the heavy quark potential for three flavor Lattice QCD with a quark mass $m_q = 0.1$ GeV/c^2, adopted from Ref. [KLP01]. The band of lines gives the Cornell-potential $\alpha = 0.25 \pm 0.05$.

1.2.2 Relativistic heavy ion collisions

According the phase diagram calculated by Lattice QCD, the QGP is possible to be created experimentally in two different directions: 1) high temperature and low baryonic chemical potential (μ_b); 2) low temperature but large baryonic chemical potential. The relativistic heavy ion colliders are designed to search for the deconfined QGP matter in the first way, including BEVALAC at LBL, SIS at GSI, AGS at BNL, SPS at CERN, RHIC at BNL and the coming LHC at CERN.

The Relativistic Heavy Ion Collider (RHIC) at Brookhaven National Laboratory (BNL) is design for head-on Au + Au collisions at $\sqrt{s_{NN}}$ =200 GeV. To date, RHIC has successfully performed Au + Au collisions at 62, 130 and 200 GeV, Cu + Cu collisions at $\sqrt{s_{NN}}$ = 62 and 200 GeV, d + Au and $p + p$ collisions at 200 GeV, and some short low energy runs such as Au + Au collisions at 9 and 19 GeV and Cu + Cu collisions at 22 GeV.

In the relativistic heavy ion collisions, two nuclei can be represented as two thin disks approaching each other at high speed because of the Lorentz contraction effect in the moving direction. During the initial stage of the collisions, the energy density is higher than the energy density needed for the formation of QGP from the Lattice QCD calculation. Plenty of exciting physics results reveal that the matter created at RHIC is quite different from what we observed before, it can not be described by hadronic degrees of freedom and demonstrates many of the signatures from a QGP scenario. These measurements provide strong hints for the discovery of QGP [Ada05b]. Some selected key measurements will be discussed in the following sections.

1.2.2.1 Elliptic flow

In non-central heavy ion collisions, the initial spatial anisotropy of the created matter that causes the azimuthally anisotropic pressure gradient in the first place will be transferred into the final hadrons' azimuthal anisotropy in momentum space due to the pressure-driven expansion. This azimuthal anisotropy in momentum space can be expanded into a Fourier series as:

$$E\frac{d^3N}{dp^3} = \frac{d^2N}{2\pi p_T dp_T dy}(1 + \sum_{n=1}^{\infty} 2v_n \cos\left[n(\phi - \Psi_{rp})\right]), \tag{1.6}$$

$$v_n = \langle \cos\left[n(\phi - \Psi_{rp})\right]), \tag{1.7}$$

where Ψ_{rp} denotes the direction of the reaction plane. The Fourier expansion coefficient v_n stands for the n-th harmonic of the event azimuthal anisotropies. v_1 is so-called direct flow and v_2 is the elliptic flow. Due to the approximate elliptic shape of the overlapping region, the elliptic flow v_2 is the largest harmonic observed in mid-rapidity. Since the azimuthal anisotropy of the final states particles is transferred from the initial spatial anisotropy of the created matter, the elliptic flow is believed to carry the information of early stage and sensitive to the property of the hot dense medium.

The left panel of Fig. 1.4 shows identified particle $v_2(p_T)$ and the hydrodynamic model predictions. In this low p_T range, v_2 has larger values for lower mass particles.

This mass ordering is reasonably described by the hydrodynamics models, which assume ideal relativistic fluid flow and negligible relaxation time compared to the time scale of the equilibrated system. The agreement implies early thermalization, *i.e.* strongly interacting matter with a very short mean free path dominates the early stages of the collisions.

The right panel of Fig. 1.4 shows v_2 scaled by number of constituent quarks (NCQ) as a function of the NCQ scaled p_T. All of the particles at $p_T/NCQ > 0.6$ GeV/c fall onto one universal curve. This meson/baryon grouping phenomenon was also observed in the nuclear modification factor at moderate p_T [Ada05b]. Coalescence models which assume hadrons are formed through coalescing of constituent quarks provide a viable explanation for these observations. This indicates the flow developed during a sub-hadronic (partonic) epoch, and offers a strong evidence of deconfinement at RHIC.

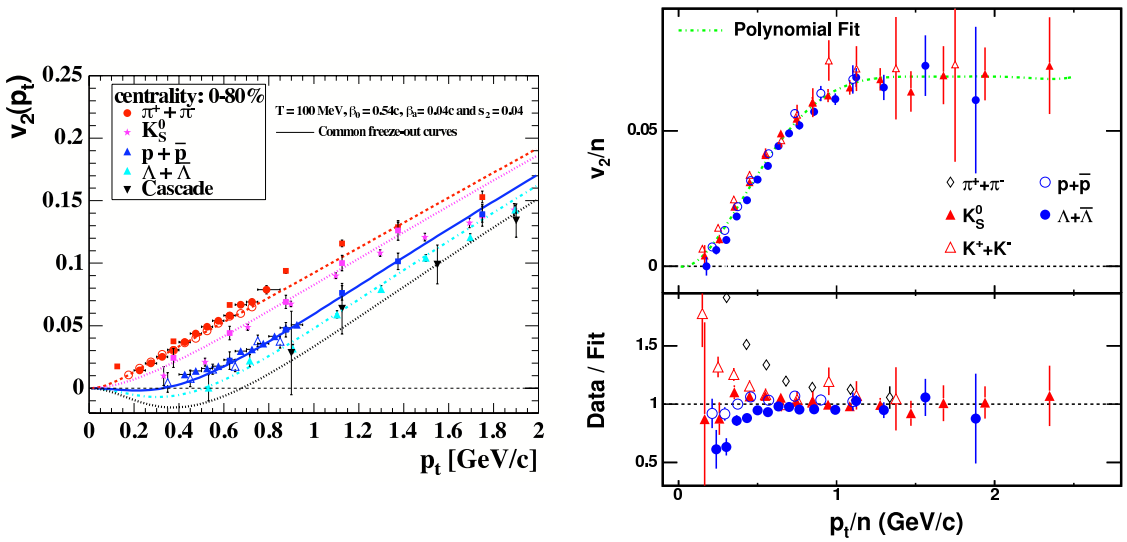

Figure 1.4: **Left:** Comparison of minimum bias $v_2(p_T)$ dependence on particle mass with blast-wave model fits.
Right: Test of the constitute quark number scaling of v_2 for minimum bias Au + Au collisions at $\sqrt{s_{NN}} = 200$ GeV. The figures are taken from Ref. [VPS08].

1.2.2.2 Jet quenching

In relativistic heavy ion collisions, the high p_T ($p_T > 5$ GeV/c) particles are believed to produced mainly from the initial QCD scattering processes following by parton fragmentation. This kind of particle can be used as unique probes by studying the interaction of partons with the hot dense medium. A widely used observable to this study is the nuclear modification factor R_{AB} which is the ratio of the spectra in heavy ion (A + B) collision and those in $p+p$ collisions, scaled by the number of binary nucleon-nucleon collisions:

$$R_{AB}(p_T) = \frac{d^2N_{AB}/dp_T dy}{T_{AB} d^2\sigma^{pp}/dp_T dy}, \tag{1.8}$$

where $T_{AB} = \langle N_{bin} \rangle / \sigma_{pp}^{inel}$ in the nuclear overlap geometry factor, calculated from a Glauber model [Abe08b]. If the nucleon-nucleon interaction is the same as that in $p+p$ collisions, the R_{AB} should be consistent with unity.

The left panel of Fig. 1.5 shows the R_{AB} in minimum bias and central d + Au and central Au + Au collisions at $\sqrt{s_{NN}} = 200$ GeV. At high p_T, the R_{AuAu} is a constant (0.2) and significant lower than 1, in contrast with that in d + Au collisions, in which the initial state condition is similar as in Au + Au collisions but final state is different. The combination of these two results suggest that the strong suppression in Au + Au collisions is due to the final state interactions rather than initial state effect and thus a very dense matter must be created in central Au + Au collisions at RHIC. The energetic partons strongly interact with the hot dense medium and loss energy, producing lots of soft particles instead of fragmenting to high p_T particles (leading particles).

This phenomenon is also evident in the dihadron azimuthal angle correlation study [Ada05b]. The right panel of Fig. 1.5 shows the azimuthal angle distribution of hadrons with $p_T^{associated} > 2$ GeV/c relative to a trigger hadrons with $p_T^{trigger} > 4$ GeV/c. A hadron pari drawn from a single jet will generate an enhanced correlation at near side ($\Delta\phi \approx 0$), as observed for $p+p$, d + Au and Au + Au collisons, with similar correlation strengths, widths. The pair from back-to-back jet correlation on away side

($\Delta\phi \approx \pi$) only appears in $p+p$ and d + Au collisions while uniquely absent in central Au + Au collisions. This result suggests that the disappear of the away side correlation in central Au + Au collision is again due to the final state interactions of the hard-scattered partons in the hot dense medium.

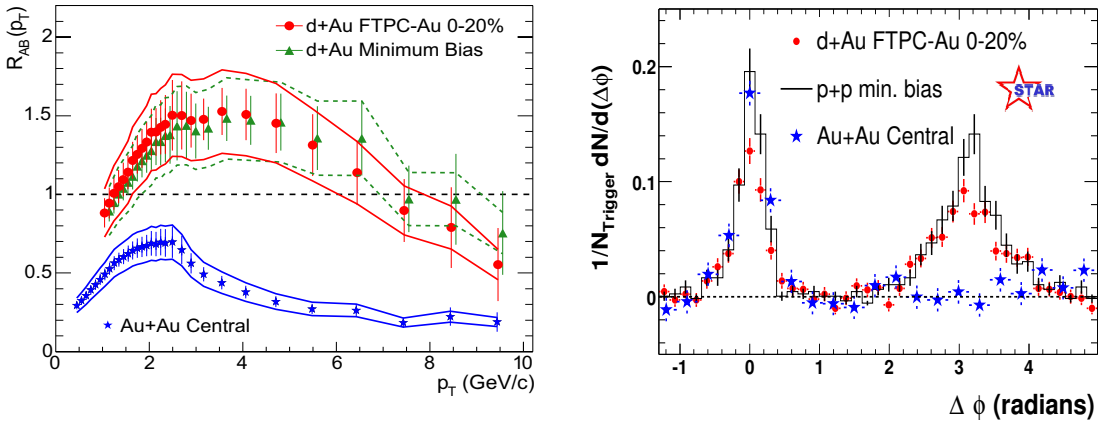

Figure 1.5: **Left:** $R_{AB}(p_T)$ for minimum bias and central d + Au and central Au + Au collisions.
Right: Two particle azimuthal distributions in $p+p$, d + Au and central Au + Au collisions.

1.2.2.3 Heavy quark in relativistic heavy ion collisions

Heavy flavor is a unique prob to test the pQCD and the property of the medium produced in the heavy ion collisions due to its much larger mass than that for light flavor. To date, the open heavy flavor is mostly measured indirectly through the semi-leptonic channel ($c \to e$ and $b \to e$). The left panel of Fig. 1.6 shows the heavy quark decayed electron R_{AA} as a function of p_T in d + Au and central Au + Au collisions measured by the STAR collaboration. At high p_T , the heavy quark decayed electron has similar suppression at the light flavors, suggests that the heavy quark also has large energy loss. STAR also make progress to separate the suppression from charm and bottom quarks through the azimuthal correlations between heavy decayed electrons and hadrons or D-mesons [Wan08]. With the upgraded reaction plane detector, PHENIX also measured non-zero elliptic flow of the heavy decayed electrons shown in the right panel of Fig. 1.6, which suggests that the charm is flowing even its mass is so large.

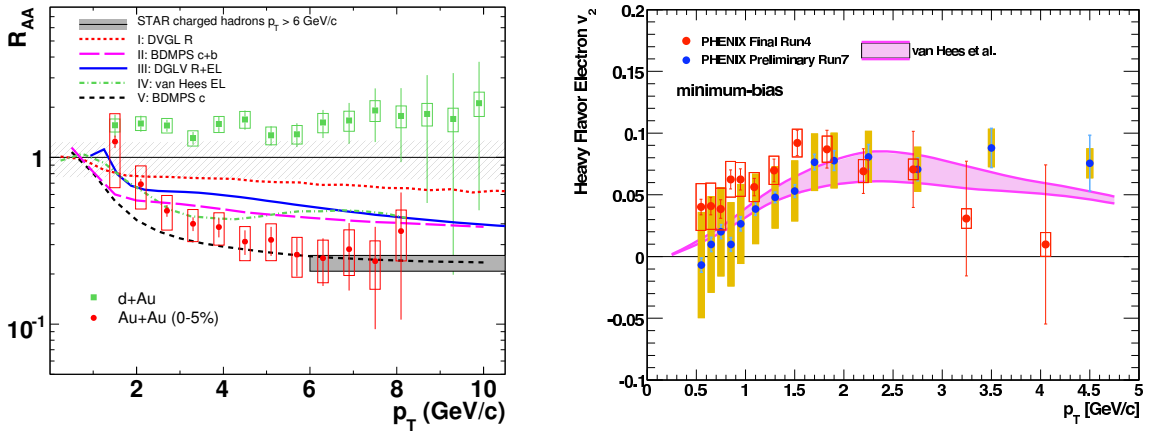

Figure 1.6: **Left:** Non-photonic electron R_{AA} as a function of p_T in d + Au and Au + Au collisons. **Right**: Elliptic flow of non-photonic electron as a function of p_T in Au + Au collisions. There figures are taken from [Abe07, Hor08]

As the bound states of heavy quarks, the heavy quarkonium is even more unique than the open heavy flavor. For example, the dissociation of the J/ψ in heavy ion collisions due to the color screening effect is proposed as one of the signatures of the formation of the QGP. In the following sections, i will discuss the production mechanism of charmonium which is essential for the understanding of the modification of production from the hot dense medium, and its behavior in heavy ion collisions.

1.3 Production Mechanism of Charmonium

1.3.1 Charmonium system

Charmonium is the bound states of charm quark and anti-charm quark. The first charmonium discovered is J/ψ, which is discovered by two independent groups in November, 1974. The discovery of J/ψ play a very important pole in the development and evolution of the Standard Model, causing the introduction of charm quark into the Standard Model. From that time, more and more charmonium states were founded. Figure 1.7 shows the charmonium spectroscopy. The lowest states of charmonium are η_c, η_c', J/ψ, ψ', $\chi_{c0,1,2}$ and etc. J/ψ is the second lowest charmonium states and mostly investigated. For the feed-down sources of the J/ψ, the χ_cs have large branching ratio to

decay into J/ψ by radiating a γ except the χ_{c1}. The ψ' also have some possibility to decay into J/ψ. There is also some J/ψ decayed from B-hadrons.

The J/ψ lies just below the threshold for decay into $D^0\bar{D}^0$. Therefore, by energy and momentum conservation, the J/ψ can decay hadronically only through OZI suppressed channels. This is thought to be the reason for the small width of the J/ψ. The dominant hadronic decay channel for J/ψ proceeds through a 3-gluon intermediate state. The preferred means of studying the J/ψ is the dileptonic channels.

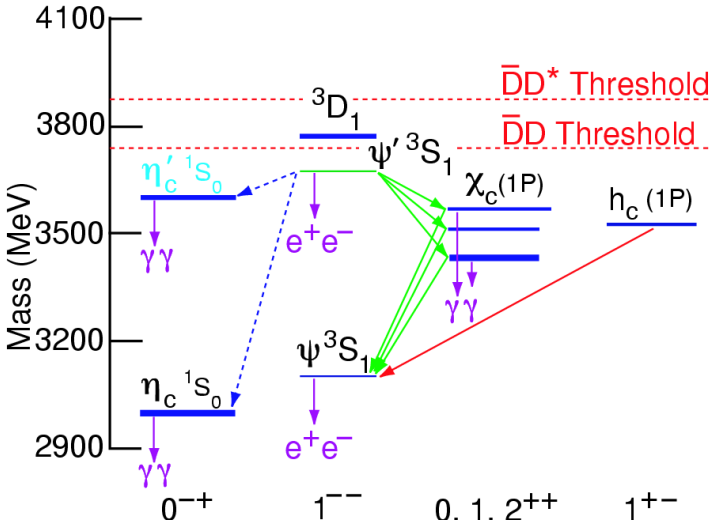

Figure 1.7: Charmonium spectroscopy.

When the charmonium is produced, it needs some time for the quarks go through a distance to form the bound the states. The formation time is depending on the potential of the charmonium state. One of the popular potential is the so-called *Cornell potential*:

$$V(r) = \sigma r - \alpha/r, \tag{1.9}$$

where r is the effective radius of the charmonium state and σ, α are parameters. The first part of the potential, αr, is known as the *confinement* part of the potential. The second part, $-\alpha r$, corresponds to the potential induced by one-gluon exchange between the charm quark and anti-charm quark, and is known as the *Coulombic* part of the potential, since its $1/r$ form is identical to the well-known coulombic potential induced

by the electromagnetic force. The charmonium states's radius and the "formation time" is dependent on the parameters σ, α and charm quark mass. One sets of the formation times are list in Tab. 1.1, which is taken from [BO87].

Table 1.1: Radius and formation time of charmonium states.

Charmonium	Mass (GeV/c62)	radius (cm)	Formation time (fm/c)
J/ψ	3.1	0.45	0.7
ψ'	3.7	1.8	1.1
χ_c	3.5	2.4	1.2

1.3.2 Charmonium production mechanism

After the discovery of J/ψ in 1974, the J/ψ production has been measured in variant colliders and our understanding of its production mechanism has been gone several cycles in last decades.

The Color Singlet Model (CSM) was first proposed shortly after the discovery of the J/ψ [BJ81, BR81]. In this model, the formation of quarkonium is decomposed into two steps:1) creation of two on-shell heavy quarks; 2) binding of these two heavy quarks to make mesons. In the first step, since the charm quark mass is much larger than the QCD scale Λ_{QCD}, the cross section is computed in pQCD. In the second step, the quarkonium formation, the heavy quarks are at rest in the meson frame and the color and the spin of the heavy quark pair do not change during the binding. Which means the heavy quark pairs have to be produced initially in color-singlet state. In high energy collisions, the leading contribution comes from a gluon fusion process: $gg \rightarrow {}^3S_1 g$. This model did a good job at the CERN-EMC and CERN-ISR energy, described the J/ψ photo- and hadron-produciton very well [BR81, BJ81].

When the energy went higher, the CSM started to face problems. The inclusive J/ψ, ψ' and χ_c cross section from the UA1 experiment at the CERN and from the CDF collaboration at Tevatron started to show discrepancies from the CSM predictions. But at that time, the contributions from B-meson can not be distinguished. The CSM still could roughly described the data by predicting a huge B-mesons contributions to

inclusive charmonium states, making the B-decays as the dominate source of the J/ψ production at that energy. A rigorous test of the CSM became possible when CDF presented a measurement of the direct ψ' cross section, where the contribution from B-decays had been removed using the microvertex-detection. It turned out that the B-mesons contribution to ψ' is only $\sim 25\%$. The CSM prediction was orders of magnitudes less than the measurement at $p_T > 5$ GeV/c.

To solve the discrepancy of the LO CSM predictions and experimental measures, people pointed out that the gluon and heavy quark fragmentation had to be take into account even though of higher order in α_s. The calculations indeed showed that by including the gluon and heavy quark fragmentations, the CSM predicted higher cross section for both J/ψ and ψ', especially at high p_T because the contributions from fragmentations have steeper shape ($1/p_T^4$ vs. $1/p_T^8$). This prediction went closer to the prompt J/ψ cross section and the discrepancy was accounted by the experimental and theoretical uncertainties. As the same as the ψ' case, when the CDF collaboration removed the contributions from the radiative χ_c decays from the prompt J/ψ cross section, the CSM was ruled out at the high energy hadron collisions since it underpredicted the direct J/ψ cross section at Tevatron energy by a factor of 30 times.

Then the Color Octet Model is introduced in the framework of Non-Relativistic QCD (NRQCD), which is a effective theory based on a systematic expansion in both α_s and v (the quark velocity within the bound state). This model allows the formation of a charmonium from a color octet $c\bar{c}$ pair with one or some soft gluon emissions later. The partonic quarkonium production cross section of the quarkonium state is a sum of the products of NRQCD matrix elements and short distance coefficients with an expansion in powers of v. The short distance coefficients are essentially the process dependent partonic cross sections to make a $c\bar{c}$ pairs. It can be computed perturbatively. The transition between the $c\bar{c}$ pair and the final physical quarkonium state is describe by the NRQCD matrix elements, which are free parameters needed to be obtain from experiments. With this model, the CDF J/ψ cross section measurement is finally described by the model calculations. By a few years later, the CDF collaboration

provided another tool to constrain the model calculations: the polarization of prompt J/ψ. The only model described the cross section of the J/ψ at that time failed even though the χ_c feeddown may make the comparison difficult, which predicted a large transverse polarization, while the experiment measured a zero polarization at moderate p_T and becomes longitudinal at higher p_T.

In the beginning of this new century, the Belle collaboration found that more than 80% of J/ψ are produced associated with another $c\bar{c}$ pair in 10.6 GeV e^+e^- collisions [Abe02, Pak04]. No model can explain this observation at that time and people start to think about the NLO contributions. It turned out the NLO corrections at LHC and Tevatron energy are huge compared to the LO contributions. The CSM is recently developed by including the high order corrections [ACL08, Lan08]. It described the Υ spectra at Tevatron and J/ψ spectra at low p_T at RHIC but failed at high p_T at Tevatron. After including some NNLO diagrams, this new CSM qualitatively reproduce the Υ polarization.

1.4 Charmonium Production in Heavy Ion Collisions

In the presence of the medium, the Charmonium production in high energy heavy ion collisions is different with that in hadron collisions. The J/ψ has long been though of as the probe of the "Smoking Gun" quality-the kind of probe that could definitively prove the formation of a QGP in relativistic heavy ion collisions. Both calculations performed by Matsui and Satz in the 1980s and Lattic QCD results (of the time) predicted that charmonium bound states would "melt" in the QPG due to the color screening effect, and that this process would lead to a suppression of charmonium yields when compared to nominal pQCD calculations. This suppression was proposed as one of the signature of the formation of QGP. But these is some other medium effects have to be considered to influence this probe. Nowadays people believe that the medium effects on the charmonium production in heavy ion collisions can be categorized into two parts: 1) the effects from the QGP, called as "final state effects"; 2) the effects from the

nuclear matter before the QGP formation, these initial state effects don't require the formation of QGP thus usually referred as cold nuclear matter effects (CNM).

As the final state effects, the possible contributions are:

- Color screening by the abundance of thermal partons in QGP.
- Recombination from uncorrelated $c\bar{c}$ pairs in QGP at the phase boundary.
- Interaction of charmonium with secondary comoving hadrons (comovers).

For the CNM effects, the possible contributions are:

- Modification of gluon distribution function in heavy nuclei such as gluon *shadowing*, gluon *anti-showing* and etc.
- Interaction of pre-resonance $c\bar{c}$ state with the projectile or target nuclei, usually referred as *nuclear absorption*.
- Multiple interactions of partons inside the nuclei, usually referred as *Cronin effect*.

1.4.1 Final state effects

We start will the formal treatment of charmonium dissociation due to the color screening effect, originally formulated by Matsui and Satz [**?**]. In the presence of the QGP, the confinement term in the Cornell potential of the heavy quark pairs discuss above will disappear, and the coulombic term is needed to be modified due to de Debye screening of colored partons, similar as that in the electromagnetic plasma. The modified potential can be written as:

$$V(r) = -\frac{\alpha}{r} e^{-r/\lambda_D(T)}, \tag{1.10}$$

where $\lambda_D(T)$ is the Debye screening radius. This potential can still allow for bound states to form. But when the screening length of the quark color charge is less than the hadronic raidus, the valence quarks of the quarkonium state can not longer "feel" each

other and are unable to form a bound state. The Debye screening length depends on temperature and becomes smaller with increase of temperature. As deconfinement is an essential ingredient in the arguments formulated here, an observed suppression would imply that there is deconfinement in relativistic heavy ion collisions.

Another dissociation mechanism besides the color screening is parton-induced destruction in the QGP. This mechanism is essentially the dynamic counterpart of static Debye color screening. Since J/ψ is small system and tightly bound system, only a sufficiently high energy projectile can break the binding. Therefore it is expected that J/ψ can only be dissociated by the interaction with a hard gluons of the hadron, not with the hadron as a whole. The calculations shows that the dissociation cross section of J/ψ by thermal gluons is significantly larger compared to that by hadrons, which indicates that the J/ψ can be dissolved in QGP and survive in confined medium.

The comover scattering of J/ψ in an additional absorption of J/ψ by hadronic secondaries called comovers, which is occurred in hadronic phase.

There dissociation mechanism is possible to compensate in the transition or hadronization stage from the regeneration processes. The STAR and PHENIX collaborations at RHIC measured both the radial and elliptic flow for the heavy flavor decayed electrons which suggest the charm quark may reached thermal equilibrium. If this is true, the thermalized primordial charm and anti-charm quarks coming together may on a statistical basis to form bound states near or at the phase boundary between hadron matter and QGP. The important physics message from the regeneration mechanism is that an observation of enhancement would not only imply deconfinement, but may also imply *thermalization*. The latter is a critical requirement for the formation of a QGP. It should be noted that observation may not necessarily rule out the possibility for some level of J/ψ production via regeneration.

1.4.2 Cold nuclear matter effects

As discussed before, there is some initial state affecting the J/ψ productions, which has to be account for before firm conclusion can be drawn about the effect of the hot medium thought to be created.

The nuclear quark and anti-quark distribution function have been probed through deep inelastic scattering (DIS) of lepton and neutrinos from nuclei. These measurements (EMC collaboration for example) found that the parton distribution function in nucleus is modified compared to that in free protons. This modification of the parton distribution function in a nucleus in usually quantified as the ratio of parton structure function in the nucleus to that in a deuteron or a carton nucleus. At low x (the fraction of momentum carried by the parton), the ratio is smaller than 1 and increase as a function of increase x. This region is usually referred as shadowing region. At $0.1 < x < 0.3$, the ratio is larger than 1, increasing and then decrease. This region is usually referred as the anti-shadowing region. At $x > 0.3$ the ratio is smaller than 1 again and decrease as increasing x. This modification of parton distribution difference has to affect the charmonium production in p + A or $A + A$ collisions. And the effects may be different for different charmonium states, and the charmonium from different sources such as B-mesons feeddown to J/ψ.

The partons also suffering the multiple scattering while they traverse in the nuclei before production J/ψ. Gluons from the projectile collides with various target nucleons exchanging transverse momentum at each collision vertex, which leads to the p_T distribution of J/ψ wider compared to that in $p + p$ collisions. This is known as Cronin effect.

Besides the modification of the parton modification functions, the projectile/target nucleons also has the possibility to broke the pre-resonance $c\bar{c}$ state, which still has no enough time for form the final charmonium states yet, into $D\bar{D}$. The survive possibility

of pre-resonance $c\bar{c}$ state of J/ψ (S^{abs} can be represented as:

$$S_{AB}^{abs} = e^{-\rho_0 \sigma_{abs} L(A,B)}, \tag{1.11}$$

where ρ_0 is the nuclear matter density, σ_{abs} is the effective absorption cross section and $L(A,B)$ depicts effective pass length through the nuclear matter. The production of cross section of J/ψ in $A+B$ collisions ($\sigma_{J/\psi}^{AB}$) relative to that in nucleon-nucleon collisions ($\sigma_{J/\psi}^{NN}$) can be represented as:

$$\frac{\sigma_{J/\psi}^{AB}}{\sigma_{J/\psi}^{NN}} = AB \times S_{AB}^{abs} \tag{1.12}$$

1.5 Motivation of This Study

As discussed before, the J/ψ suppression is proposed as one of the signatures of the formation of the QGP. Recent Lattice QCD calculations and potential analyses find the J/ψ dissociation temperature (2.10 T_c) is higher than the temperature reached in $Pb+Pb$ collisions at 17.3 GeV at CERN-SPS ($\sim$ 1.2 T_c), and Au + Au collisions at 200 GeV at BNL-RHIC ($\sim$ 1.5 T_c). While for the higher charmonium states χ_c and ψ', their dissociation temperature is just above T_c (1.16 T_c and 1.12 T_c respectively). That may suggest that the direct J/ψ may not be suppressed in the current experiments and the J/ψ suppression observed at SPS and RHIC are possible from the J/ψ decayed from higher charmonium instead of direct J/ψ. This is evident in Fig. 1.8. The left panel shows the J/ψ survival possibility ($S(J/\psi)$) (CNM effects have been removed) in $Pb+Pb$ and $In+In$ collisions at $\sqrt{s_{NN}}$ = 17.3 GeV measured by NA50 and NA60 collaborations as a function of energy density of the created medium. NA50 collaboration also measured ψ' suppression in $Pb+Pb$ collisions. People believe that there is only about 60% J/ψ is directed produced. The feeddown contribution are most from χ_c and ψ'. By assume the χ_c and ψ' suppression is the same and the direct J/ψ has no suppression, the authors of [KKS06] compared the $0.4S(\psi')+0.6$ with the

$S(J/\psi)$ and found they are consistent with each other very well, shown in the left panel of Fig. 1.8. They also compared the J/ψ survival possibility from SPS and RHIC and found they also consistent with each other. The $S(J/\psi)$ from SPS and RHIC are both stop at about 0.6 except the PHENIX central data point with relative large uncertainty.

Table 1.2: Dissociation temperature of quarkonia inferred from Lattice QCD calculations and potential model analyses.

Quarkonium	J/ψ	χ_c	ψ'	Υ (1S)	χ_b (1P)	$\Upsilon(2S)$	χ_b (2P)	Υ (3S)
T_d/T_c	2.10	1.16	1.12	≥ 4.0	1.76	1.60	1.19	1.17

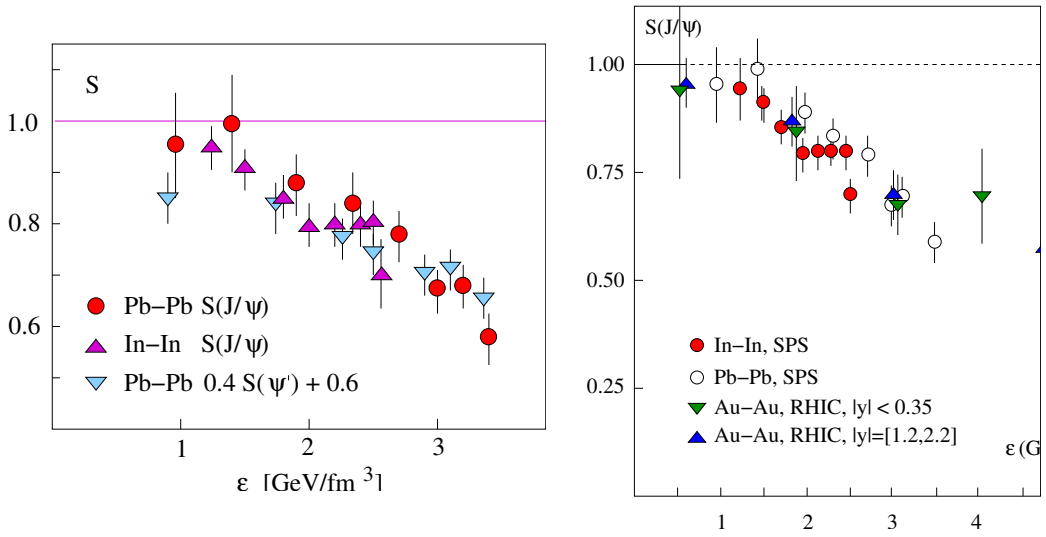

Figure 1.8: **Left:** Universal J/ψ and ψ' suppression at SPS. **Right**: The J/ψ suppression at SPS and RHIC. The figures are taken from Ref. [KKS06].

If it is true that the direct J/ψ is not suppressed at SPS and RHIC, do we really need to wait for the LHC to measure the direct J/ψ suppression? Recently, one AdS/CFT calculation [LRU07] which treat the fermion pairs have velocity with respect to the hot dense medium predict the decrease J/ψ dissociation temperature as increasing p_T, shown in Fig. 1.9. It shows that at $p_T > 5$ GeV/c, the dissociation of the J/ψ decrease to $\sim 1.5\ T_c$ which is the temperature people believe the RHIC reached [Ada05b]. Consequently, J/ψ production is predicted to be more suppressed at high p_T, in contrast to the standard suppression mechanism. This prediction can be tested with measurements of J/ψ over a broad kinematic range, in both $p+p$ and $A+A$ collisions.

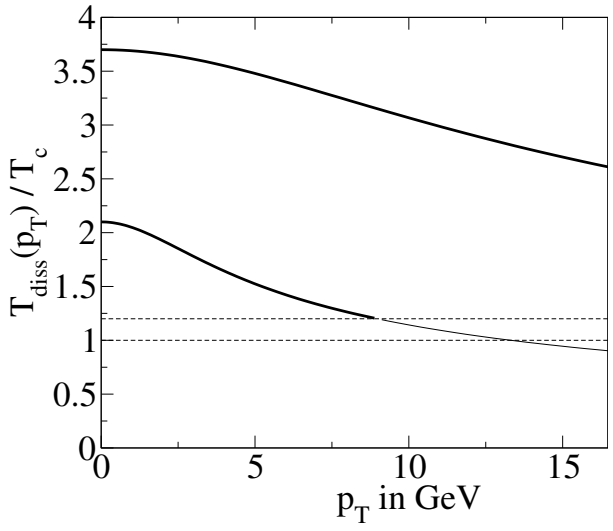

Figure 1.9: J/ψ dissociation temperature as a function of p_T in hot wind calculate by AdS/CFT. The figure is taken from [LRU07]

.

And if this calculation is correct, we may be able to study the direct J/ψ suppression by measuring the high p_T J/ψ.

The interpretation of J/ψ suppression (observed by SPS and RHIC and probably will be observed at LHC) requires understanding of the quaronium production mechanism in hadronic collisions, which include direct production via gluon fusion and color-octet and color-singlet transition, as described by NRQCD; parton fragmentation; and feeddown from higher charmonium states and B meson decays. No model at present fully explains the J/ψ systematic observed in elementary collisions (cross section, polarization, double $c\bar{c}$ pair production and etc). J/ψ production at high-p_T in $p+p$ and nuclear collisions may provide additional insights into the basic processes underlying quarkonium production.

The knowledge of the feeddown contribution to the inclusive J/ψ is also important for understanding the J/ψ production mechanism. As discussed before, before moving the B decays contributions to the ψ' people can not rule out the leading order color singlet model even it turned out later that the model calculation is less than the measurement by a factor of 30. Even more, the B production is rarely measured at RHIC energy, and people are even having problem to extract the charm suppression

from the non-photonic electron analyses due to the contamination of $B \rightarrow e$. People are trying to measure the ratio of $B \rightarrow e$ to the total non-photonic electrons through the angular correlations of non-photonic electron and hadrons or Ds, and etc [Wan08]. These analyses still can not provide a strong constraint on this due to the γ conversion and π^0 Daliz decay (which can not be removed unlike the γ conversion) backgrounds and statistics. The $B \rightarrow J/\psi$ measurement can provide additional and independent information on the B production and its contamination to the open charm measurement.

I will introduce our experiment setup in Chapter 2. And describe the analysis procedures on spectrum analysis in Chapter 3 and J/ψ-hadron correlation in Chapter 4 in detail. The results will be discussed in Chapter 5. In Chapter 6, i will talk a little bit on our future of the J/ψ measurement.

CHAPTER 2

Experimental Set-up

2.1 RHIC Accelerator Complex

The Relativistic Heavy Ion Collider (RHIC) at Brookhaven National Laboratory (BNL) is designed to accelerate and collide heavy ions and polarized protons with high luminosity, allowing physics to explore the strong iteration through many extensive and intensive measurements. It started to construct during 1991 and began operate in 2000, following 10 years development and continuing construction. It is the first facility to collide heavy ion beams and the top center-of-mass collision energy is 200 GeV per nucleon pair, which is about more than 10 times greater than the highest energy reached at previous fixed target experiment. The purpose of this extraordinary new accelerator is to seek out and explore new extremely high-energy and high-temperature forms of matter and thus continue the centuries-old quest to understand the nature and origins of matter at its most basic level. RHIC is also delivering polarized proton beams up to center-of-mass energy 500 GeV/c to carry on vigorous spin scientific program. The basic design parameters of the collider are list in Tab. 2.1 [HLO03]. The luminosity achieved now is actually much higher than the original design. The store-averaged luminosity reached now are 12×10^{26} cm^{-2}s^{-1} for Au + Au collisions, 2.3×10^{31} cm^{-2}s^{-1} for $p + p$ collisions and 1.3×10^{29} cm^{-2}s^{-1} for d + Au collisions.

Figure 2.1 shows a diagram of the RHIC machine complex, including a Van de Graaff facility, a Linear Proton Accelerator, the Booster Synchrotron ring, the Alternative Gradient Synchrotron (AGS), and ultimately the RHIC synchrotron ring. For Au beam operations, the negatively charged Au ions from the pulsed sputter ion

Table 2.1: Performance specifications of RHIC [HLO03]

	For Au + Au	For $p+p$
Beam energy	100 $\rightarrow$ 30 GeV/nucleon	250 $\rightarrow$ 30 GeV/nucleon
Luminosity	2×10^{26} cm^{-2}s^{-1}	1.4×10^{31} cm^{-2}s^{-1}
Number of Bunches/ring	60 ($\rightarrow$ 120)	60 ($\rightarrow$ 120)
Luminosity lifetime	$\sim$10 hours	$>$ 10 hours

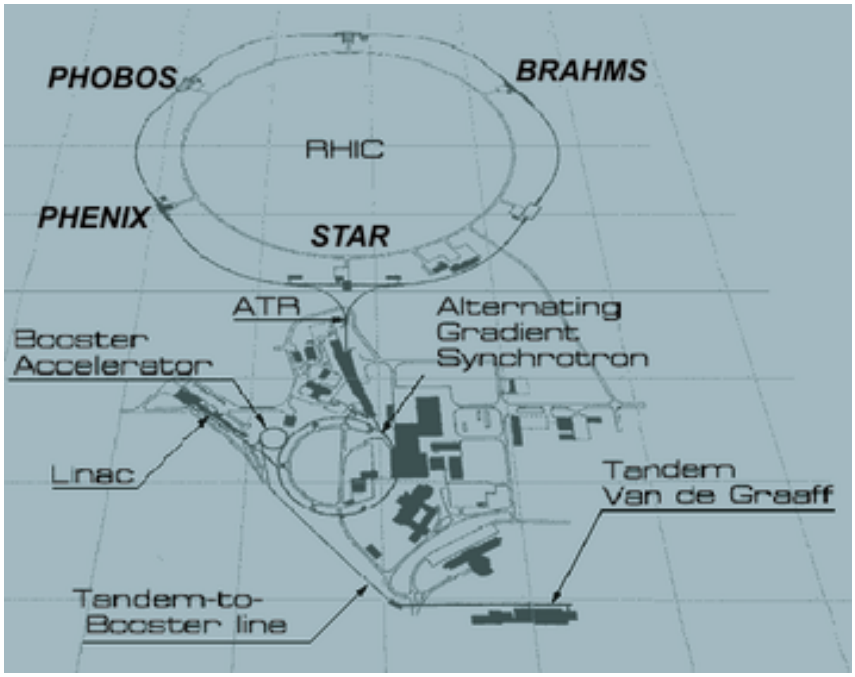

Figure 2.1: Schematic of the RHIC complex

source at the Tandem Van de Graaff are partially stripped of their electrons with a foil at the Tandem's high voltage terminal, and then accelerated to the energy of 1 MeV/nucleon by the second stage of the Tandem. After further stripping at the exit of the Tandem and a charge selection by bending magnets, the ions with charge state of +32 are delivered to the Booster Synchrotron and accelerated to 95 MeV/nucleon. Ions are stripped again at the exit from the Booster to reach the charge stat of +77 and injected to the AGS for acceleration to the RHIC injection energy of 10.8 GeV/nucleon. The 24 bunched injected into AGS are debunched and then re-bunched to four bunches at the injection from porch prior to the acceleration. There four bunches are transferred to RHIC, one bunch at a time, to RHIC through the AGS-to-RHIC Beam Transfer Line. Au ions are fully stripped to the charge state of +79 at the exit from the AGS. For

proton operations, the protons are injected from the 200 MeV Linac into the Booster, followed by acceleration in the AGS and injection into RHIC.

The RHIC consists of two quasi-circular concentric accelerator/storage rings on a common horizontal plane. Rings are oriented to intersect with one another at six locations along their 3.8 km circumference. 4 for them are quipped with detectors. They are two large experiments STAR (6 o'clock) and PHENIX (8 o'clock) and two smaller ones PHOBOS (10 o'clock) and BRAHMS (2 o'clock), respectively.

To date, RHIC has been run in $p+p$, d + Au, Au + Au and Cu+Cu configurations at variant energies.

2.2 STAR Detector

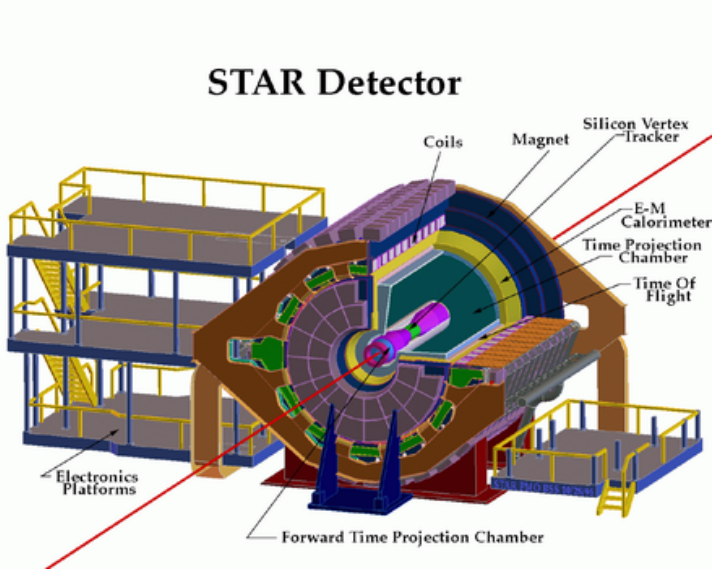

Figure 2.2: Perspective view of the STAR detector.

STAR is short from Solenoidal Tracker at RHIC. It was constructed to investigate the behavior of strongly interacting matter at high energy density and to search for signatures of QGP formation. Key features of the nuclear environment at RHIC are a large number of produced particles (up to approximately 1000 per unit of pseudo-rapidity) and high momentum particles from hard parton-parton scattering.

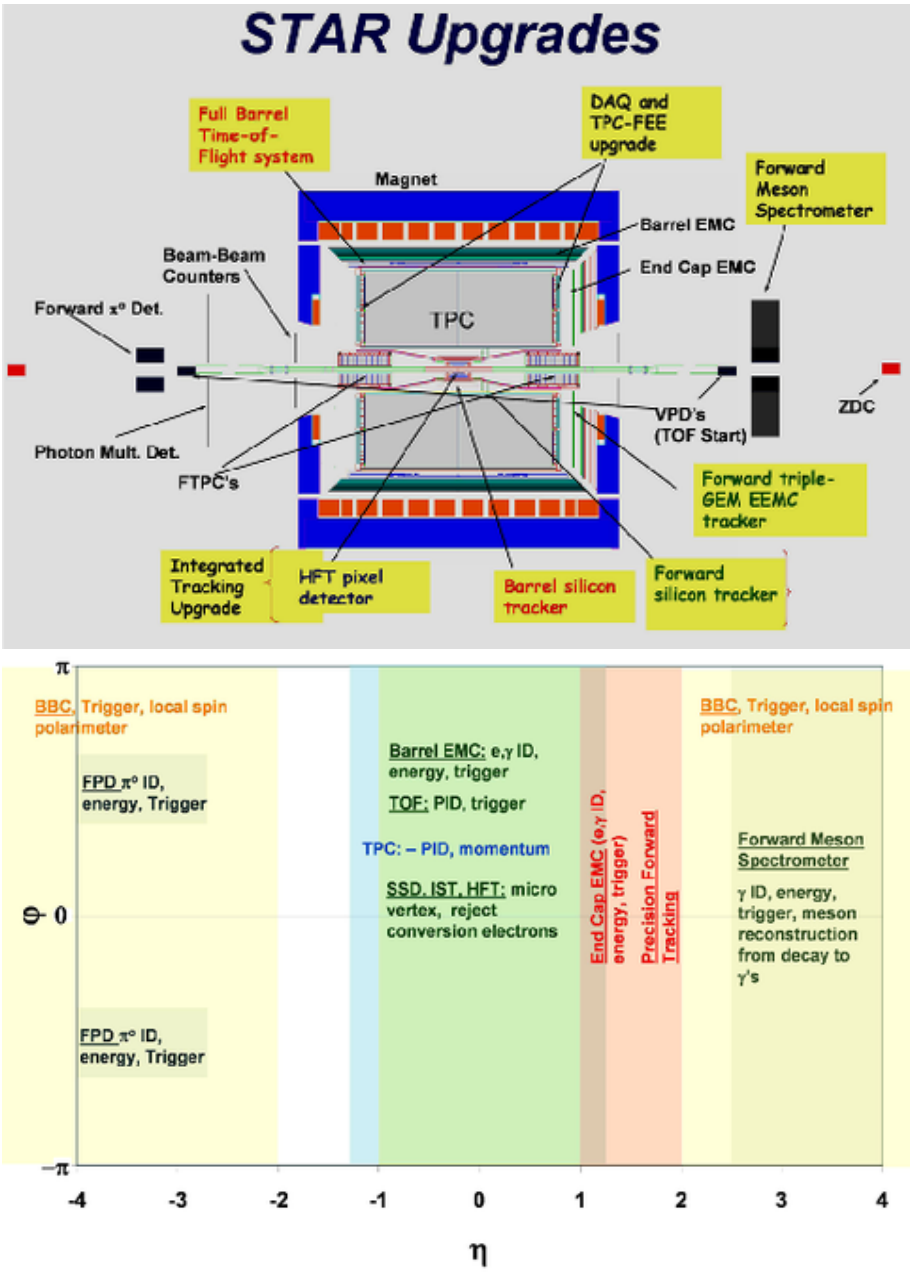

Figure 2.3: Cutaway side view of the STAR detector (upper panel) and its coverage (lower panel).

STAR are measuring many observables simultaneously to study signatures of a possible QGP phase transition and to understand the space-time evolution of the collision process in ultra-relativistic heavy ion collisions. The goal is to obtain a fundamental understanding of the microscopic structure of these hadronic interactions at high energy densities. In order to accomplish this, STAR was designed primarily for measurements of hadron production over a large solid angle, featuring detector systems for high precision tracking, momentum analysis, and particle identification at the mid-rapidity. The Large acceptance of STAR makes it particularly well suited for event-by-event characterizations of heavy ion collisions and for the detection of hadron jets.

STAR consists of several subsystems. The Layout of the STAR experiment is shown in Fig. 2.2. A cutaway side view of the STAR detectors and their coverage is displayed in Fig. 2.3.

Magnet The STAR Magnet [Ber03] is cylindrical in design with a length of 6.85 m and has inner and outer diameter of 5.27 m and 7.32 m, respectively. It generates a field along the length of the cylinder having a maximum of $|B_z| = 0.5$ T. It allows the tracking detectors to measure the helical trajectory of charged particles to get their momenta. To date, the STAR magnet has been run in full field, reversed full field and half field configurations.

Tracker The Time Projection Chamber is the main tracker of STAR, it covers the $|\eta| < 1.8$ and 2π in azimuthal. The details of TPC detector will be discussed in the next section (sec. 2.2.1). To extend the tracking to the forward region, a radial-drift TPC (FTPC) is installed covering $2.5 < |\eta| < 4$ also with complete azimuthal coverage and symmetry [Ack03]. To improve the precision of the tracking at the forward region, a Forward GEM Tracker (FGT) based on triple GEM technology is proposed and in preparation [Sim08].

Inner Tracker Charged particle tracking close to the interaction region is accomplished by two inner tracks Silicon Vertex Tracker (SVT) [Bel03] and Silicon Strip Detectors (SSD) [Arn03]. The SVT consist of 216 silicon drift detectors (equivalent to a total of 13 million pixels) arrange in three cylindrical layers at distances of approximately 7, 11 and 15 cm from the beam axis. The SSD constitutes the fourth layer of the inner tracking system. It is placed at a distance of approximately 23 cm from the beam axis. The silicon detectors cover $|\eta| \lesssim 1$ with complete azimuthal symmetry. Silicon tracking close to the interaction allows precision localization of the primary interaction vertex and identification of secondary vertices from weak decays of, for example, Λ, Ξ, and Ωs and possible D-hadrons. The Inner tracker is helpful for secondary vertices reconstruction but contribute considerable material budget which produces lots of photonic background to the electron related analysis. Figures 2.4 shows the distribution of the gamma conversion radius. The SVT and SSD has been taken out in RHIC year 2008 run for this reason. To provide more precise secondary vertices for heavy flavor (mostly c and b) measurements, STAR is proposing to build a new silicon vertex detector Heavy Flavor Tracker (HFT) [Sha07, Kap08]. This detector will have two layers of pixels with limited materials located at mean radius of 1.5 cm and 5 cm from the beam axis and will be combined with the SSD to fill the gap between the innermost silicon detectors and the TPC.

Table 2.2: Material budget of STAR detectors

Detector	Material budget (X_0)	Comment
beam pipe	0.29%	
beam pipe wrap	0.14%	
air	0.1%	
SVT	6%	removed from 2007
SSD	1%	removed from 2007
TPC inner filed cage	0.36%	

Electro-Magnetic Calorimeter The STAR Barrel Electro-Magnetic Calorimeter (BEMC) located outside of the TPC covers $|\eta| < 1$ with complete azimuthal symmetry [Bed03]. The Endcap Electro-Magnetic Calorimeter (EEMC) provides

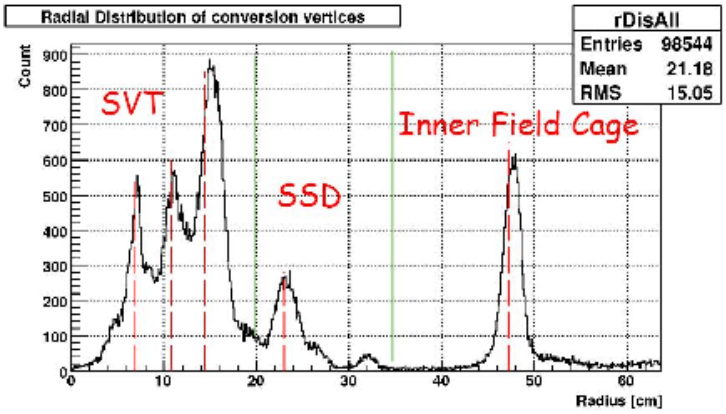

Figure 2.4: Distribution of the gamma conversion radius. The dashed lines represent the mean physical radius of the detectors.

coverage for $1 < \eta \leq 2$, over the full azimuthal range, supplementing the BEMC [All03]. This system allows measurement of the transverse energy of events, and trigger on and measure high transverse momentum photons, electrons, and electromagnetically decaying hadrons. The EMCs include shower-maximum detectors (SMD) to distinguish high momentum single photons from photon pairs from π and η meson decays. They can also be used to distinguish electrons from charged hadrons. The EMCs also provide prompt charged particle signals essential to discriminate against pileup tracks in the TPC, arising from other beam crossings falling within the 40 μs drift time of the TPC, which are anticipated to be prevalent at RHIC $p+p$ collision luminosity ($\sim 10^{32} cm^{-2} s^{-1}$). Recently, the EMCs are also started to be used as a high p_T hadron trigger, which has successfully extended the identified particle spectra in $p+p$ up to ~ 15 GeV/c. The BEMC and BSMD is two of the main detectors for this analysis and will be discussed in detail in Sec. 2.2.2 and Sec. 2.2.3.

Forward Photon and Meson Detector At the pseudo-rapidity range more forward than the EEMC pseudo-rapidity coverage, STAR installed a preshower Photon Multiplicity Detector (PMD) which covers $2.3 < |\eta| < 3.5$. This detector is designed to measure multiplicity and spatial distribution of photon on a event basis in the forward region where high particle density precludes the use of a calorimeter [Agg03]. At even more forward region, STAR installed another Calorimeter, Forward π^0 Detector (FPD)

to measure π^0 at large rapidity and moderate transverse momentum. In RHIC year 2008 run, STAR has completed the upgrade from FPD to a much larger detector Forward Meson Spectrometer (FMS) which has the capability to measure neutral particle such as π^0, η and J/ψ in the pseudo-rapidity range $2.5 < \eta < 4$.

Time-Of-Flight System The STAR Time-Of-Flight (TOF) [Sha06, Don06, Llo05] is based on Multi-Resistive Gap Chamber (MRPC) technique. It locates between TPC and BEMC, covers $|\eta| < 1$ and full azimuthal angle, has < 80 ps intrinsic timing resolution and $> 95\%$ detecting efficiency. The TOF provides very good particle identification at moderate momentum range, extends π/K separation from 0.7 GeV/c to 1.6 GeV/c and proton/(π,K) separation from 1.1 GeV/c to 3 GeV/c. Combining with TPC, it also provide electron identification at $p_T > 0.2$ GeV/c. This will improve low p_T J/ψ measurements at STAR a lot. This detector is still installing and will have $\sim 3/4$ coverage in RHIC year 2009 run and will be completed in RHIC year 2010 run.

The trigger system of the TOF detector is the two Pseudo Vertex Position Detectors (pVPD) or upgraded pVPDs (upVPD), each staying 5.4 m away from the TPC center along the beam line. They provide a stating timing information for TOF detectors and pseudo vertex position of each event.

Muon Chamber The STAR detector does not have any μ capability in original design until the TOF prototype's coming in. The STAR TOF can measure μ at very low momentum ($0.17 < p_T < 0.25$ GeV/c) where the time of flight difference between π and μ is big enough comparing to the timing resolution of the TOF [Abe08a]. This μ measurement in such limited p_T range only helps to extract the total charm cross section so far. To extend the μ capability, STAR is proposing a μ detector, Muon Telescope Detector (MTD). The MTD is similar with the STAR TOF, but has much larger readout and sits outside of the STAR magnet (with 2 times larger radius), using the BEMC and the magnet steel as absorber to stop electrons and hadrons. It has 40-50% detect efficiency including acceptance effect for μ at $p_T > 2$ GeV/c. The MTD prototype

has been put in from RHIC year 2007 run and works very well [Rua08, Sun08].

Trigger Detector The STAR trigger system is a 10 MHz pipelined system which is based on input from fast detectors to control the event selection for the much slower tracking detectors. The fast detectors that provide input to the trigger system are a central trigger barrel (CTB) at $|\eta| < 1$, zero-degree calorimeters (ZDC) located in the forward direction at $\theta < 2$ mrad and Beam-Beam Counter (BBC). The CTB surrounds the outer cylinder of the TPC, and triggers on the flux of charged-particles in the mid-rapidity region. It will be replaced by the TOF. The ZDCs are used for determining the energy in the neutral particles remaining in the froward directions. The BBC consists of a hexagonal scintillator array structure at ± 3.5 m from the nominal interaction point. It is the main device to make the relative luminosity measurement and to provide a trigger to distinguish $\vec{p}\vec{p}$ events from beam related background events by means of timing measurements.

2.2.1 Time Projection Chamber

The TPC is the primary tracking device of the STAR detector [And03]. It records the tracks of particles, measures their momenta, and identifies the particles by measuring their ionization energy loss (dE/dx).

Figure 2.5 shows the TPC structure schematically. It is 4.2 m long along the beam line and 4 m in diameter, sits in the STAR solenoidal magnet. It is an empty volume of gas in a well-defined, uniform, electric field of ~ 135 V/cm. The paths of primary ionizing particles passing through the gas volume are reconstructed with high precision from the released secondary electrons which drift to the readout end caps at the ends of the chamber. The uniform electric field which is required to drift the electrons is defined by a thin conduction Central Membrane (CM) at the center of the TPC, concentric filed-cage cylinders and the readout end caps.

The gas the STAR TPC used is P10 gas (10% methane, 90% argon) which has long

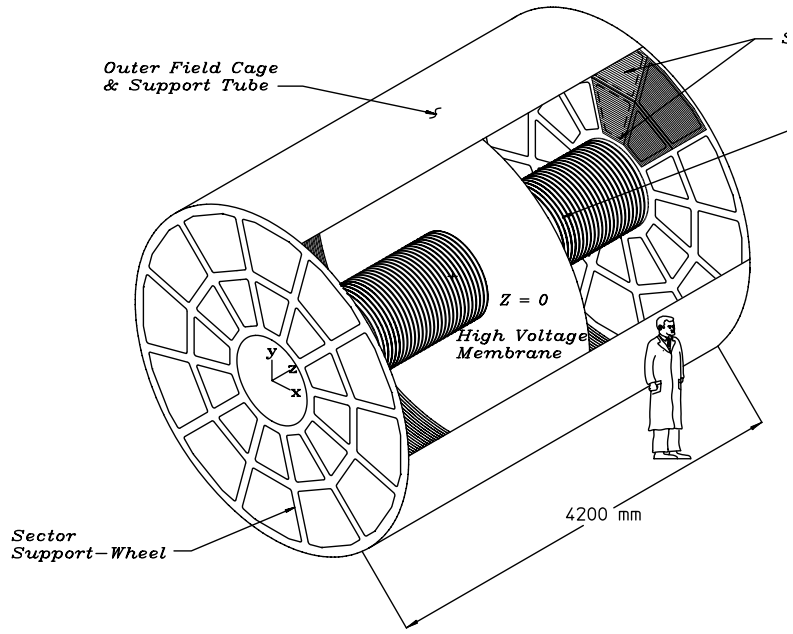

Figure 2.5: The schematcis of the STAR TPC.

been used in TPCs, regulated at 2 mbar above atmospheric pressure. The transverse diffusion of electrons in P10 is 230 $\mu m/\sqrt{cm}$ at 0.5 T or about $\sigma_T = 3.3$ mm after drifting 210 cm. The longitudinal diffusion of a cluster of electrons that drifts the full length of the TPC is $\sigma_L = 5.2$ mm. This sets the scale for the resolution of the tracking system in the drift direction.

The readout system in based on Multi-Wire Proportional Chamber (MWPC) with readout pads. The drifting electrons avalanche in the high filed at the 20 μm anode wires providing an amplification of 1000-3000. The chambers consists of a pad plane and three wire planes. Figure 2.6 shows the pad plane of one full TPC sector which is divided into two subsectors. The outer radius subsector have continuous pad coverage to optimize the dE/dx resolution. This is optimal because the full track ionization signal is collected and more ionization electrons improve statics on the dE/dx measurement. Another modest advantage of full pad coverage is an improvement in tracking resolution due to anti-correlation of errors between pad rows. The inner subsectors are in the

region of highest track density and thus are optimized for good two-hit resolution. This design uses smaller pads and the pad plane to anode wire spacing is reduced accordingly. The inner sector only serves to extend the position measurements along the track to small radii thus improving the momentum resolution and the matching to the inner tracking detectors. It also helps to detect particles with lower momentum. The parameters of the outer and inner subsectors are summarized in Table 2.2.1.

Table 2.3: Parameters of the TPC inner and outer subsectors.

Item	Inner subsector	Outer subsector	Comment
Pad size	2.85 mm × 11.5 mm	6.20 mm × 19.5mm	
Isolation gap between pads	0.5 mm	0.5 mm	
Pad rows	13	32	
Number of pads	1750	3942	5692 total
Anode voltage	1170 V	1390 V	20:1 signal:noise
Anode gas gain	3770	1230	

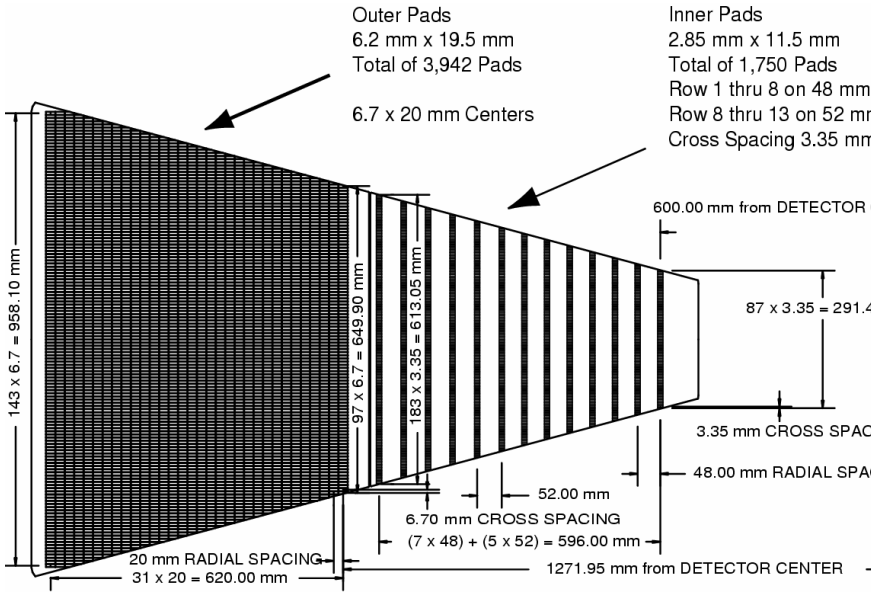

Figure 2.6: The anode pad plane of one full TPC sector. The inner subsector is on the right and it has small pads arranged in widely spaced rows. The outer subsector is on the left and it is densely packed with larger pads.

The track of primary particle passing through the TPC is reconstructed by finding ionization clusters along the track. The clusters are found separately in transverse plane and on the direction of beam line. The position resolution depends on the drift length

and the angle between the particle momentum and the drift direction and on the level of mm. After finding and associating the clusters along the track, it is fitted to track models. The track model is, to first order, a helix. Second-order effects include the energy lost in the gas which cause a particle trajectory to deviate slightly from the helix. The track is then be extrapolated to the other detectors and the points from other detectors might be added. At the end this track is then fitted with a more sophisticated fitting method and from there on is called a global track. Once all of the global tracks from the same event have be reconstructed, the primary vertex of this event can be reconstructed with pretty good accuracy. The vertex resolution inversely proportional to the square root of the number of tracks in the calculation and can reach 350 μm in central Au+Au collisions. After getting the primary vertex, a track which originates from the primary vertex can be refitted using the primary vertex as additional point. If the distance of closest approach (dca) of a global track is small enough (< 3 cm for example) and the refitting works out well then this refitted track is marked as primary track and stored into a separated collection for further use. The momentum resolution of primary track in $p + p$ collisions is approximately $\Delta p_T/p_T \approx 1\% + 0.5\% \times p_T$.

Energy lost in the TPC gas is a valuable tool for identifying particle species. The dE/dx is extracted from the energy loss measured on up to 45 padrows. The length over which the particle energy loss is measured is too short to average out ionizations fluctuations and it is not possible to accurately the average dE/dx. Instead, the most probable energy is measured. This is done by removing the largest ionization clusters. Figure 2.7 shows the 70% truncated mean dE/dx distribution. It's resolution is less than 8%, which makes the π/K separation up to p $\sim$ 0.7 GeV/c and proton/meson separation up to p $\sim$ 1.1 GeV/c. The TPC is originally designed to identify particles at low momentum, but the separation of dE/dx of particles at relativistic rising region also allows people to identified particles at high momentum ($p > 3$ GeV/c) [Sha06, Xu08]. This method is especially more powerful for high momentum electron, which is much more difficult to be identified at low momentum. The e/π (e/K) separation is approximately 3σ (5σ) at $p_T = 3$ GeV/c and 2σ (3.5σ) at $p_T = 10$ GeV/c [Xu08].

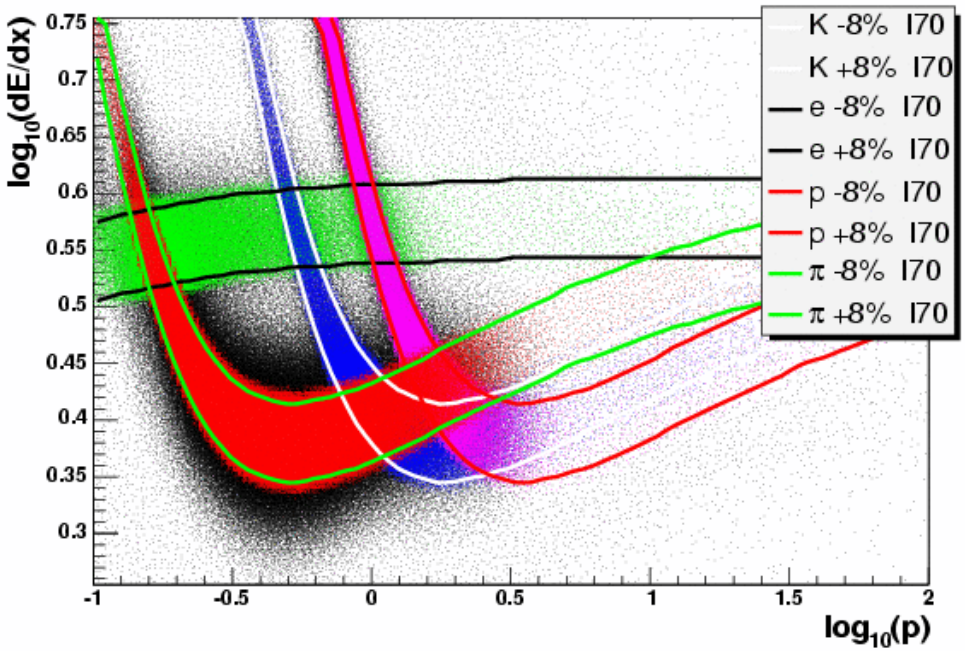

Figure 2.7: Distribution of $log_{10}(dE/dx)$ as a function of $log_{10}(p)$ for electrons, pions, kaons and protons. The units of dE/dx and momentum are keV/cm and GeV/c, respectively. The color bands denote within $\pm 1\sigma$ the dE/dx resolution. $I70$ means Bichsel's prediction for 30% truncated dE/dx mean.

2.2.2 Barrel Electro-Magnetic Calorimeter

The STAR TPC is nominally a slow detector, its Data AcQuisition (DAQ) rate is less than 100 Hz. The STAR BEMC is a fast detector, allows STAR to trigger on and study rare, high p_T processes (jets, leading hadrons, direct photons, heavy quarks) and provide large acceptance for photons, electrons, π^0, η, J/ψ , Υ mesons in systems spanning polarized $p+p$ through Au + Au collisions.

The BEMC is located inside the aluminum coil of the STAR solenoid, between the TPC and the magnet coils, and covers $|\eta| \leq 1$ and 2π in azimuthal, matching the acceptance for full TPC tracking. The inner surface of the BEMC has a radius of about 220 cm and parallel to the beam axis.

The design for the BEMC includes a total of 120 calorimeter modules, each subtending 6° in $\Delta\phi$ (~ 1 rad) and 1.0 unit in $\Delta\eta$. These modules are mounted 60 in ϕ and 2 in η. Each module is roughly 26 cm wide by 293 cm long with an active depth of

23.5 cm plus $\sim$ 6.6 cm in structural plates (of which $\sim$ 1.9 cm lies in front of the detector). The modules are further segmented into 40 towers, 2 in ϕ and 20 in η, with each tower subtending 0.05 in $\Delta\phi$ by 0.05 in $\Delta\eta$. The full BEMC is thus physically segmented into a total of 4800 towers. Each of these towers in projective and points back to the center of the TPC. Figure 2.8 shows a schematic side view of a module illustrating the projective nature of the towers in the η direction.

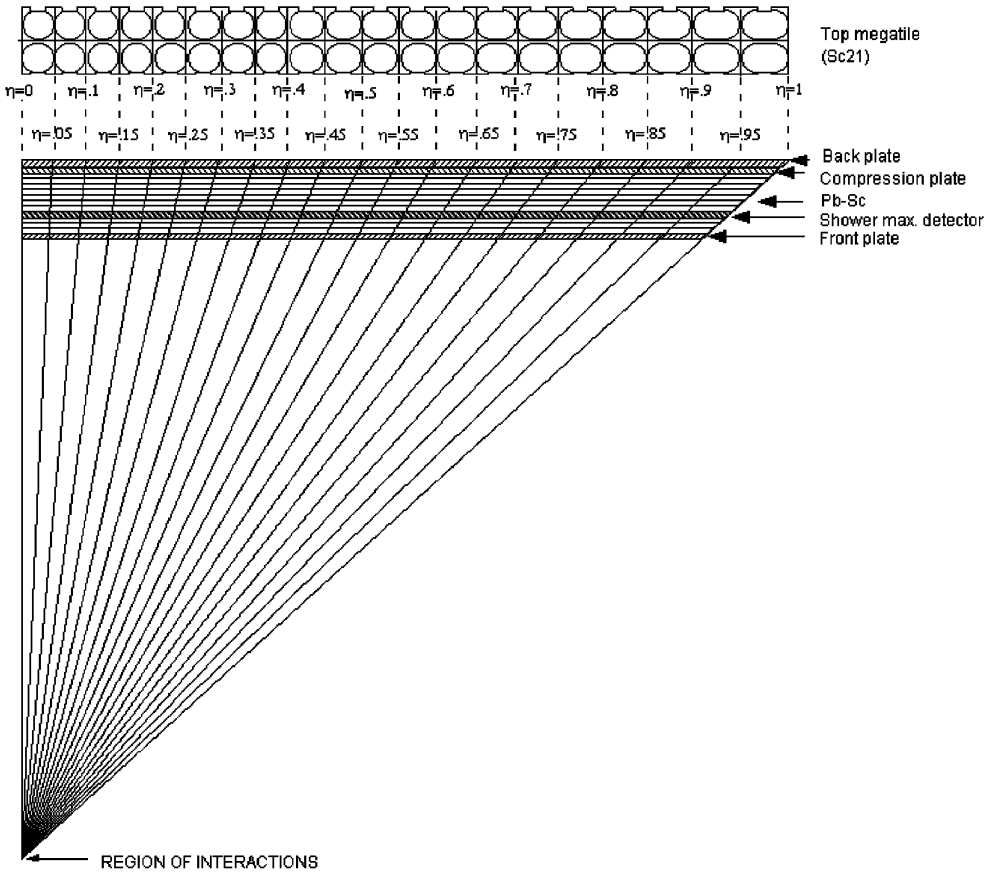

Figure 2.8: Side view of a calorimeter module showing the projective nature of the towers. The 21st mega-tile layer is also shown in plan view.

The BEMC is a sampling calorimeter using lead and plastic scintillator because of the large area and complex geometry. Figures 2.9 shows an end view of a module showing the mounting system and the compression components. The core of each BEMC module consists of a lead-scintillator stack and shower maximum detectors situated approximately 5 radiation lengths from the front of the stack, which will be discussed in the next section (sec. 2.2.3). There are 20 layers of 5 mm thick lead, 19

layers of 5 mm thick scintillator and 2 layers of 6 mm thick scintillator. The thicker scintillator layers are associated with the preshower detector which is significantly helpful in both π^0/γ and electron/hadron discrimination. Since the preshower detector calibration is unavailable until 2008, it is not used in this analysis.

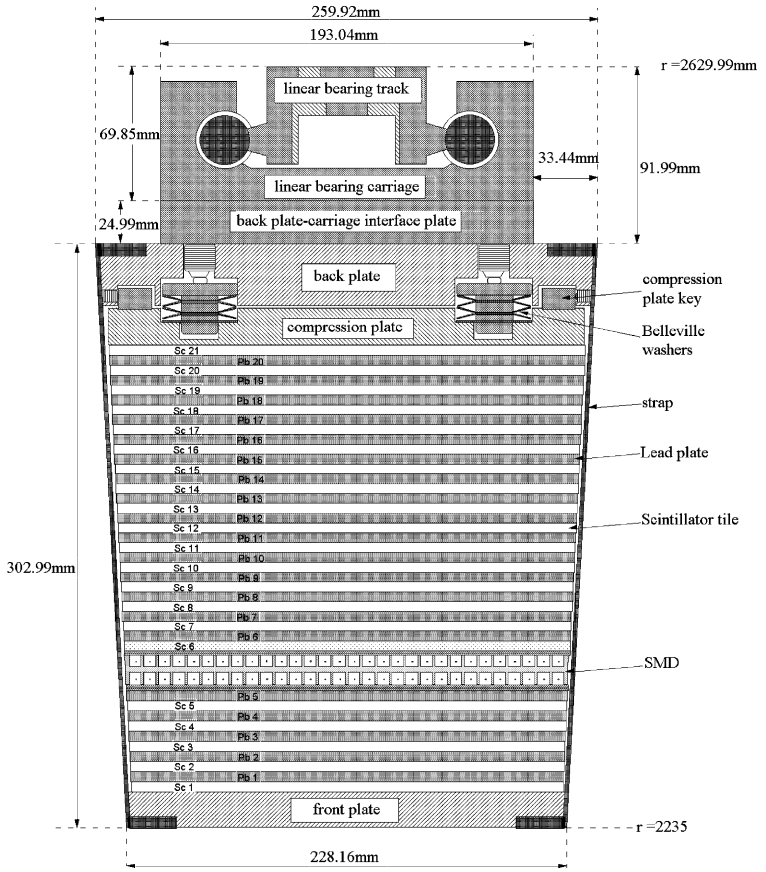

Figure 2.9: Side view of a STAR BEMC module showing the mechanical assembly including the compression components and the rail mounting system. Shown is the location of the two layers of shower maximum detector at a depth of approximately $5X_0$ from the front face at $\eta = 0$

The BEMC has a total depth of ∼20 radiation length (20 X_0) at $\eta = 0$. The intrinsic energy resolution of tower is $\sigma_E/E \approx 1.5\% \oplus 14\%/\sqrt{E}$. The hadron background can decrease the effective resolution. In central Au+Au collisions, the resolution for electron energy at 1.5 GeV and 3 GeV is around 17% and 10%, respectively [Bed03].

2.2.3 Barrel Shower Maximum Detector

The STAR BEMC has segmentation (towers) significantly larger than an electromagnetic shower size. Each of its 4800 towers span $\Delta\phi \times \Delta\eta = 0.05 \times 0.05$ which at the radius of the inner face of the detector correspond to tower size $\sim 10 \times 10$ cm^2 at $\eta = 0$ increasing towards $\eta = 1$. Its provides precise energy measurement for isolated electromagnetic showers but its spatial resolution is not fine enough to measure the shower shape and shower size to distinguish direct γ and π^0. The BSMD with high spatial resolution is embedded in the BEMC to satisfy this requirement [Bed03].

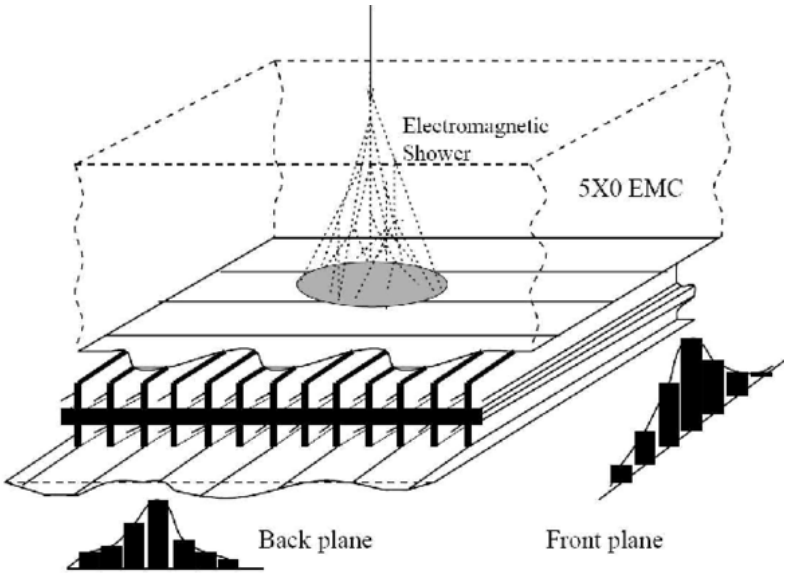

Figure 2.10: Schematic illustration of the double layer STAR BSMD. Two independent wire layers, separated by an aluminum extrusion, image electromagnetic shoers int the η and ϕ on corresponding pad layers.

The conceptual design of the SMD is shown in Fig. 2.10. The BSMD is located at about 5 radiation length depth in the calorimeter modules, at $\eta = 0$, including all material immediately in front of the calorimeter. A unique feature of the STAR SMD is its double layer design. A two sided aluminum extrusion provides ground channels for two independent planes of proportional wires. Independent PC Board cathode planes with strips etched in the η and ϕ directions, respectively, allowing reconstruction of a two dimensional image of the shower. The SMD is a wire proportional counter-strip readout detector using gas amplification. The basic structure of the detector is an

aluminium extrusion with 5.9 mm wide channels running in the η direction. There are 50 μm gold-plated tungsten wires in the center of the extrusion channels. The detector strips sense the induced charge from the charge amplification near the wire. One set of strips is perpendicular to the wires, making up one side of the channel around the wire outside the aluminum extrusion, and provide an image of the shower spatial distribution in the η direction. Each of these strips span 30 channels (30 wires). They have size of 0.1 rad in ϕ ($\approx 23cm$, i.e. the module width) and 0.0064 in η ($\approx$ 1.5 cm at low η). The other set of strips are parallel to the wire channels of the aluminum extrusion. These stripes are physically 1.33 cm wide and have lengths 0.1 units in η, while the wires are 1.0 units in η.

The BSMD has an approximately linear response versus energy, at the depth of $5X_0$ inside the EMC, in the energy range from 0.5 to 5 GeV. The ionization at the back plane of the BSMD is about 10% lower than the front plane. The energy resolution in the front plane is given approximately by $\sigma_E/E = 12\% + 86\%/\sqrt{E}\ [GeV]$ with he energy resolution on the back plane being 3-4% worse. The position resolution in the front and back planes are given approximately by $\sigma_{front} = 2.4\ mm + 5.6\ mm/\sqrt{E}\ [GeV]$ and $\sigma_{back} = 3.2\ mm + 5.8\ mm/\sqrt{E}\ [GeV]$.

CHAPTER 3

High-p_T J/ψ Transverse Momentum Distributions

J/ψ is usually reconstructed through di-electronic channel or di-muon channel in the world. To date, STAR has only tried to reconstructed J/ψ through its di-electronic channel since there is no muon detector in STAR so far. The previous J/ψ reconstruction in STAR using TPC [Gon, Cos08] was limited to low p_T with low efficiency, limited sample luminosity and large background. Even PHENIX, which is originally designed for leptonic measurements, has difficulty to push the J/ψ spectra to high p_T [Adl04a, Ada07a, Ada07b, Ada08]. This chapter is dedicated to detailed description of the analysis for the high-p_T J/ψ reconstruction by using the BEMC triggered data in STAR.

3.1 Data Sets and Trigger

The typical luminosity - cross-section of the beam-beam collision per second - achieved at RHIC is much higher (on the level of several order of magnitude) than the event recording rate of slow tracking detectors, such as the STAR TPC. The slow STAR detector subsystems only operate at event rates lower than 100 Hz. The actual interaction rates are in the order of 1 Mhz for p+p collisions and 100 Khz for Au+Au collisions. There is room for the fast detectors to select (or trigger) on interesting events for the slow detector to be read out. The BEMC is one of the fast detectors, which is usually used to trigger on rare and/or high p_T processes (jets, leading hadrons, direct photons, heavy quarkonia, etc.). There are two types of triggers from the EMC front-end electronics. One set of trigger, called "patch trigger", consistent of 300 tower

sums from patches of 0.2×0.2 in $\eta - \phi$. The other set of trigger, called "high-tower trigger", is up to 300 high-tower energy values from the single largest 0.05×0.05 tower signal within each 0.2×0.2 patch. These primitives are processed and passed to the trigger electronics to make final trigger decisions. Of interest to the analysis in this dissertation is the high tower trigger. Events with an energy deposition in a single tower of the BEMC above a certain threshold can be selected to enhance the sample of events, in which a high transverse momentum electron or photon is produced. The reason we use this trigger to reconstruct the high-p_T J/ψ is explained in Fig. 3.8. The figure shows the p_T correlations between the daughters from high-p_T J/ψs decay in PYTHIA. Significant fraction of the high-p_T J/ψs have a high p_T electron daughter (for example p_T¿2.5 GeV/c). This means that the trigger, which enriches high p_T electron sample, also enriches high p_T J/ψ sample.

Table 3.1: Data sets used in this analysis.

	$p+p$ (2005)	$p+p$ (2006)	Cu + Cu
Minimum bias trigger	BBC	BBC	ZDC
EMC trigger threshold	$E_T > 3.5$ GeV	$E_T > 5.4$ GeV	$E_T > 3.75$ GeV
Sample luminosity	2.8 pb^{-1}	11.3 pb^{-1}	860 μb^{-1}
pp-equivalent luminosity	2.8 pb^{-1}	11.3 pb^{-1}	3.4 pb^{-1}
Number of events	3.44 M	2.97 M	3.12 M

The STAR BEMC started to operate in year 2003 but its coverage was limited to 1/4 of the TPC coverage at that time. It started to sample enough luminosity for this analysis from year 2005. Table 3.1 lists all of the data sets used in this analysis. The high tower triggered data also requires an event satisfy a minimum-bias trigger concurrently. The minimum-bias trigger in Cu + Cu collisions requires a coincidence between the ZDCs. The minimum-bias trigger in $p+p$ collisions requires a coincidence between the BBCs. Centrality definition in Cu + Cu was based on the uncorrected charged particle multiplicity at mid-rapidity ($|\eta| < 0.5$). The 0-60% and 0-20% of the geometric cross section are selected by requiring $dN_{ch}^{raw}/d\eta \geq 19$ and $dN_{ch}^{raw}/d\eta \geq 98$ respectively.

3.2 Electron Identification

TPC is the main detector in STAR for tracking and identifying charged particles as discussed in section 2.2.1. To reconstruct J/ψ with good mass resolution and signal to background ratio, both excellent tracking and electron identification are needed.

3.2.1 Track selection

Since the lifetime of the J/ψs is so small that they decay very close to the event primary vertex, we are interested in electrons originating from the primary vertex. A primary charged track includes the event primary vertex into the track fitting to get good momentum resolution, as discussed in sec. 2.2.1. Furthermore, the distance of closet approach (DCA) to the event primary vertex of its associated global track is required to be smaller than certain value to reject 1) tracks from different collisions which mostly have different primary vertex, 2) tracks decayed from resonance with long lifetime like K_S, Λ, Ξ, Ω and etc., 3) tracks scattered by beam pipe, and etc. In principle, the electrons decayed from J/ψ should have DCA$\sim$0 cm. However, since the silicon detectors (inner tracker) are not included into the tracking in the data sets for this analysis and the first TPC measured points are at least 50 cm away from the event primary vertex, the resolution of DCA is on the order of centimeter, depending on p_T. Therefore, we require that an electron candidate have $DCA < 1$ cm at high p_T and $DCA < 3$ cm at lower p_T. To ensure good momentum resolution, number of TPC hits used in tracking is required to ≥ 25 (45 in maximum). This requirement also suppresses the possibility of selecting duplicated short tracks from track splitting. Charged tracks within a pseudo-rapidity window $|\eta| < 1.0$ are selected to be within the TPC coverage.

3.2.2 dE/dx from the TPC

The ionization energy loss (dE/dx) of a charged particle traversing TPC provides powerful hadron rejection for electron candidates. As discussed in sec. 2.2.1, the TPC

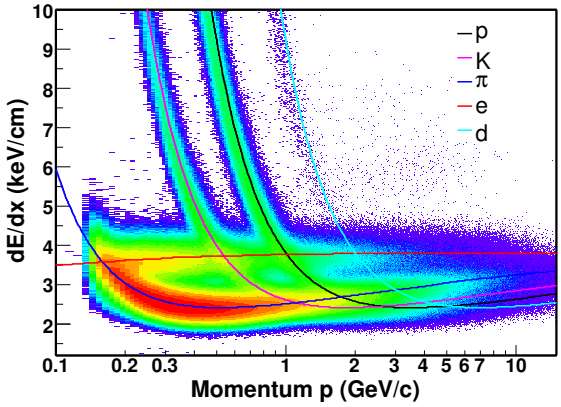

Figure 3.1: The distribution of dE/dx versus momentum for BEMC triggered data in 2006 $p+p$ collisions.

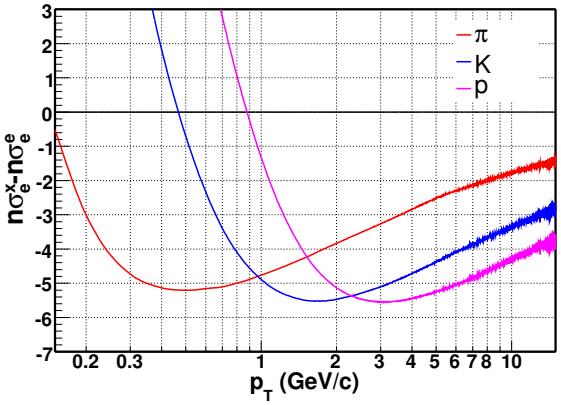

Figure 3.2: nσ_e difference between e/π, e/K and e/p expected from Bichsel function as a function of p_T.

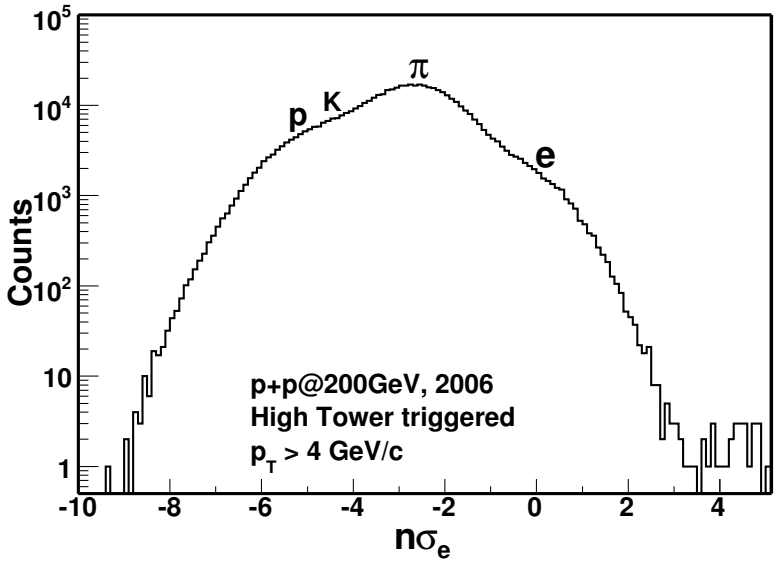

Figure 3.3: nσ_e distribution for high p_T tracks in $p+p$ 2006 high tower triggered data. The tracks are selected through the cuts discussed in detail in the text.

also measures dE/dx with the 70% truncated mean for each track. Figure 3.1 shows the dE/dx distribution as a function of momentum in high tower triggered data in 2006 p+p data. The high-tower trigger enhances high p_T particles especially electrons. The ionization energy loss by charged particles in material is given by the Bethe-Bloch formula and for thin material by the more precise Bichsel formula. The predictions for electron, pion, kaon, proton and deuteron are plotted on Fig. 3.1. They describe the data well. The electron identification is difficult at low p_T because the electron band crosses several hadron bands. To quantitatively describe the particle identification, the variable $n\sigma_x$ ($x = \pi, K, p, e$, etc.) is defined as:

$$n\sigma_x = \frac{1}{R} log \frac{dE/dx_{measured}}{\langle dE/dx \rangle_x}, \tag{3.1}$$

where $dE/dx_{measured}$ is the measured mean dE/dx for a track, $\langle dE/dx \rangle_x$ is the expected mean dE/dx from Bichsel formula for charged particle x with a given momentum, and R is the dE/dx resolution, which depends on the characteristics of each track, such as number of hits measured in the TPC used for dE/dx measurement, the pseudorapidity of a track. To obtain good dE/dx resolution, we have required number of dE/dx hits included in the truncated mean method to be ≥ 15. Figure 3.2 shows the difference of $n\sigma_e$ between electron and charged hadrons (π, K, p). Clearly, the e and π separation is within 3σ at $p_T < 0.2$ GeV/c, the e and K separation is within 3σ at $0.35 < p_T < 0.65$ GeV/c and the e and p separation is within 3σ at $0.7 < p_T < 1.2$ GeV/c. There is little p_T range at low p_T where the electron band significantly separates from the other hadrons. At higher p_T, the situation gets better. The electron band is above all of the three hadron bands. However, the electron yield is too low to be easily identified in almost the whole p_T range. In non-single diffractive $p + p$ collisions at 200 GeV, the electron/hadron ratio is $\sim 1/10$ at $p_T \sim 0.2$ GeV/c and drops to ~ 0.007 at $p_T > 1$ GeV/c. Figure 3.3 shows the $n\sigma_e$ distribution at $p_T > 4$ GeV/c in high tower triggered data from 2006 $p + p$ collisions at 200 GeV. There are three visible bumps, the left one corresponds to kaons and protons, the middle one corresponds to pions and the

right one corresponds to electrons. Even at such high p_T and with the electron enhanced data sets, the electron/hadron ratio is still $< 1/10$ and there are substantial hadron contaminations under the electron dE/dx peak. For the high p_T J/ψ reconstruction, we demand at least one very pure electron daughter at high p_T. Therefore, EMC not only provides the necessary trigger but also is crucial for the electron identification.

3.2.3 Energy from the BEMC towers

When a high energy electron incidents on a thick absorber, it initiates an electromagnetic cascade as bremsstrahlung – electromagnetic radiation produced by the deceleration of the electron. The electron will continue to radiate photons while the produced high energy photons produce electrons and positrons through the pair production. These two processes continue alternatively, until electrons eventually fall below the critical energy, where the ionization energy loss starts to dominate over the energy loss by bremsstrahlung, and dissipate their energy by ionization and atomic excitation rather than by the generation of more shower particles. The BEMC towers have about 21 radiation lengths. It is thick enough to collect almost all of the energy of an electron.

When a high energy hadron passes through a material, it produces several lower-energy hadrons through the interaction with the nuclei via the strong interaction and continues with the electromagnetic shower due to π^0 production and low energy hadronic activity. The cross-section of hadron-nucleus interaction is much smaller than the bremsstrahlung of a high energy electron. Thus in STAR BEMC, a significant fraction, $\sim 30 - 40\%$ of high energy charged hadrons do not deposit any amount energy via the nuclear iterations and only deposits $\sim 250 - 350$ MeV of equivalent energy in the calorimeter due largely to electromagnetic ionization energy loss. These hadrons are so-called "Minimum Ionizing Particles" (MIP) producing "MIP hits" in the BEMC towers. The energy deposition of non-showering, high p_T hadrons is approximately constant, independent of momentum and particle species, and provide a convenient

calibration reference [CPR02]. Even for those hadrons with showers, most of them can not deposit all of their energy into the BEMC, which is approximately one hadronic interaction length.

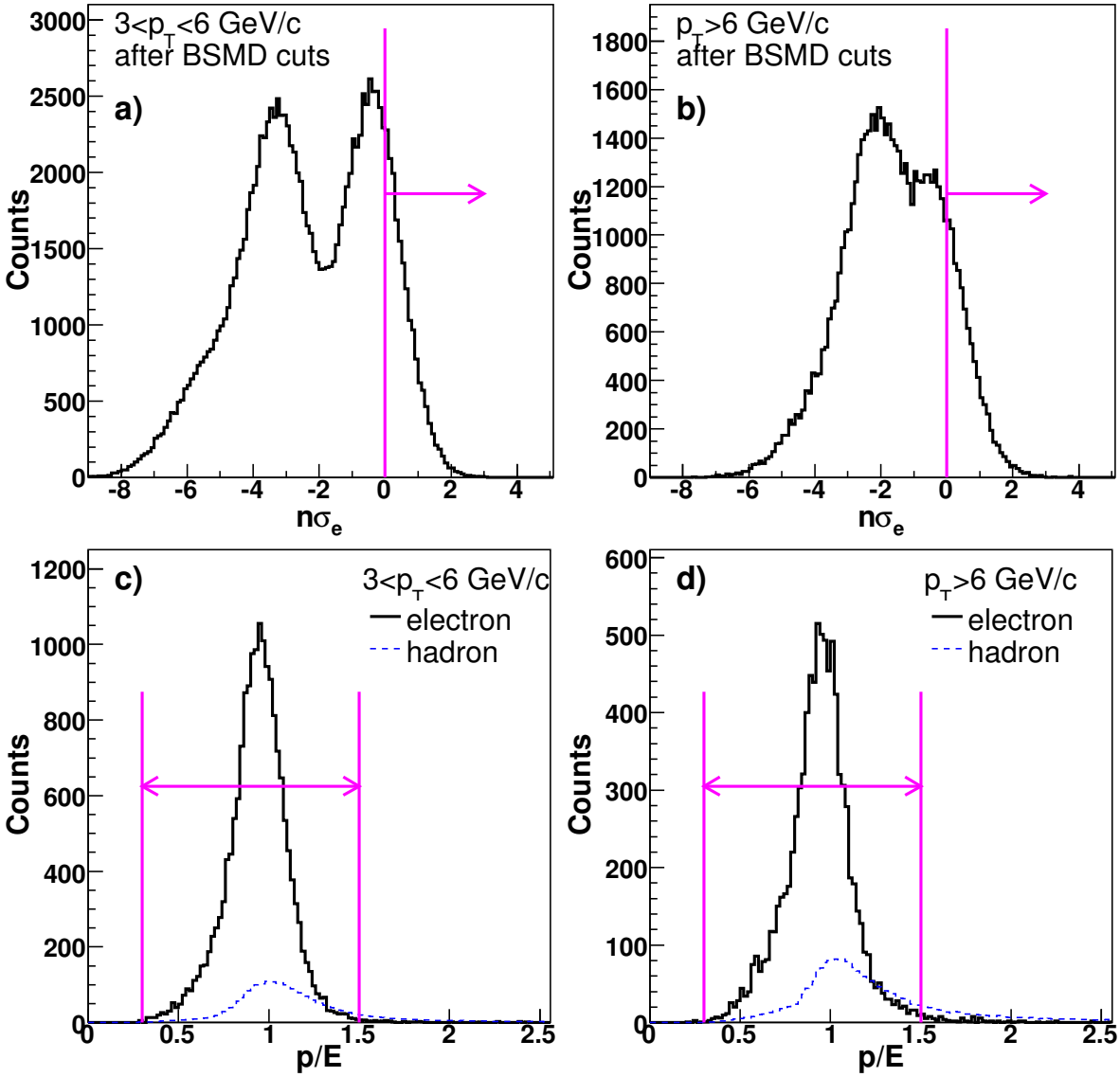

Figure 3.4: The $n\sigma_e$ distribution (a,b) and the p/E distributions for electrons (solid histogram) and hadrons (dashed histogram) (c,d). The arrows depict the cuts. See text for detail.

The different BEMC responses to electrons and hadrons can be used to help electron identification. The TPC reconstructed charged tracks with $p_T > 1.5$ GeV/c are extended to the BEMC tower inner plane, the BSMD η plane and the BSMD ϕ plane

respectively and the corresponding tower energy E from the struck tower. The detailed procedure can be found in [Don]. Then the energy E is compared to the momentum p measured by TPC. For electron, the p/E ratio should be peak at unity. While for the hadron, the p/E ratio should have a broad distribution and has some possibility to be very large for the non-showering hadrons. To study the electron efficiency and hadron rejection on p/E cut, one has to select an electron sample and a hadron sample. Since the hadron yield is dominated over electron yield, the hadron sample can be simply selected by requiring $n\sigma_e < -2$, which means that the dE/dx is 2 σ below the electron expected dE/dx. As discussed in sec. 3.2.2, a pure electron sample is more difficult to get. The information from BEMC is needed to get further hadron rejection. Figure 3.4.a and 3.4.b show the $n\sigma_e$ distributions after BSMD shower shape and shower position cuts. The electrons and hadrons are clearly separated. We select the electron sample for the p/E study by requiring $n\sigma_e > 0$. The electron purity in this sample is $> 95\%$. Figure 3.4.c and 3.4.d show the p/E distributions for electron samples (solid histograms) and hadron samples (dashed histograms) at $3 < p_T < 6$ GeV/c and $p_T > 6$ GeV/c. The dashed histograms are scaled to match the entries with that of the solid histograms. The p/E distributions are approximately a Gaussian distribution, peaking at ~ 1 with $\sigma \sim 0.15$. For the hadrons, the height at ~ 1 is much lower than that for electrons, and has a long tail on the right-hand side. In addition, hadrons with energy deposit below the trigger energy threshold have already been rejected by the high-tower trigger. We cut on the p/E between 0.3 and 1.5 to select electrons for the high-p_T J/ψ analysis. The cuts are shown as arrows on the plots.

3.2.4 Information from the BSMD

The BSMD is embedded in the BEMC at the depth $\sim 5X_0$, where the electromagnetic showers from electrons and photons have their maximum spatial extent. But the hadronic showers typically incompletely develop at this depth. Therefore, the number of BSMD hits produced by hadrons, in general, is smaller than those produced by electrons. The resulting difference of the number of BSMD hits is used for additional

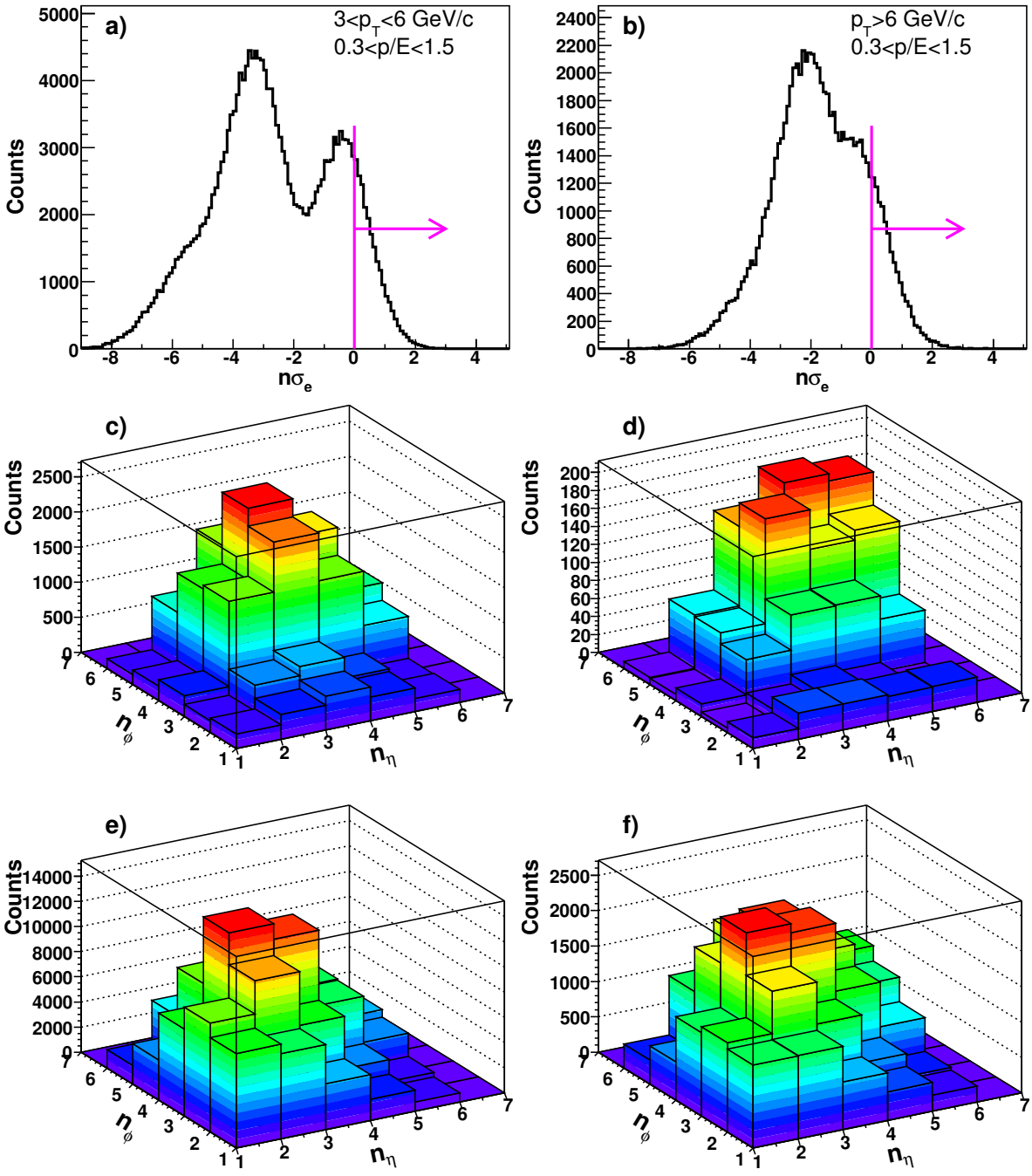

Figure 3.5: **Panel a,b:** $n\sigma_e$ distribution after track quality cuts and tower energy cut at $3 < p_T < 6$ GeV/c and $p_T > 6$ GeV/c.
Panel c,d: The number of stripes fired on the BSMD η and ϕ plane for electrons.
Panel e,f: The number of stripes fired on the BSMD η and ϕ plane for hadrons.

hadron rejection. Figure 3.5.a and 3.5.b show the $n\sigma_e$ distribution after tower energy cuts. We select a electron sample by requiring $n\sigma_e > 0$ denoted on the plots for the BSMD cuts study. The middle panels of Fig. 3.5 are the number of stripes fired on the η plane and ϕ plane for electrons. The bottom panels of Fig. 3.5 are the number of stripes fired on the η plane and ϕ plane for hadrons. The difference of number of BSMD hits between electrons and hadrons can be clearly seen. We require $n_\eta \geq 2$ and $n_\phi \geq 2$ for electron candidates for this high p_T J/ψ analysis.

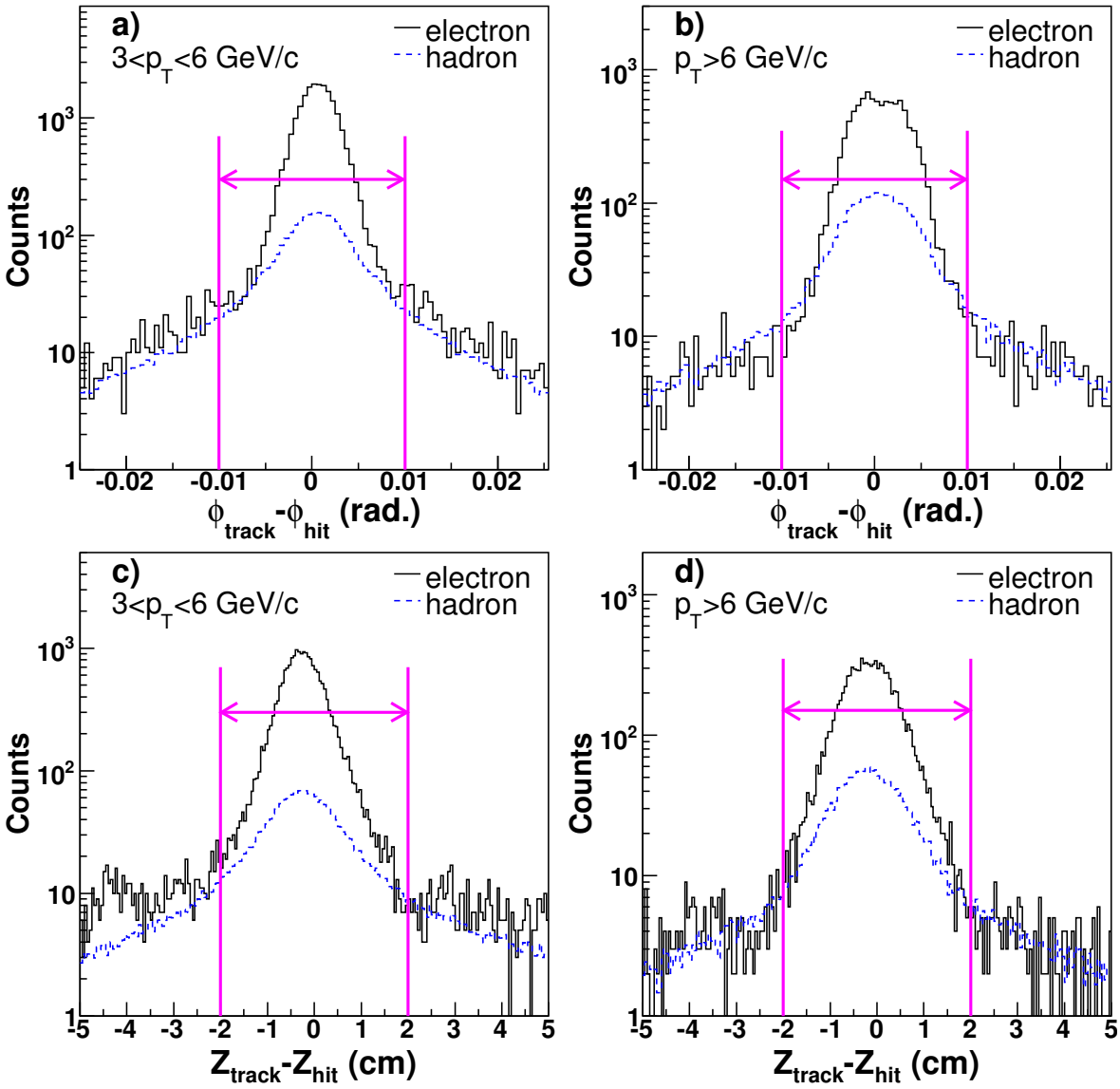

Figure 3.6: The distance between TPC track projection and the reconstructed BSMD hits position on ϕ and η plane for electrons and hadrons. The arrows denote the cuts we set.

Besides the shower size measured by BSMD, the shower center position measured by the BSMD can also be used for additional hadron rejection. We compare the distance between the TPC track projection position on BSMD η and ϕ planes and the reconstructed BEMC point position. The distance has a much wider distribution for hadrons than for electrons. Figure 3.6 shows the distributions of the difference between the projected track position and the BSMD reconstructed shower position in ϕ direction (upper panels) and Z (η) direction (bottom panels) for electrons and hadrons. Again, the histograms for hadrons are scale to match the entries with that of the electrons. The peak region of the distance distribution for electrons are from the real electromagnetic shower while the tails are mostly from random association between TPC tracks and the BEMC hits. The tails for electrons and hadrons match very well on both directions at different p_T range. But the resolution of the peak region for electron is much narrower than that for hadrons. The cuts denoted as arrows on the plot remove the contribution from random association, and also reject some hadrons.

3.2.5 All electron cuts combined

Table 3.2: The summary of the electron identification cuts.

Parameter	cut	Comments
# fit points	≥ 25	ensure good momentum resolution
global DCA	< 1 cm	
pseudorapidity η	(-1,1)	
# dE/dx points	≥ 15	ensure good dE/dx resolution
$n\sigma_e$	(-2,5)	
p/E	(0.3,1.5)	BEMC tower energy
n_η	≥ 2	number of strips fired on BSMD η plane
n_ϕ	≥ 2	number of strips fired on BSMD ϕ plane
$\phi_{track} - \phi_{hit}$	(-0.01,0.01) rad.	distance between track projection and BSMD hits
$Z_{track} - Z_{hit}$	(-2,2) cm	distance between track projection and BSMD hits

Figure 3.7 shows how the $n\sigma_e$ distribution changes when the cuts on the BEMC tower energy and BSMD shower size and shower position applied one by one. The BEMC and BSMD electron identification cuts dramatically reduce hadron contamination without reducing electron sample. The ratio of the electron signal to the

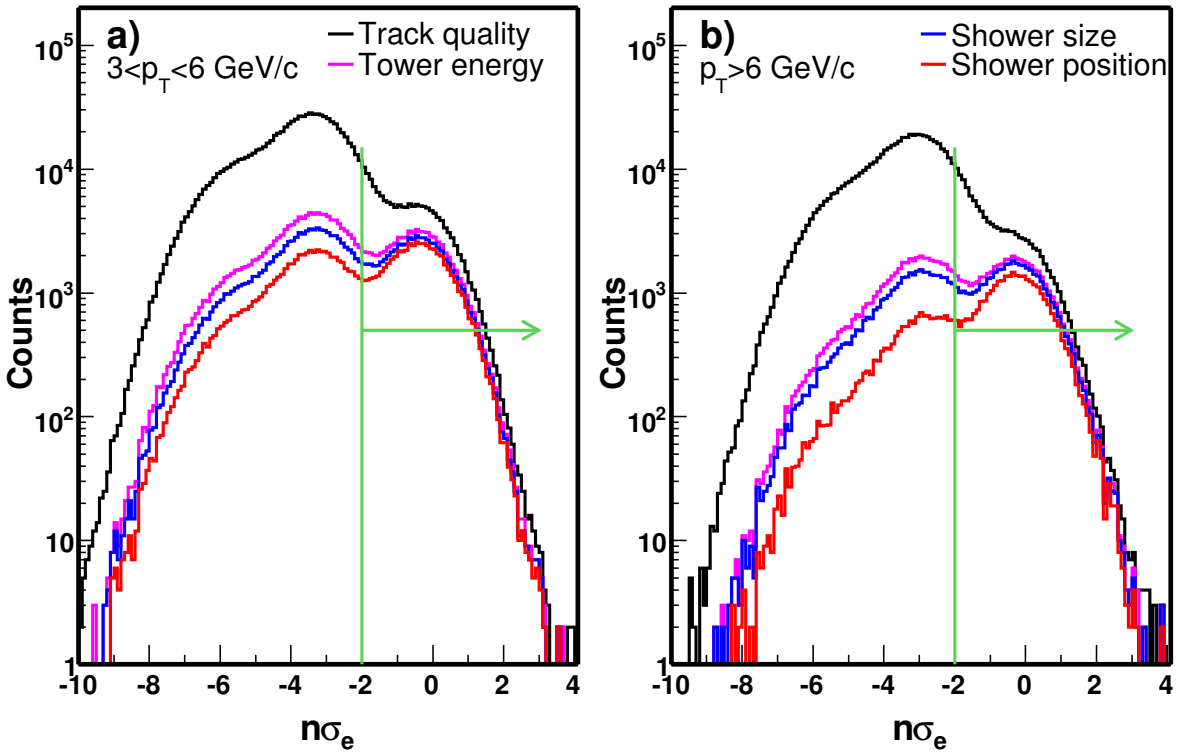

Figure 3.7: The $n\sigma_e$ distributions of the tracks after applications of TPC quality cuts, BEMC tower energy cut and BSMD measured shower size and shower position cuts.

hadron contamination is dramatically enhanced after all of the cuts are applied, and the electron peak and hadron peak are well separated. The cuts are summarized in Tab. 3.2. After all of the cuts, we select the track with $-2 < n\sigma_e < 5$ as our electron candidates to reconstruct the high p_T J/ψ. The purity of electron in this sample is $> 90\%$ at $p_T < 5$ GeV/c and decrease to $\sim 70\%$ at $p_T = 8$ GeV/c. Since this kind of electron candidates are identified by combining information from TPC and EMC, we call them 'EMC+TPC' electrons.

3.3 High p_T J/ψ Reconstruction

Once getting the electron candidates, one can start to reconstruct the J/ψ. But the electron candidates we got in the last section are triggered by the BEMC and identified by the combining information from TPC and BEMC. These 'EMC+TPC' electrons usually have high p_T, corresponding to the energy threshold of the online trigger list in

Table 3.3: The summary of the cuts for 'TPC only' electron candidates.

Parameter	cut	Comments
# fit points	≥ 25	ensure good momentum resolution
global DCA	< 3 cm	
pseudorapidity η	(-1,1)	
# dE/dx points	≥ 15	ensure good dE/dx resolution
$n\sigma_e$	(-2,2)	

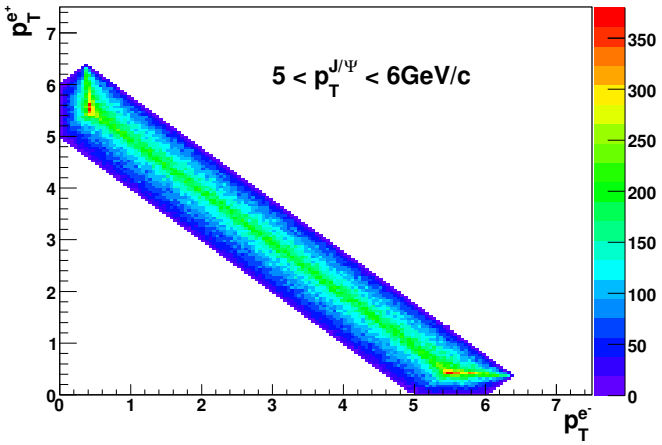

Figure 3.8: p_T correlations between daughters decayed from high-p_T J/ψ in PYTHIA.

Tab. 3.1. We also apply off-line p_T cut on this electron candidates listed in Tab. 3.4. But as shown in Fig. 3.8, the high p_T J/ψs decay into one high p_T electron and one electron with lower p_T. The efficiency for J/ψ reconstruction with only 'EMC+TPC' electron candidates is very small. We reconstruct the high p_T J/ψ by pairing the 'EMC+TPC' electrons with the electrons with lower p_T ($p_T \gtrsim 1.2$ GeV/c), which can be identified by TPC dE/dx only with reasonable hadron rejection (purity is $\sim 90\%$ with particle identification efficiency $> 95\%$). The detailed cuts for these electron candidates are listed in Tab. 3.3. There are several advantages to have the p_T cut on the lower p_T electron candidates (called 'TPC only' electrons). The $p_T \gtrsim 1.2$ GeV/c will not lose much high p_T J/ψ signals but significantly reduce background from misidentification and random combination (namely QCD background).

We paired every 'EMC+TPC' electron with all of the 'TPC only' electrons with opposite charge in the same event and calculated the invariant masses of the pairs by

Table 3.4: Table of the trigger conditions, off-line cuts and information of J/ψ signal. E_T is the BEMC trigger threshold. p_{T1} and p_{T2} are the high p_T and lower p_T of the electron pair.

	$p+p$ (2005)	$p+p$ (2006)	Cu + Cu
MB trigger	BBC	BBC	ZDC
E_T (GeV)	> 3.5	> 5.4	> 3.75
Sample luminosity	2.8 pb^{-1}	11.3 pb^{-1}	860 μb^{-1}
p_{T1} (GeV/c)	> 2.5	> 4.0	> 3.5
p_{T2} (GeV/c)	> 1.2	> 1.2	> 1.5
J/ψ p_T (GeV/c)	5-8	5-14	5-8
J/ψ counts	32 ± 6	51 ± 10	23 ± 8
S/B	9:1	2:1	1:4

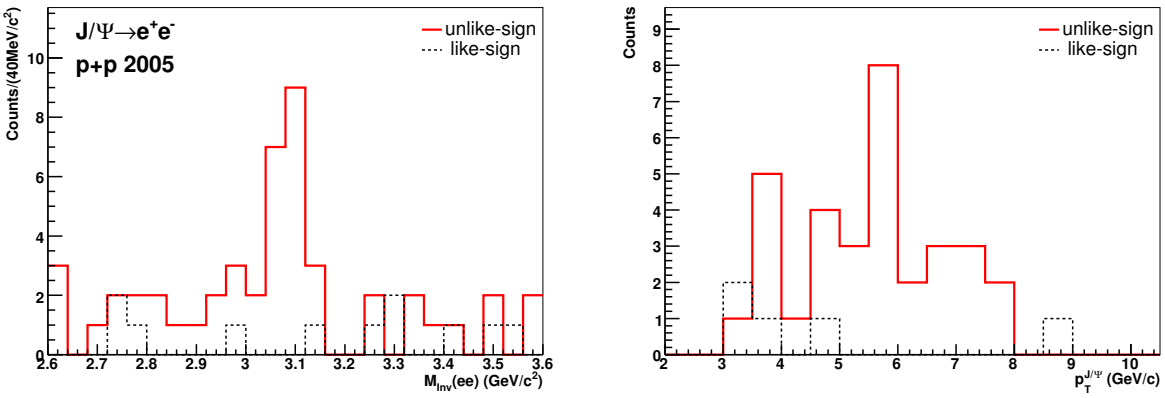

Figure 3.9: **Left:** Invariant mass distribution of unlike-sign (solid line) and like-sign (dashed line) electron pairs from 2005 $p+p$ data.
Right: Raw p_T distribution of unlike-sign (solid line) and like-sign (dashed line) electron pairs with $2.7 < M_{inv}(ee) < 3.2$ GeV/c^2

using the momentum vectors measured by the TPC. The solid line on the left panel of Fig. 3.9 shows the invariant mass distributions from 2005 $p+p$ data. A significant excess is clearly visible in the J/ψ mass region ($M = 3.096$ GeV/c^2). The background in this distribution is mainly from: (i) hadrons misidentified as electrons, (ii) electrons decayed from other heavy flavor resonances such as D-mesons and B-mesons, or Drell-Yan process and etc. (iii) electrons from gamma conversion ($\gamma \rightarrow e^+ + e^-$), (iv) electrons from π^0 Daliz decay ($\pi^0 \rightarrow \gamma + \gamma*, \gamma* \rightarrow e^+ + e^-$). Since our electron samples are very pure, the contribution from (i) is relatively small. Previous non-photonic electron analysis [Ada05c, Abe07, JC09, Abe08a] found that in STAR experiment with

inner trackers, the photonic electrons are dominant over the non-photonic electrons. It means in the case of our high p_T J/ψ reconstruction, the backgrounds from (iii) and (iv) are dominant over (ii). If both the electron candidates are from the same γ or $\gamma*$, its invariant mass will mostly set at very low mass region ($M_{inv}(ee) < 0.1$ GeV/c^2) and will not contribute to the mass region we are interested in. Therefore, most of our backgrounds are from random combinations of electrons from different γ or $\gamma*$. These backgrounds will spread out in a large invariant mass region and only have a small fraction to set in the mass region we are interested in.

We use the like-sign technique to reproduce the backgrounds from uncorrelated electron pairs. In this technique, every 'EMC+TPC' electrons are paired with every 'TPC only' electrons with the same charge in the same event. Generally, since the number of positive and negative particles may not be the same, to correctly the subset of non-correlated pairs in the unlike-sign ee distribution, the like-sign ee invariant mass distribution is calculated as:

$$N_{Like-Sign}(m) = 2 \times \sqrt{N_{e^+e^+}(m) \times N_{e^-e^-}(m)}, \tag{3.2}$$

where N is the number of entries in a bin with its center at the ee pair invariant mass m. But in our low background and low statistics case, the $N_{e^+e^+}$ and $N_{e^-e^-}$ has large possibility to be 0 in a given bin. The multiply of them is likely to underestimate the background. On the other hand, since the electrons are usually produced in pair, the number of positive charged electron candidates should be similar with the number of negative charged electron candidates. The sum of the $N_{e^+e^+}$ and $N_{e^-e^-}$ ($N_{e^+e^+} + N_{e^-e^-}$) is better than $2 \times \sqrt{N_{e^+e^+} \times N_{e^-e^-}}$ in our case. The dashed line on the left panel of Fig. 3.9 shows the background reproduced by this method. It matches the unlike-sign ee invariant mass distribution at $M_{inv}(ee) > 3.2$ GeV/c^2. The excess on the left-hand side of the J/ψ peak for unlike-sign pairs is due to the bremsstrahlung of the electrons decayed from J/ψ which will be discussed in detail in Sec. 3.6. To include enough J/ψ signals, the mass window we use to count J/ψ signals is set to be $2.7 < M_{inv}(ee) < 3.2$

GeV/c^2. The number of J/ψ signals and the signal to background ratio are listed in Tab. 3.4. The right panel of Fig. 3.9 shows the raw p_T distribution of unlike-sign and like-sign electron pairs within the mass window. In the p_T range $5 < p_T < 8$ GeV/c, we are background free. We divide the p_T range into two p_T bins: 5-6 GeV/c and 6-8 GeV/c.

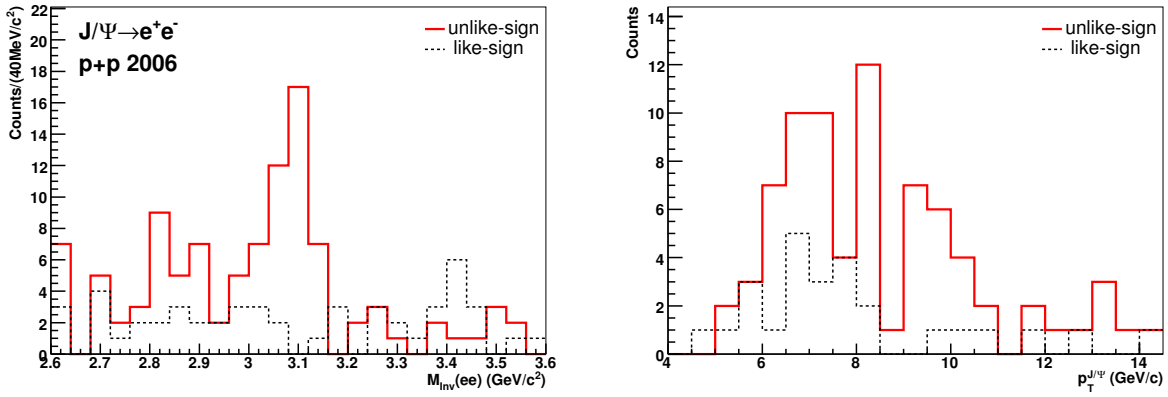

Figure 3.10: **Left:** Invariant mass distribution of unlike-sign (solid line) and like-sign (dashed line) electron pairs from 2006 $p+p$ data.
Right: Raw p_T distribution of unlike-sign (solid line) and like-sign (dashed line) electron pairs with $2.7 < M_{inv}(ee) < 3.2$ GeV/c^2

The STAR BEMC only has half coverage in RHIC 2005 run but has full coverage in RHIC 2006 run. And the high tower trigger threshold in 2006 is much higher than that in 2005, allowing the high tower trigger record more luminosity. The sample luminosity in 2005 and 2006 $p+p$ is 2.8 pb^{-1} and 11.3 pb^{-1}, respectively. Figure 3.10 shows the invariant mass distributions and the raw p_T distribution of unlike-sign and like-sign electron pairs in 2006 $p+p$ collisions. Due to the doubled coverage and much higher recorded luminosity, the p_T coverage of our J/ψ is pushed up to 14 GeV/c. We divide the p_T coverage into 4 bins: 5-7, 7-9, 9-11 and 11-14 GeV/c.

In Cu + Cu collisions, the high tower trigger is easier to be satisfied due to the much higher multiplicity. Thus the rejection factor of this trigger is smaller than that in $p+p$ collisions. To date, RHIC only runs in Cu + Cu configuration in 2005. The STAR high tower trigger recorded 860μb^{-1} (3.4pb^{-1} pp-equivalent) luminosity with threshold $E_T > 3.75$ GeV. The high multiplicity also result in worse dE/dx resolution in Cu + Cu

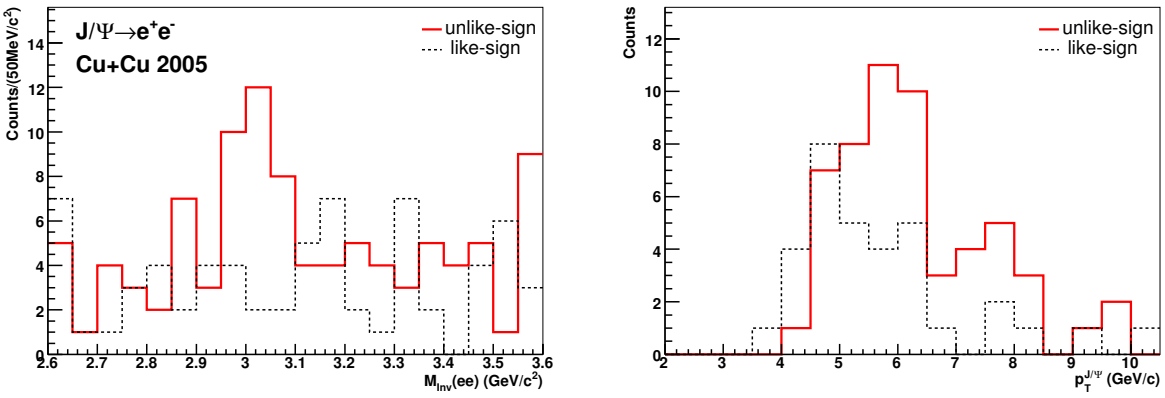

Figure 3.11: **Left:** Invariant mass distribution of unlike-sign (solid line) and like-sign (dashed line) electron pairs from 2005 Cu + Cu data.
Right: The raw p_T distribution of unlike-sign (solid line) and like-sign (dashed line) electron pairs with $2.7 < M_{inv}(ee) < 3.2$ GeV/c^2

collisions than that in $p+p$ collisions. Even more, in a Cu + Cu event the BEMC triggered electron ('EMC+TPC' electron) has to be paired with much more 'TPC only' electrons in the same event than in a $p+p$ event, most of them are combinatorial background, thus the signal to background ratio is much worse than that in $p+p$ collisions. To suppress this effect, we increase the p_T cut for the 'TPC only' electron from 1.2 GeV/c to 1.5 GeV/c. Figure 3.11 shows the invariant mass distributions and the raw p_T distribution of unlike-sign and like-sign electron pairs in Cu + Cu collisions collected in 2005. Even though the significance of the signal is not so good as that in $p+p$ collisions, the signal is still obvious before any background subtraction. And as showing in the right panel of Fig. 3.11, our signal mostly situate p_T range $p_T > 5$ GeV/c. For convenience of getting nuclear modification factor R_{AA}, we use the same binning as that in 2005 $p+p$ data.

In RHIC 2004 Au + Au run, the STAR BEMC had very limited coverage and did not collect much data for this analysis. In RHIC 2007 Au + Au run, the STAR BEMC had full coverage and sampled $\sim 500\ \mu b^{-1}$ ($\sim 20\ pb^{-1}$ pp-equivalent) luminosity with $E_T > 5.5$ GeV and $\sim 50\ \mu b^{-1}$ ($\sim 2\ pb^{-1}$ pp-equivalent) luminosity with $E_T > 4.3$ GeV. These data are suitable for this analysis but not fully produced yet.

3.4 Acceptance and Efficiency

The raw yields of J/ψ need to be corrected for the detector acceptance, reconstruction and selection efficiency etc. In this analysis, the J/ψ detection efficiency was calculated through two complementary methods. In the first method, the $'$EMC+TPC$'$ electron detection efficiency and $'$TPC only$'$ electron detection efficiency are determined separately. The J/ψ detection efficiency is then determined by folding the efficiencies of the decay electrons using the J/ψ decays kinematic. This method will be discussed in detail in Sec.3.4.1, Sec. 3.4.2 and Sec. 3.4.3. In the second method, we directly embed J/ψ's into PYTHIA events and run them through the detector response and reconstruction procedures. This method will be discussed in detail in Sec. 3.4.4.

3.4.1 $'$EMC+TPC$'$ electron detection efficiency

The $'$EMC+TPC$'$ electron detection efficiency, including the BEMC trigger efficiency, tracking efficiency, acceptance etc., is determined by comparing the triggered electron yields to the inclusive electron spectrum from previous measurements [Abe07]. The electron raw yields are obtained by fitting the $n\sigma_e$ distribution to a multi-Gaussian function. Figure 3.12 shows a typical $n\sigma_e$ distributions in high tower triggered $p+p$ data at 200 GeV. The black curves represent the fit to 8-Gaussian function. Each Gaussian function represents the $n\sigma_e$ distribution of one particle. All of the Gaussian functions have the same width. The mean value of the Gaussian functions for electron are not at 0 due to imperfect TPC calibration. We treat this value as free parameter and fix the difference of the mean value of the Gaussian distributions for other particles relative to that of electron. The fixed values are obtained from the TPC re-calibration discussed in detail in Ref. [Xu08]. Since the electron yields are dominant in the high tower trigger data, the systematic uncertainty on the electron raw yields is much less than the statistical uncertainty.

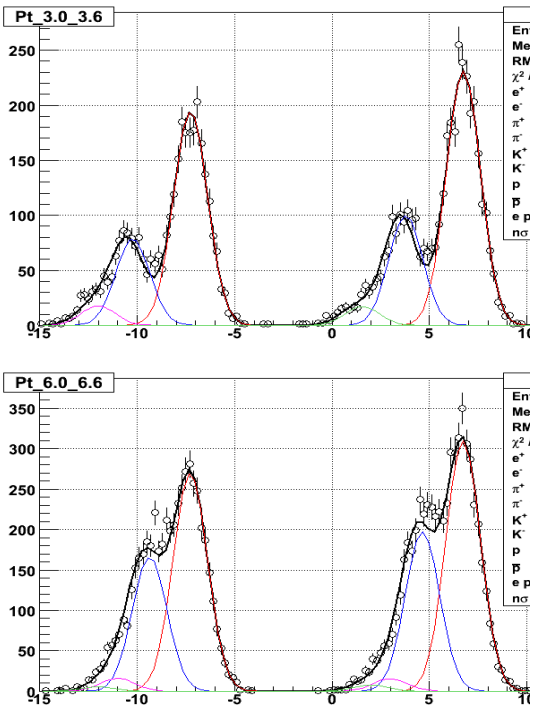

Figure 3.12: $n\sigma_e$ distribution in high tower triggered $p+p$ collisions at $3.0 < p_T < 3.6$ GeV/c (upper panel) and $6.0 < p_T < 6.6$ GeV/c (lower panel), and shifted by ± 7 for positively and negatively charged particles, respectively. The black curve represents the fit to 8-Gaussian distribution. The Gaussian functions peaked at $\sim \pm 7$ are for electrons.

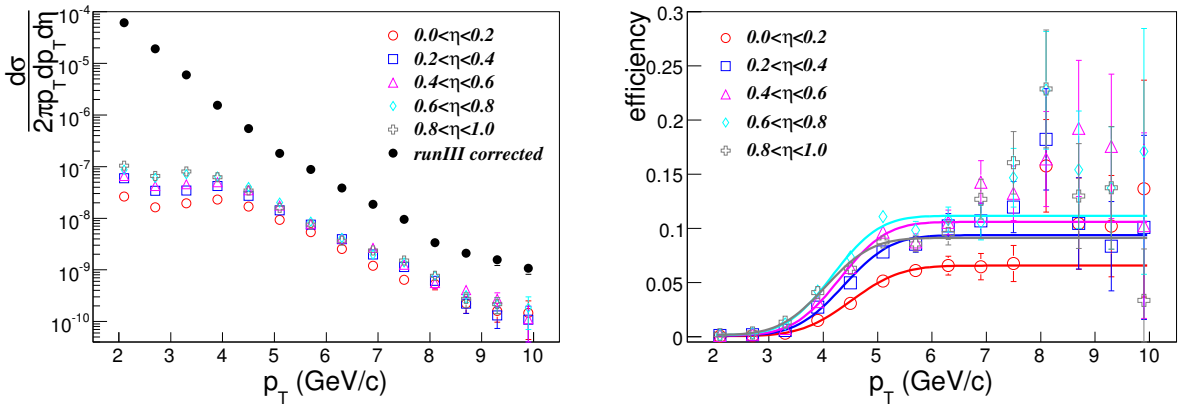

Figure 3.13: **Left:** The 'EMC+TPC' electron raw p_T spectra in 2005 $p+p$ collisions (open symbols) and the efficiency fully corrected electron p_T spectrum in 2003 $p+p$ collisions [Abe07]
Right: The 'EMC+TPC' electron detection efficiency as a function of p_T in different η bins in 2005 $p+p$ collisions.

The inclusive electron raw differential cross section:

$$\frac{d\sigma}{2\pi p_T dp_T d\eta} = \frac{dN}{\mathcal{L}^{-1} 2\pi p_T dp_T d\eta}, \tag{3.3}$$

where $\mathcal{L}$ is the sample luminosity, in 2005 $p+p$ data is obtained in several small η bins ($\Delta\eta = 0.2$) showing in Fig. 3.13 (left) as open symbols. The efficiency fully corrected p_T spectrum from previous measurement [Abe07] is also shown as solid circles in Fig. 3.13 (left) for comparison. The electron detection efficiency, including trigger efficiency, tracking efficiency, acceptance etc., as a function of p_T in each η bin in 2005 $p+p$ collisions is obtained by dividing the open symbols by the solid circles in 3.13 (left), and is shown in the right panel of 3.13. The curves represent the fits by the Error Function:

$$erf(x) = \frac{2}{\sqrt{\pi}} \int_x^\infty e^{-t^2} dt. \tag{3.4}$$

At high p_T ($p_T > 7$ GeV/c, the data points have large fluctuation and uncertainty mostly due to limited statistics, less powerful of the BEMC and BSMD hadron rejection and smaller separation of the electron/hadron dE/dx. But at low p_T ($p_T < 7$ GeV/c), the curves describe the data points very well. The efficiency increase as increasing $|\eta|$ at ($|\eta| < 0.8$) is mostly due to the high tower trigger bias. The threshold of each tower is set according to:

$$E = E_T / \sin\theta, \tag{3.5}$$

where θ is the dip angle with respect to the TPC center. The center ring has the lowest E threshold and the most outer ring has the highest E threshold. In an event with the z component of the primary vertex deviates from 0 ($V_z \neq 0$), the tracks with $\eta \sim 0$ are more difficult to satisfy the high tower trigger than those tracks pointing to the center rings, especially in 2005 runs when the STAR BEMC had only coverage on the west side ($\eta > 0$). The drop of the efficiency at the highest η bin is due to the BEMC acceptance. In 2006 run, the high tower threshold is much higher (5.4 GeV). The efficiency curve is mostly constrained by the data points at very high p_T. But in previous

measurement [Abe07], the statistics at high p_T is very poor due to limited sample luminosity. However, the statistics at high p_T in 2005 $p+p$ collisions is much better. So we get the 'EMC+TPC' detection efficiency by taking the ratio of the raw p_T spectra from 2005 data and 2006 data shown in Fig. 3.14.

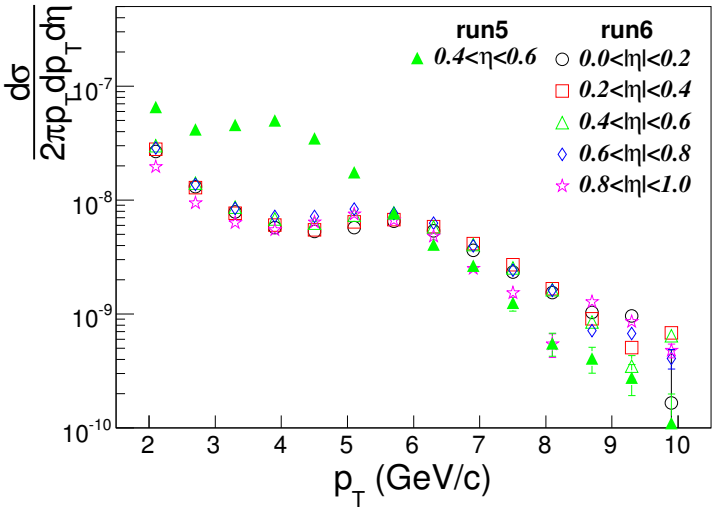

Figure 3.14: The 'EMC+TPC' electron raw p_T spectra in 2006 $p+p$ collisions (open symbols) and in 2005 $p+p$ collisions (solid triangles).

In 2005 Cu + Cu collisions, the STAR detector configuration is quite similar to that in 2005 $p+p$ collisions. Since the multiplicity in Cu + Cu collisions is not high enough to affect the STAR TPC. For the Cu + Cu data, we use the same efficiency as the 2005 $p+p$ data. In this method, efficiencies of all the cuts are automatically taken into account. And the uncertainty on the sample luminosity used to normalize the spectra will cancel when we calculate the J/ψ spectra.

3.4.2 'TPC only' electron detection efficiency

The efficiency of the 'TPC only' electron depends only on the TPC tracking efficiency and dE/dx efficiency. The TPC tracking efficiency is studied by Monte-Carlo simulations. The simulated electrons are generated using a flat p_T and a flat rapidity y distribution and pass through GSTAR [Lon] (the framework software package to run the STAR detector simulation using GEANT [Ago03, All06] and TRS (the TPC Response

Simulator [Lon]). The simulated electrons are then combined with a real raw event and we call this combined event a simulated event. This simulated event is then processed through the standard STAR reconstruction chain and we call this event after reconstruction a reconstructed event. The reconstructed information of those particles in the reconstructed event is subsequently associated with the Mente-Carlo information in the simulated event. At the end, we get the total number of simulated electrons from simulated events in a certain p_T bin. Meanwhile, we can get the total number of associated tracks after all of the track quality cuts we applied except those associated with a track's dE/dx in the reconstructed events in this p_T bin. In the end, the ratio of the number of associated electrons over the number of simulated electrons is the TPC reconstruction efficiency for a certain p_T bin. The TPC tracking efficiency increases as increase p_T at low p_T and reach a plateau at $p_T \sim 1$ GeV/c. We use a constant efficiency value 87% for the $'$TPC only$'$ electrons. The inefficiency associated with dE/dx quantities are currently not well simulated in STAR [Gon]. Instead, we rely on the real data itself in order to account for the inefficiency caused by cuts on dE/dx hit points ($nHitsDedx$) and dE/dx particle identification ($n\sigma_e$) for each track. To study the inefficiency of the $nHitsDedx$, we select a track sample by applying all of the track quality cuts in the real data except the cuts associated with the dE/dx, and obtain the inefficiency of the $nHitsDedx$ cut by comparing the number of tracks with and without the $nHitsDedx$ cut. Figure 3.15 shows the efficiency of $nHitsDedx$ cut as a function of p_T. At $p_T > 1.2$ GeV/c, it is almost a constant at the value of 98%.

An ideal $n\sigma_e$ distribution for electrons is a normal Gaussian distribution, a $|n\sigma_e| < 2$ cut will result in a 95% efficiency. But in real data, the calibration is not perfect, the $n\sigma_e$ distribution is usually shift a little bit and the σ also deviates from 1. Figure 3.16 shows the mean and σ of $n\sigma_e$ for electrons as a function p_T in 2006 $p+p$ data. Both of the mean and width are almost a constant with p_T. The mean is shifted to -0.24 and the σ is 0.87. The $|n\sigma_e| < 2$ is a very loose cut, the shift of the $\langle n\sigma_e \rangle$ will not result in much change on the efficiency. The solid line in Fig. 3.17 shows the efficiency of the $|n\sigma_e| < 2$ as a function of $\langle n\sigma_e \rangle$, the shift of -0.24 only result in a 1% decrease on the efficiency.

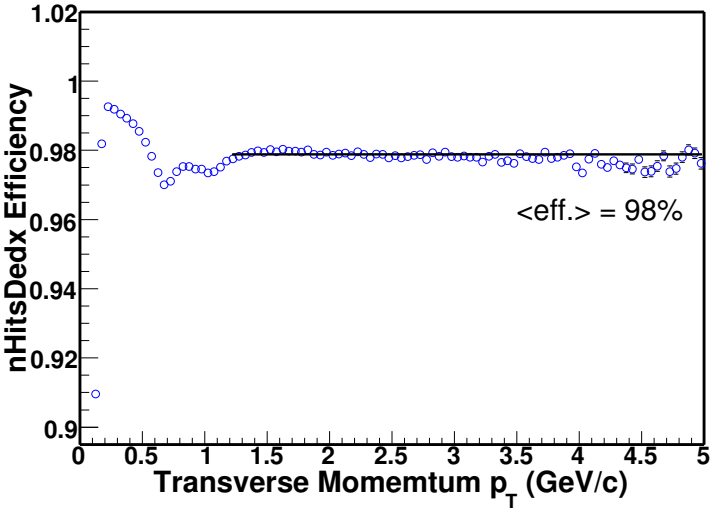

Figure 3.15: The efficiency due to the $nHitsDedx$ cut as a function of p_T.

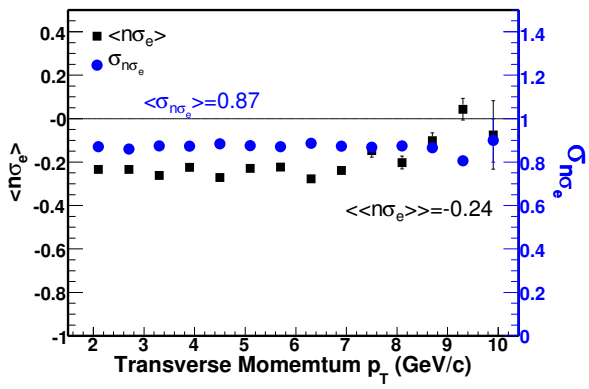

Figure 3.16: The mean (squares) and σ (circles) of $n\sigma_e$ as a function of p_T in 2006 $p+p$ collisions. The circles are corresponding to the axis on the left side and the squares are corresponding to the axis on the right side.

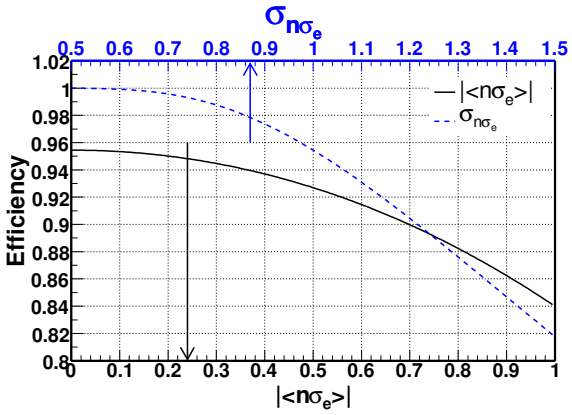

Figure 3.17: The efficiency of $|n\sigma_e| < 2$ cut as a function of $|\langle n\sigma_e \rangle|$ (solid line) and $\sigma_{n\sigma_e}$ (dashed line). The solid line is corresponding to the axis on the bottom and the dashed line is corresponding to the axis on the top. The arrows represent the $|\langle |n\sigma_e| \rangle$ (solid line) and $\sigma_{n\sigma_e}$ in 2006 $p+p$ data.

The dashed line on Fig. 3.17 shows the efficiency of the cut $|n\sigma_e| < 2$ as a function of $\sigma_{n\sigma_e}$, due to the narrower width, our 2 σ dE/dx cut efficiency increase from 95% to 98%.

3.4.3 J/ψ detection efficiency

After getting the detection efficiencies for the decay electrons, the J/ψ detection efficiency is then determined by folding the efficiencies of the decay electrons using the J/ψ decays kinematic. We generate a J/ψ sample with a flat p_T and a flat ϕ distribution first. For the rapidity y distribution, we take the distribution predicted by NRQCD, which matches PHENIX measurements in $p+p$ collisions at 200 GeV [Ada07a]. The kinematics of the J/ψ decay into e^+e^- is provided by the PYTHIA framework software package [SMS06]. The electron daughter with higher p_T is treated as triggered electron and applied the $'$EMC+TPC$'$ electron efficiency in the corresponding p_T and η. For the other electron, the acceptance, tracking efficiency and efficiency associated with dE/dx are applied. Then the J/ψ efficiency in a given p_T bin is obtained by convoluting the detecting probabilities of the daughters through this exercise. Figure 3.18 shows the J/ψ detection efficiency as a function of p_T in 2005 and 2006 $p+p$ collisions.

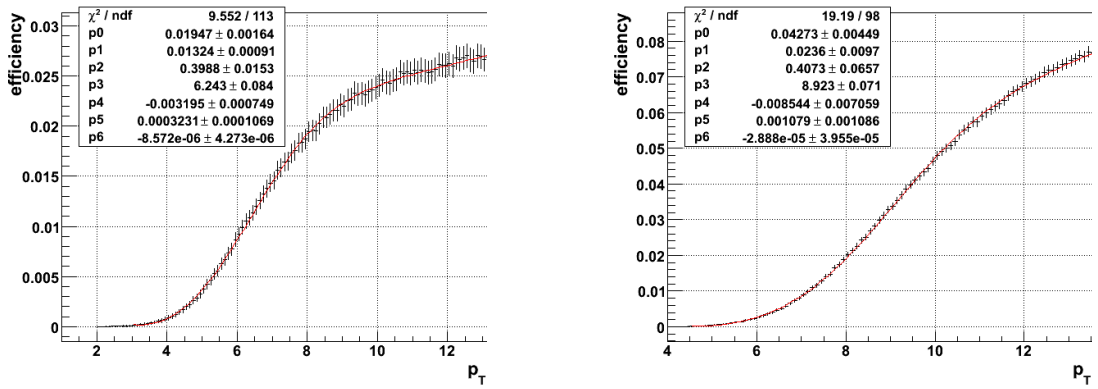

Figure 3.18: J/ψ detection efficiency as a function of p_T in 2005 and 2006 $p+p$ collisions. The curves represent the parameterizations.

3.4.4 J/ψ detection efficiency check with embedding

We also did an independent check on the J/ψ detection efficiency through the STAR standard embedding procedure for 2006 $p+p$ data. In this procedure, the simulated J/ψ are generated using a flat p_T and a flat rapidity y and embedded into a PYTHIA event. This embedded event are then passed through the GSTAR to simulate the detector responses. The electromagnetic shower are also simulated. Then the detector responses are combined into a real raw background event (zero bias event). The STAR TPC response is well described in the embedding as shown in Ref. [Abe08b]. But the STAR BEMC is implemented recently and has to check the validity. The STAR BEMC sits outside the STAR TPC and CTB/TOF. To check the BEMC simulation and reconstruction in embedding, we compared the tower energy of electrons in the reconstructed event to the simulated momentum at the TPC exit point. Figure 3.19 shows the ratio of the tower energy of electron to the simulated momentum at the last TPC point. We fit the distribution to a Gaussian distribution and find the mean value to be 1.002 ± 0.002. The tower energy in the embedding are well simulated and reconstructed. The effect of an online high tower trigger is implement by a trigger simulator. After applying all of the cuts as done in the real-data analysis, the J/ψ efficiency is directly obtained from the embedding data. Figure 3.20 shows the J/ψ detection efficiency as a function of p_T from embedding. The red curve is the efficiency we got from previous sections (the first method). We scale down the red curve to fit the data points and get the black curve. The scale factor is 0.9, which means the difference of the efficiency from these two methods is only 10%.

3.4.5 Polarization effect on the J/ψ detection efficiency

The J/ψ polarization parameter α is measured to be negative at high p_T region ($p_T > 5$ GeV/c) and become increasingly negative (favoring longitudinal polarization) as p_T increase at Tevetron [Abu07]. Our detector acceptance for the J/ψ may be different depending of the polarization.

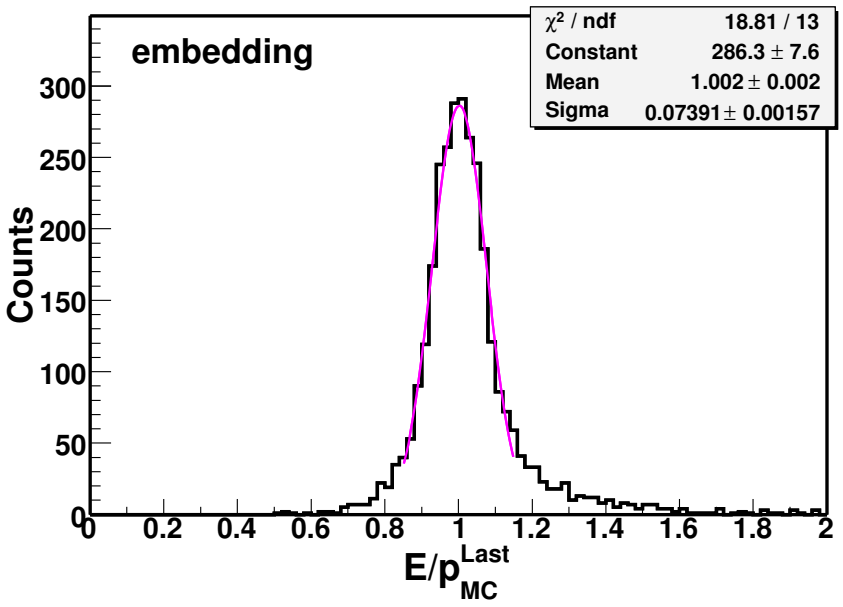

Figure 3.19: The ratio of tower energy to the simulated momentum at the last TPC point for electron in embedding. The curve represent the fit to a Gaussian function.

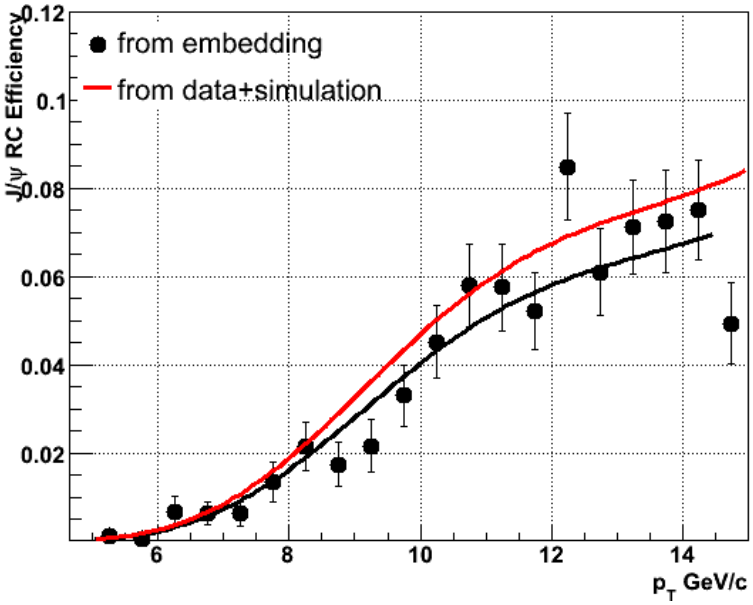

Figure 3.20: J/ψ detection efficiency from embedding. The red curve shows the efficiency from the first method discussed in text. The black curve is from scaling down the red curve to match the data points.

To evaluate the effect of J/ψ polarization on our J/ψ detection efficiency, we use the polarization parameter α as a function of p_T from CDF measurements [Abu07]. Then re-sample the electron angular distribution in our simulation to the following distribution:

$$dN/d\cos\theta^{\star} \propto 1 + \alpha\cos^2\theta^{\star}, \tag{3.6}$$

where the $\theta^{\star}$ is the angle between the directions of electron in the rest frame of J/ψ and J/ψ. The detection efficiency from polarized J/ψ is compare to that with no J/ψ polarization. The left panel of Fig. 3.21 shows the J/ψ detection efficiency with and without polarization. The ratio is shown on the right panel. The polarization has almost no effect at $p_T \sim 5$ GeV/c and increase the J/ψ detection efficiency as increasing p_T. We conclude that the effect is $< 2\%$ at $p_T < 15$ GeV/c.

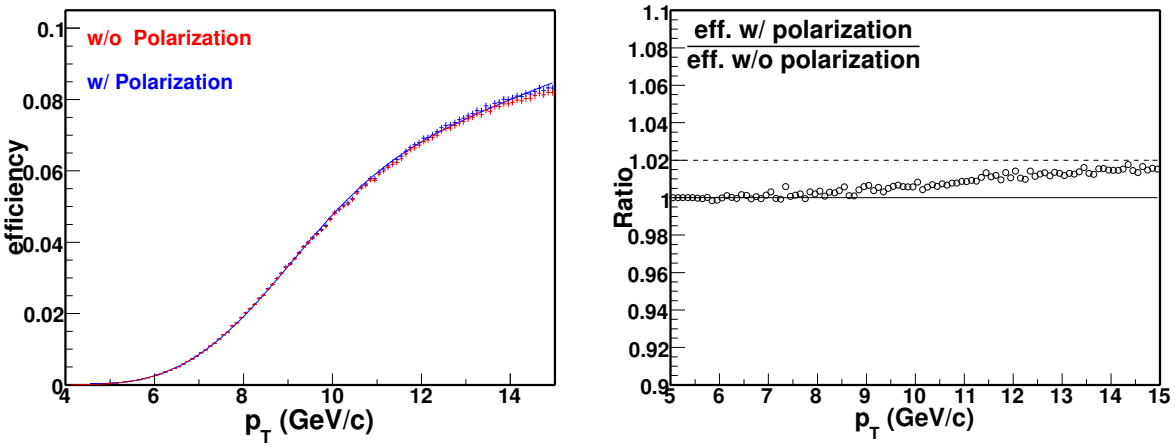

Figure 3.21: **Left:** J/ψ detection efficiency with (blue) and without (red) polarization as a function of p_T in 2006 $p+p$ collisions.
Right: The ratio of J/ψ detection efficiency with and without polarization.

3.5 Application of Efficiency via Log-likelihood Method

After determining losses due to finite acceptance and inefficiencies of the STAR detectors, the raw spectra are typically corrected by scrutinizing the background subtracted invariant mass distribution in a certain p_T window [Abe08b], extracting the number of candidates, and correcting these by the corresponding efficiency in that p_T

window. But in this analysis, the available statistics do not allow us to get the raw spectra in small p_T windows. Even more, the J/ψ detection efficiency significantly increase as increasing p_T. These facts do not allow for corrections to the raw spectra via the application of the aforementioned method. Instead, corrections in wide p_T windows in this analysis are carried out via a log-likelihood method.

We have to assume a function to describe the J/ψ p_T spectrum first:

$$B \times \frac{d\sigma}{2\pi p_T dp_T dy} = f(p_T), \tag{3.7}$$

where B is the $J/\psi \to e^+e^-$ branching ratio and $f(p_T)$ is the function to describe the J/ψ p_T spectrum. It can also be written as:

$$B \times \frac{d\sigma}{2\pi p_T dp_T dy} = f(\langle p_T \rangle) \times \left(\frac{f(p_T)}{f(\langle p_T \rangle)} \right), \; r(p_T, \langle p_T \rangle) \equiv \left(\frac{f(p_T)}{f(\langle p_T \rangle)} \right), \tag{3.8}$$

where $\langle p_T \rangle$ is the p_T position where we want to put the data points, and $f(\langle p_T \rangle)$ is the differential cross at $\langle p_T \rangle$, which is what we want. In $r(p_T, \langle p_T \rangle)$, the normalization factor in the spectrum function has been cancelled out thus only dependent on the spectrum shape. After integrating over the total luminosity and rapidity coverage, the dN/dp_T is derived:

$$\frac{dN}{dp_T} = f(\langle p_T \rangle) \times r(p_T) \times (2\pi p_T \Delta y) \times \mathcal{L} \equiv g(p_T), \tag{3.9}$$

where $\mathcal{L}$ is the sample luminosity. Then the average of expected raw J/ψ counts in a given p_T bin ($p_T - \Delta p_T/2$ to $p_T + \Delta p_T/2$) is:

$$\lambda = \int_{p_T - \Delta p_T/2}^{p_T + \Delta p_T/2} g(p_T) \times \epsilon(p_T) dp_T, \tag{3.10}$$

where $\epsilon(p_T)$ is the J/ψ detection efficiency as a function of p_T. In this p_T bin, the possibility to observe n J/ψ counts follows the Poisson distribution:

$$\mathcal{P}(n, \lambda) = \frac{\lambda^n e^{-\lambda}}{n!}, \tag{3.11}$$

The Log-likelihood of the raw p_T spectrum in a wide p_T window with several smaller p_T bins are:

$$L = -\ln(\Pi\mathcal{P}(n_i, \lambda_i)) = \sum -\ln(\mathcal{P}(n_i, \lambda_i)), \tag{3.12}$$

where n_i and λ_i is the observed and expected J/ψ raw counts in i-th p_T bin, respectively. The possibility density function (PDF) can be defined as :

$$PDF = A \times e^{-L+L_{min}}, \tag{3.13}$$

where L_{min} is the minimum of L and A is a normalization constant. Figure 3.22 shows a typical log-likelihood and possibility density function (PDF) of J/ψ cross section in a given p_T window. The solid vertical line on the right panel represents the most likely cross section, while the dashed vertical lines represent the 1-σ deviations.

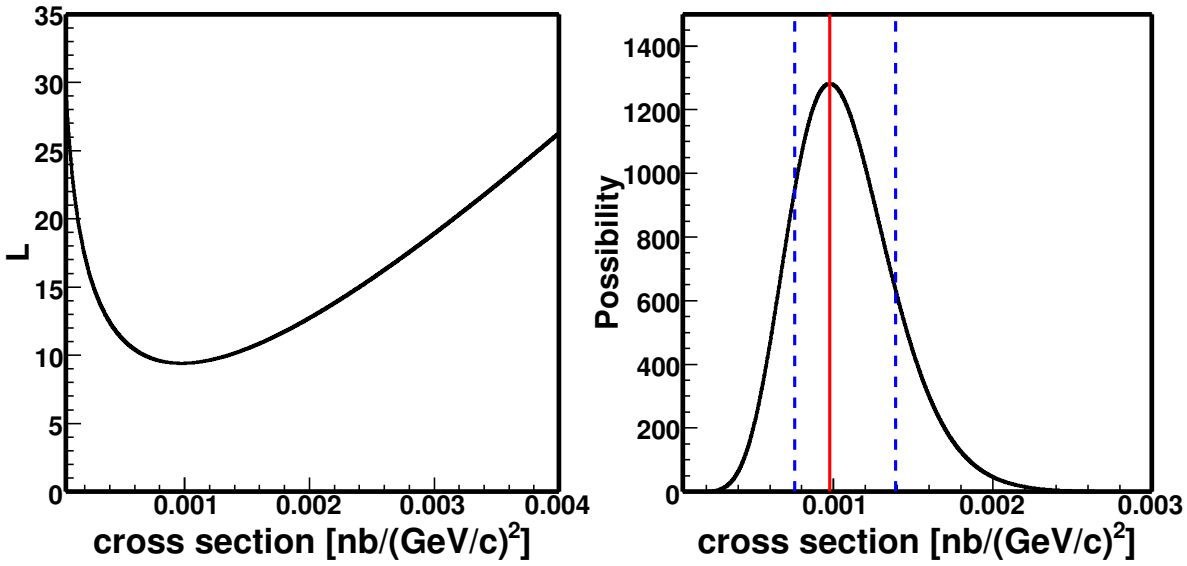

Figure 3.22: Log-likelihood (left) and possibility density function (right) of J/ψ differential function in a certain p_T window. The solid vertical on right panel shows the most likely cross section and the dashed vertical lines represent the 1-σ deviations.

3.6 J/ψ Invariant Mass Distribution Simulation

In our analysis, we have to integral the invariant mass distribution over a finite range ($2.7 < M_{inv} < 3.2$ GeV/c^2) to count signals. But the electron bremsstrahlung (mostly happens in the inner trackers such as SVT and SSD) can result in a long tail on the left side of the J/ψ peak. A finite mass window can not count all of the J/ψ signals thus a efficiency has to be obtained to correct the J/ψ cross section. This efficiency relies on how well one can reproduce the shape of the long tail.

In principle, one can directly get the invariant mass distribution from the embedding data, in which all of the detector response are simulated. But Fig. 3.23 shows that the mass cut efficiency as a function of reconstructed p_T is quit different with that as a function of input p_T (MC p_T). This is mostly caused by the input flat p_T distribution which is far away from the real p_T distribution which dramatically decrease with increasing p_T. In a J/ψ sample with flat MC p_T distribution, at a certain reconstructed p_T, there is more J/ψ with higher MC p_T but lost energy thus has this smaller reconstructed p_T, than that in a J/ψ sample with real p_T distribution. It is usually solved by either re-sampling or re-weighting the flat p_T distribution into a distribution with reasonable shape. But the re-sampling method will reject lots of statistics and re-weighting method gives funny statistical errors on the efficiency. We made a toy model to simulate the J/ψ invariant mass distribution by using the information from embedding with flat J/ψ p_T distribution and limited statistics. It follows these basic steps:

1. *Parameterize the energy loss for electrons.*

   In STAR, the energy loss of a electron is mostly happened before the TPC (in the beam pipe, the SVT, the SSD and the inner filed cage of the TPC). Figure 3.24 shows the ratio of the simulated momentum at the first TPC measured point (p_{MC}^{first}) to the momentum generated at the primary vertex (p_{MC}) for electrons with different p from the embedding data. The peak around 1 is mostly due to the ionization energy loss. The long tail is mostly from the bremsstrahlung. This

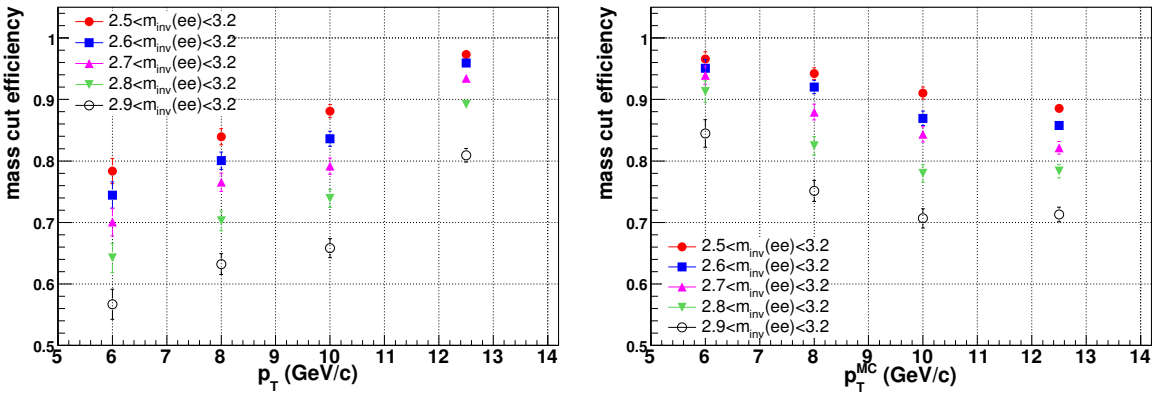

Figure 3.23: J/ψ mass cut efficiency as a function of MC p_T (left panel) and reconstructed p_T (right panel) for different mass windows.

distribution is almost independent with the electron p.

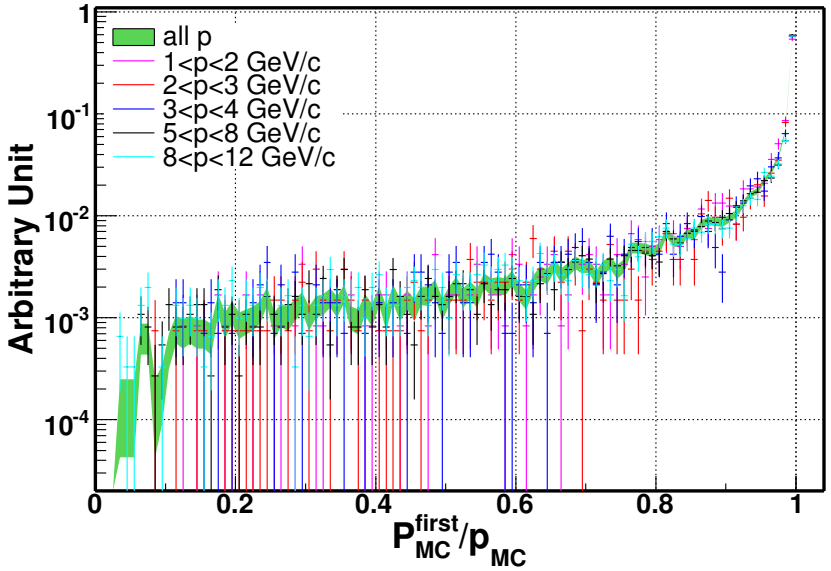

Figure 3.24: The energy loss of electrons in different p ranges from embedding data.

2. *Parameterize the momentum resolution for electrons.*

   The momentum of tracks reconstructed by the TPC is smeared by the spatial resolution of the TPC readouts. Figure 3.25 shows the distribution of $p_{MC}^{first}/p - 1$ for electrons in different p_T ranges. They are described by the Gaussian distributions very well. The mean values of the Gaussian distributions are almost 0, while the resolutions are proportional to the momentum as shown in Fig. 3.26.

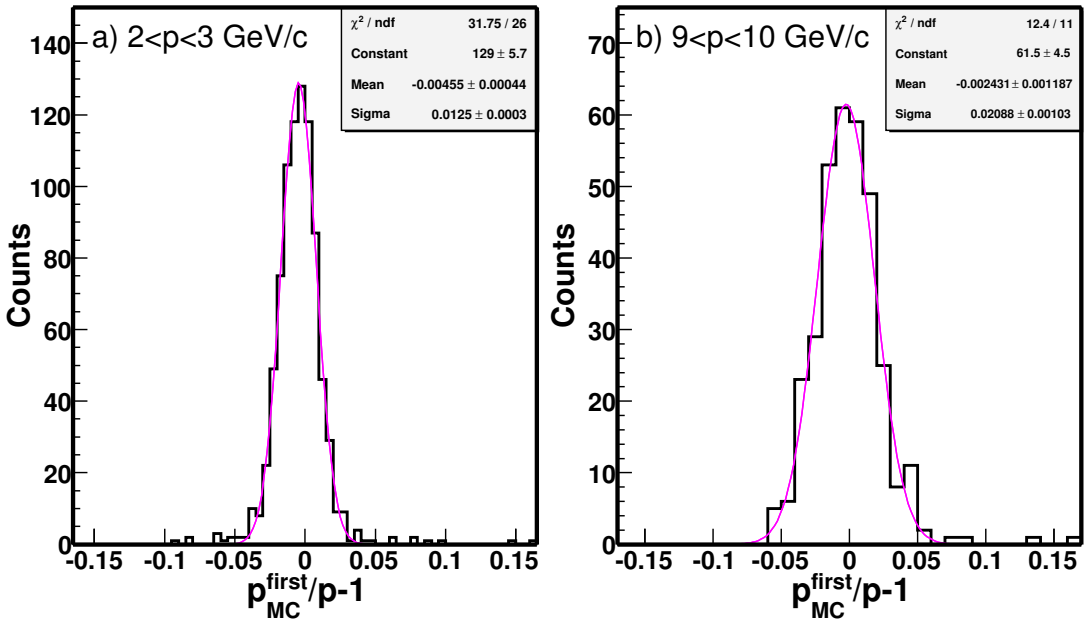

Figure 3.25: The momentum smearing for electrons from embedding data.

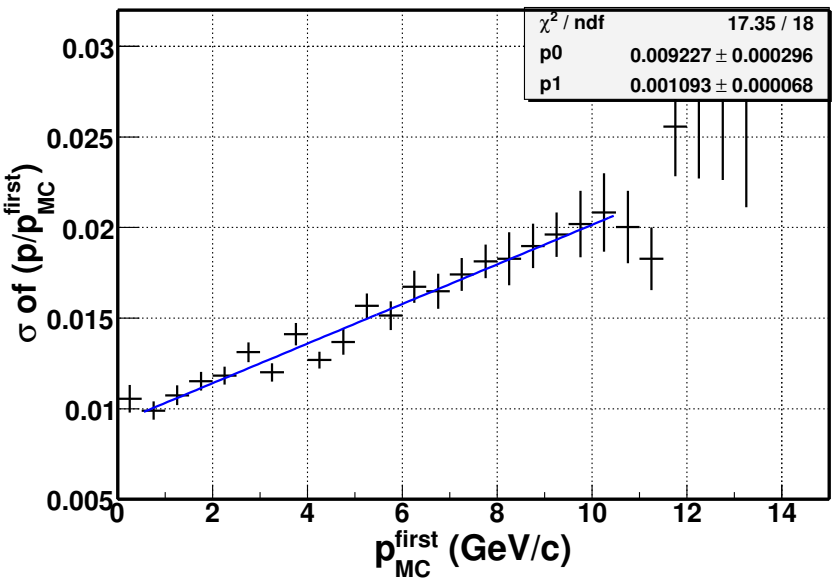

Figure 3.26: The momentum resolution for electrons as a function of momentum. The blue line represent a straight line fit.

3. *Generate J/ψ sample and decay into electrons.*

   A J/ψ sample is generated with flat ϕ, Gaussian rapidity distributions at mid-rapidity. The p_T distribution is from a fit to all of the available J/ψ p_T spectra at mid-rapidity in $p+p$ collisions at 200 GeV at RHIC. The J/ψs then decay into electrons.

4. *Implement the energy loss and momentum resolution to the electrons.*

   For a given electron generated in step 3, we sample the energy loss from step 1 to get the momentum at the first TPC measured point (p_{MC}^{first}). Then get the momentum resolution according its momentum and get the smeared momentum (p) from the p_{MC}^{first} by sampling the $p_{MC}^{first}/p - 1$ distribution (the Gaussian distributions discussed in step 2).

5. *Simulate the BEMC trigger.*

   The BEMC trigger behavior is simulated by simply sampling the p_T distribution of the electron daughter with higher p_T according the $'$EMC+TPC$'$ electron detection efficiency.

6. *Calculate the invariant mass of the electrons using the folded momentum.*

The solid curve in Fig. 3.27 shows the invariant mass distribution from simulation. It is fitted to the data in the mass range 2.7-3.3 GeV/c^2. The χ^2/ndf in this range is 16/14. The toy model well reproduced the invariant mass distribution. The efficiency of the mass cut 2.7-3.2 GeV/c^2 is obtained to be 90%.

3.7 Systematic Uncertainty Study

The systematic uncertainties contribute to the final cross section were studied. The main sources are from signal extraction, efficiency determination and application.

To study the contributions from signal extraction and trigger efficiency, we varied p_T cuts on the $'$EMC+TPC$'$ electron and $'$TPC only$'$ electron, re-calculated and

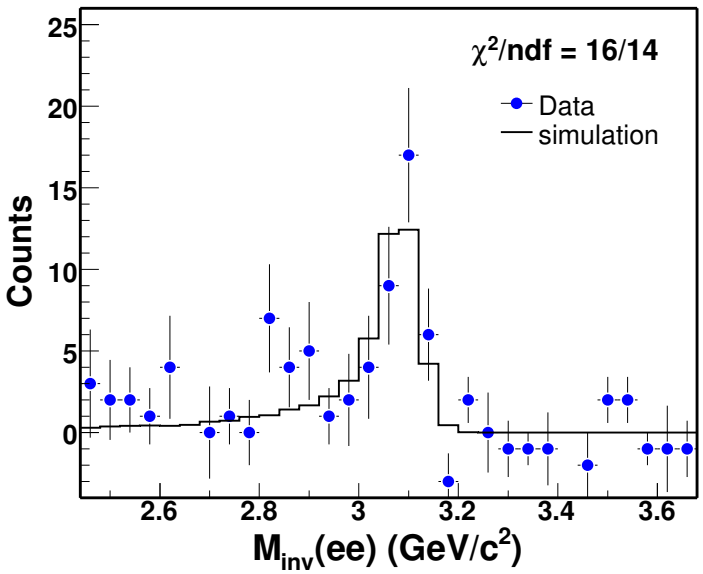

Figure 3.27: J/ψ invariant mass distribution from simulation is fit to the data in the mass range 2.7-3.3 GeV/c^2.

re-applied the J/ψ detection efficiency to get the differential cross sections to evaluated the systematic uncertainty.

On the efficiency determination, 5% systematic uncertainty are included due to the uncertainty on the materials in the STAR simulation software package. The difference of our two methods to determining the J/ψ detection efficiency are also include into the systematic uncertainty.

In the application of the J/ψ detection efficiency, that is the log-likelihood method, we have to assume a p_T spectrum shape, this could introduce extra systematic uncertainty. We tried to use different p_T spectrum function to evaluate this systematic uncertainty.

Table 3.5: Systematic uncertainties to the final p_T spectrum.

Source	Relative contribution
kinematic cuts	9%
efficiency	5%
mass cut efficiency	5%
log-likelihood method	3%
Sum	12%

Table 3.5 summarizes the systematic uncertainties from different sources.

There is also 14% normalization uncertainty on the cross section for inclusive non-single diffractive $p + p$ events [Ada03].

CHAPTER 4

Azimuthal Correlations between High-p_T J/ψ and Charged Hadrons

The high signal to background (S/B) ratio of the high p_T J/ψ in $p+p$ collisions allows us to measure the azimuthal correlations between high p_T J/ψ and charged hadrons to investigate the high p_T J/ψ production mechanism, especially the fraction of the high p_T J/ψ from B-meson feeddown. This chapter is dedicated to a detailed description of constructing the azimuthal correlations between high p_T J/ψ and charged hadrons in data. The correlations between J/ψ from different sources and charged hadrons are also obtained from PYTHIA [SMS06] to decompose the correlations observed from data.

4.1 Construction of the correlation function

The high p_T J/ψ are reconstructed through the dielectron channel using the high tower triggered data as discussed in Chapter 3. We select the electron pairs with invariant mass within 2.9-3.2 GeV/c^2 as our J/ψ candidates. Note that this mass window is different from that for the J/ψ transverse momentum distributions discussed in Chapter 3. In the spectrum analysis, we use a wider mass window (2.7-3.2 GeV/c^2) to count signal with higher efficiency and reduce the systematic uncertainty due to efficiency correction from the invariant mass distribution. In this correlation study, the distributions are usually normalized by the number of trigger particle (per J/ψ trigger), thus the absolute yield is not relevant. We narrow the mass window to increase the S/B ratio of the J/ψ candidates. We require J/ψ candidates with $p_T > 5$ GeV/c for

well-defined momentum range. The correlations can be directly compared to other correlations such as hadron-hadron correlations and model calculations or simulations.

Table 4.1: List of the cuts for the high p_T J/ψ for the correlation analysis.

Cut Parameter	Cut value
M_{inv}(ee)	(2.9,3.2) GeV/c^2
p_T	> 5 GeV/c

We use the unidentified charged hadrons as our associated particles to construct the correlation functions. The unidentified charged hadrons are the charged particles detected by the TPC without particle identification. All of the cuts for the associated charge hadrons are list in Tab. 4.2.

Table 4.2: List of the cuts for the associated charged hadrons.

Cut Parameter	Cut value
η	(-1,1)
number of fit points	≥ 15
DCA	< 2.0 cm

We must ensure that the associated particle is not a daughter track of the high p_T J/ψ. This is done by comparing the track identification numbers (track IDs), which are unique for each track in the same event, and rejecting the associated track if its ID matchs with any of the J/ψ daughter track IDs.

The azimuthal correlation function $C(\Delta\phi)$ is then obtained by comparing the ϕ angle of the high p_T J/ψ with that of all of the charged hadron candidates in the same event. Note that the ϕ angle we used here is the track azimuthal angle at primary vertex.

Although our high p_T J/ψ in $p+p$ collisions has high S/B ratio, there are still some backgrounds in the unlike-sign electron pairs ($e^{\pm}e^{\mp}$). The correlations between misidentified high p_T J/ψ and charged hadrons should be different with that between real J/ψ and charged hadrons. Since the like-sign technique reproduces the combinatorial background in the invariant mass distribution very well, we also reproduced the background in the high p_T J/ψ-hadron correlations by getting the correlations between like-sign electron pairs and charged hadrons. Then we subtract this

contributions from the correlations between unlike-sign electron pairs and charged hadrons to obtain the real high p_T J/ψ-hadron correlation function:

$$C_{J/\psi}(\Delta\phi) = (D_{e^{\pm}e^{m}p-h}(\Delta\phi) - D_{e^{\pm}e^{\pm}-h}(\Delta\phi))/(N_{e^{\pm}e^{\mp}} - N_{e^{\pm}e^{\pm}}), \tag{4.1}$$

where $D_{e^{\pm}e^{\mp}-h}(\Delta\phi)$ and $D_{e^{\pm}e^{\pm}}$ are the raw correlation functions for unlike-sign pairs and like-sign pairs, respectively. $N_{e^{\pm}e^{\mp}}$ and $N_{e^{\pm}e^{\pm}}$ are the number of unlike-sign and like-sign electron pairs, respectively.

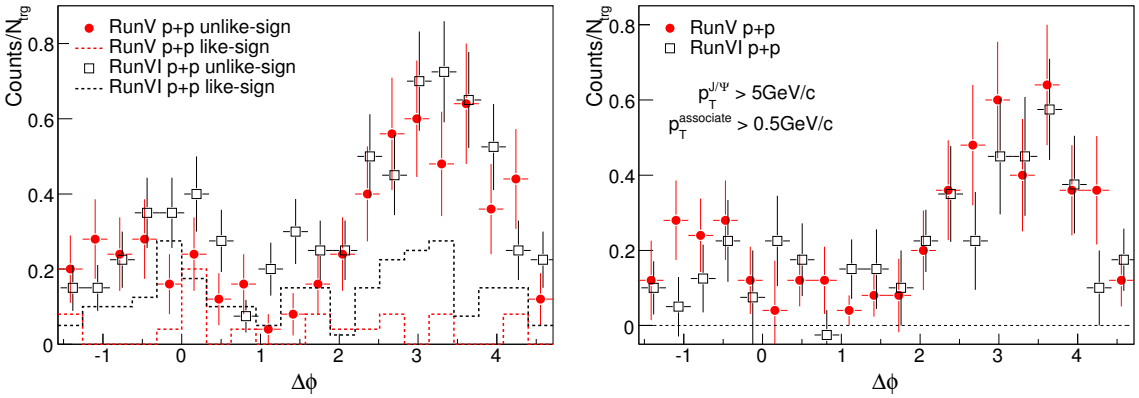

Figure 4.1: **Left:** The azimuthal correlations between high p_T J/ψ and charged hadrons in 2005 (solid circles) and 2006 (open squares) $p+p$ collisions. The dashed lines are the correlations for like-sign electron pairs.
Right: J/ψ-hadron azimuthal correlations after the subtraction of background from J/ψ misidentification.

The left panel of Fig. 4.1 shows the J/ψ-hadron correlations for unlike-sin and like-sign electron pairs in 2005 and 2006 $p+p$ collisions. The correlation functions for both unlike-sign and like-sign pairs are normalized by the same factor: $N_{J/\psi} = N_{unlike-sign} - N_{like-sign}$. The right panel shows the correlations after the subtraction of backgrounds from J/ψ background through the like-sign technique.

4.2 Efficiency and Acceptance Correction

No detector has perfect acceptance and ideal efficiency, and STAR is no exception. Thus the correlation functions have to be corrected with the single track efficiency and

detector acceptance.

4.2.1 Tracking efficiency

As we discussed before, the tracking efficiency is the probability of reconstructing the track and depends on many different effects. Figure 4.2 shows a sample of tracking efficiency as a function of p_T in different η slices for the tracks passing the cuts listed in Tab. 4.2 in $p+p$ collisions. They are obtained from embedding. The efficiency correction for the correlation studies in this analysis is only applied to the associated particles. The correction is done on track level, each associated track are weighted by the factor $1/\epsilon(p_T, \eta)$, where ϵ is the efficiency. For the trigger particles, namely the high p_T J/ψ, since we normalized the correlation functions by the number of trigger particles, the efficiency of the trigger particle cancel out.

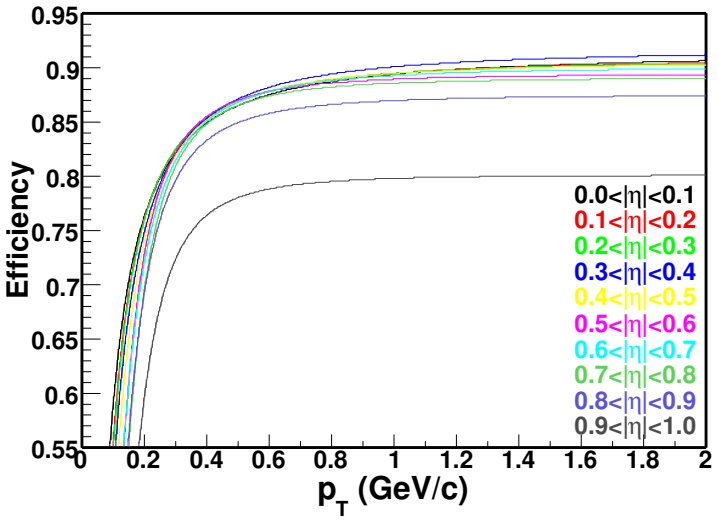

Figure 4.2: Tacking efficiency as a function of p_T in different η slices in $p+p$ collision for tracks passing through the cuts list in Tab. 4.2.

4.2.2 Acceptance

The STAR TPC has full azimuthal coverage. However it is divided into 12 sectors on each side. There are non-active areas on the boundary of each sector. Such a geometric acceptance limitation will cause the tracking efficiency to drop near the

boundary of each sector slightly depending on p_T. Thus the tracks have a non-uniform ϕ distribution even after an average tracking efficiency correction. Since it affects both trigger particles and associated particles, the effect on the correlation is a convolution of the single particle ϕ distributions. This effect is evaluated by constructing mixed event correlation functions. The method uses real tracks, both trigger and associated, pooled across a homogenous event sample and randomly selected to form a correlation. This method allows us to do the correlation on-the-fly, with the exact specification particles used in constructing the real correlation. The left panel of Fig. 4.3 shows the J/ψ-hadron azimuthal correlation function from mixed-event. The solid line represents a constant fit. The ratio of the data points to the fitted constant is shown on the right panel of the same figure. The variation of the acceptance in the $\Delta\phi$ is $< 5\%$. We did not apply this correction to the data, but took this effect as a systematic uncertainty.

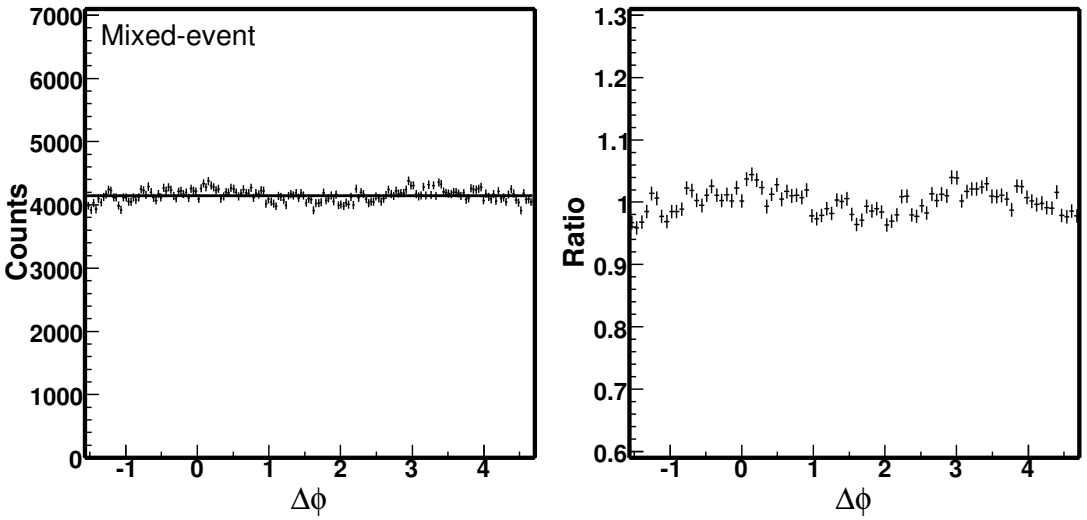

Figure 4.3: **Left:** J/ψ-hadron azimuthal correlations from mixed-event. The line represent a constant fit.
Right: Detector acceptance on $\Delta\phi$.

The TPC has good tracking in the pseudorapidity range $|\eta| < 1$, this acceptance in η causes a significant non-uniform acceptance in $\Delta\eta$ for detected correlation pairs. The left panel of Fig. 4.4 shows J/ψ-hadron $\Delta\eta$ distributions from mixed-event. The acceptance at $\Delta\eta \sim 0$ should be 100%. Thus the acceptance can be obtained by normalized the $\Delta\eta$ distribution by it maximum. The right panel of Fig. 4.4 shows the

detector acceptance in $\Delta\eta$ in our analysis. This will be used to correct the associated particle yields in the near-side ($\Delta\phi \sim 0$).

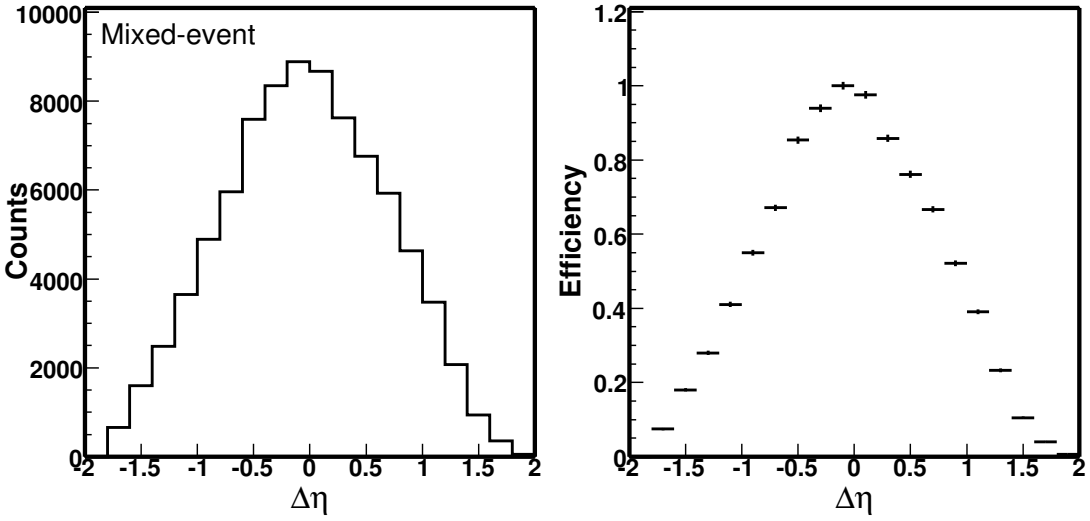

Figure 4.4: Detector acceptance on $\Delta\eta$.

4.3 Extract associated particle yields

The associated particle p_T spectra on the near side and away side are obtained in almost the same way as in Ref. [Ada05a]. The results in Ref. [Ada05a] show that on the near side, the $\Delta\eta$ distribution after efficiency and acceptance correction exhibits a jet-like peak. On the away side, the $\Delta\phi$ distribution shows a narrow jet peak but the $\Delta\eta$ distribution is much broader (and even flat in heavy-ion collisions) in a large $\Delta\eta$ range. This is confirmed by other measurements [Alv08].

Therefore, we defined the near side and away side region as $(|\Delta\phi| < 1.0, \quad |\Delta\eta| < 1.4)$ and $(\Delta\phi - \pi| < 1.0, \quad |\eta| < 1.0)$, respectively. The underlying backgrounds are subtracted to normalize the $\Delta\phi$ distribution at $\Delta\phi \sim 1.0$ to be zero. Figure 4.5 shows the associated particle p_T spectra on near side and away side. Both of them are corrected by the tracking efficiency. The p_T spectra on the near side is also corrected with the $\Delta\eta$ acceptance.

The systematic uncertainty are mainly from the underlying background subtraction

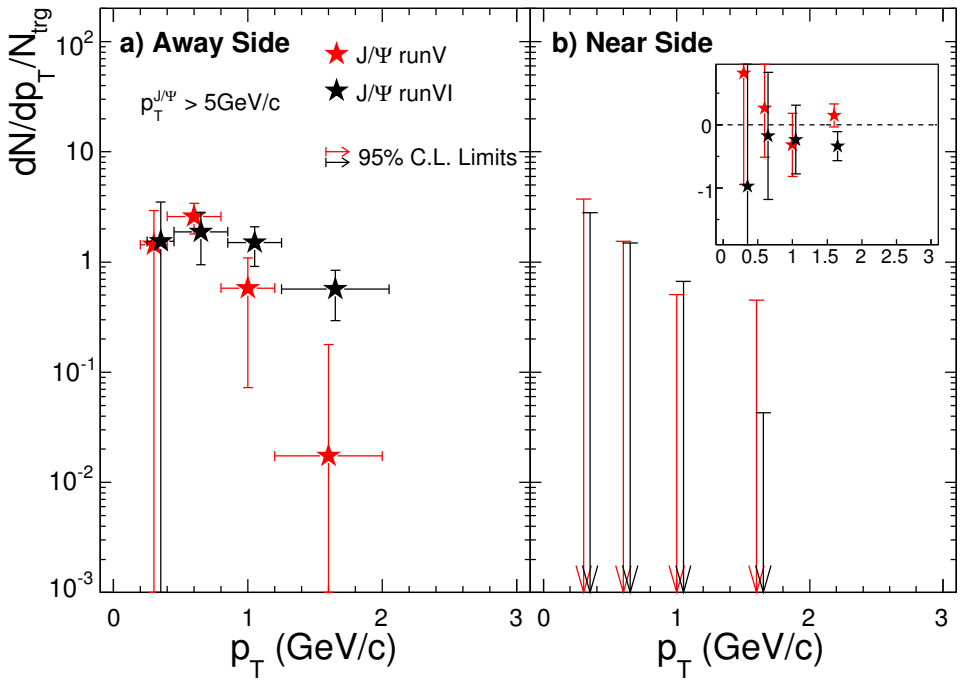

Figure 4.5: Associated particle p_T distribution on near (b) and away (a) sides in 2005 and 2006 $p+p$ collisions. The arrows on panel b) represent 95% confidence level upper limits. The insert panel shows the p_T distribution in linear scale.

due to the low statistics. We vary the normalization range to evaluate the systematics uncertainty. It is 57% for the associated particle yields on near side and 14% for the associated particle yields on away side. These is also 5% systematic uncertainty on the tracking efficiency. The combined systematic uncertainty is 58% for the yields on near side and 15% for that on away side, respectively.

4.4 Correlations from PYTHIA

We used a revised version of PYTHIA 8.108 to generate J/ψ-hadron correlation functions for J/ψs from different sources. Some parameters in the version we used were tuned by Thomas Ullrich for the STAR Heavy Flavor Working Group. Figure 4.6 shows the non-photonic electron and J/ψ p_T spectra compared to the existing measurements at RHIC. The p_T spectra in the simulation are scaled by a constant factor, the infamous K factors (3 for non-photonic electron and 0.4356 for J/ψ). The shapes match that

from the real data at RHIC very well.

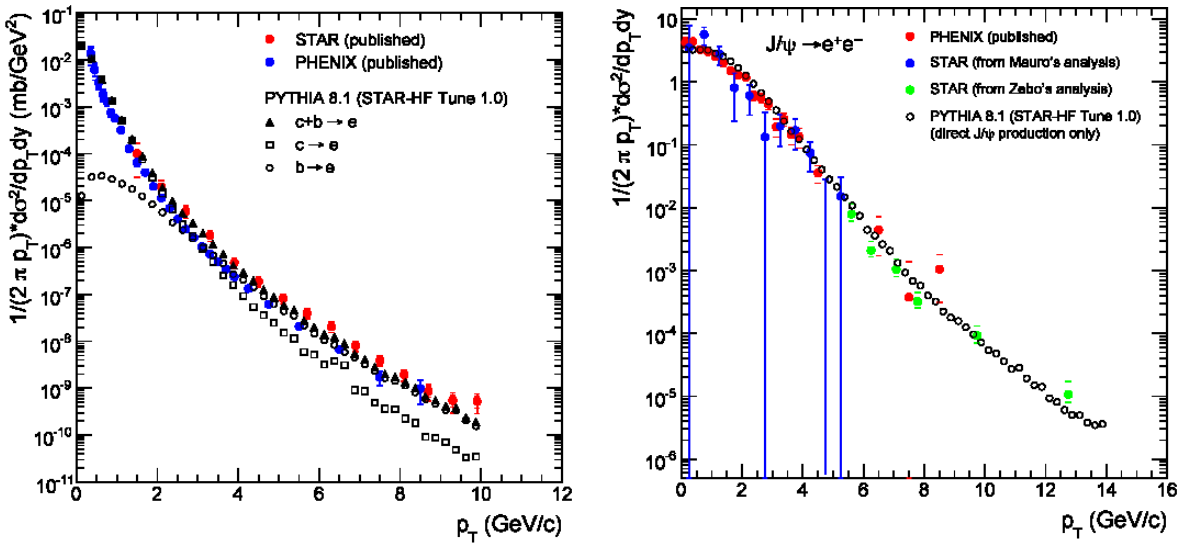

Figure 4.6: Non-photonic electron (left) and J/ψ (right) p_T spectra from PYTHIA8 compared with that in real data.

Three kinds of events are selected from PYTHIA: 1) events with prompt color singlet J/ψ , 2) events with prompt color octet J/ψ , 3) events with J/ψ from B-meson feeddown ($B \rightarrow J/\psi + X$). For 1) and 2) we did not distinguish between direct and indirect (via radiative χ_c decays) prompt J/ψ production. In all cases, the electrons from J/ψ decay were required to within STAR's acceptance ($|\eta| < 1$). Same for the charged hadrons. We only selected stable charged hadrons. Further cuts are $p_T > 5$ GeV/c for J/ψ and $p_T > 0.5$ GeV/c for charged hadrons. Figure 4.7 shows the normalized correlation functions for the various sources. The upper-left panel shows the correlation functions for J/ψ form B-meson feeddown. The near side correlation ($\Delta\phi \sim 0$) is significant, even stronger than the away side correlations ($\Delta\phi \sim \pi$). The upper-right panel show that for prompt J/ψ including color singlet and color octet J/ψ states. The near side correlations are almost flat and much smaller than the away side correlations. There is also argument that the color singlet and color octet J/ψ states can be distinguished through the J/ψ-hadron correlations since the color octet state has to radiate a gluon and probably generate stronger near side correlations. The lower panels show the correlation functions for the prompt J/ψs, left panel for color singlet

states and right panel for color octet states. The away side correlations are quite similar. For the near side correlations, there is stronger correlations for color octets, but the difference is too small to be distinguishable with the current uncertainty.

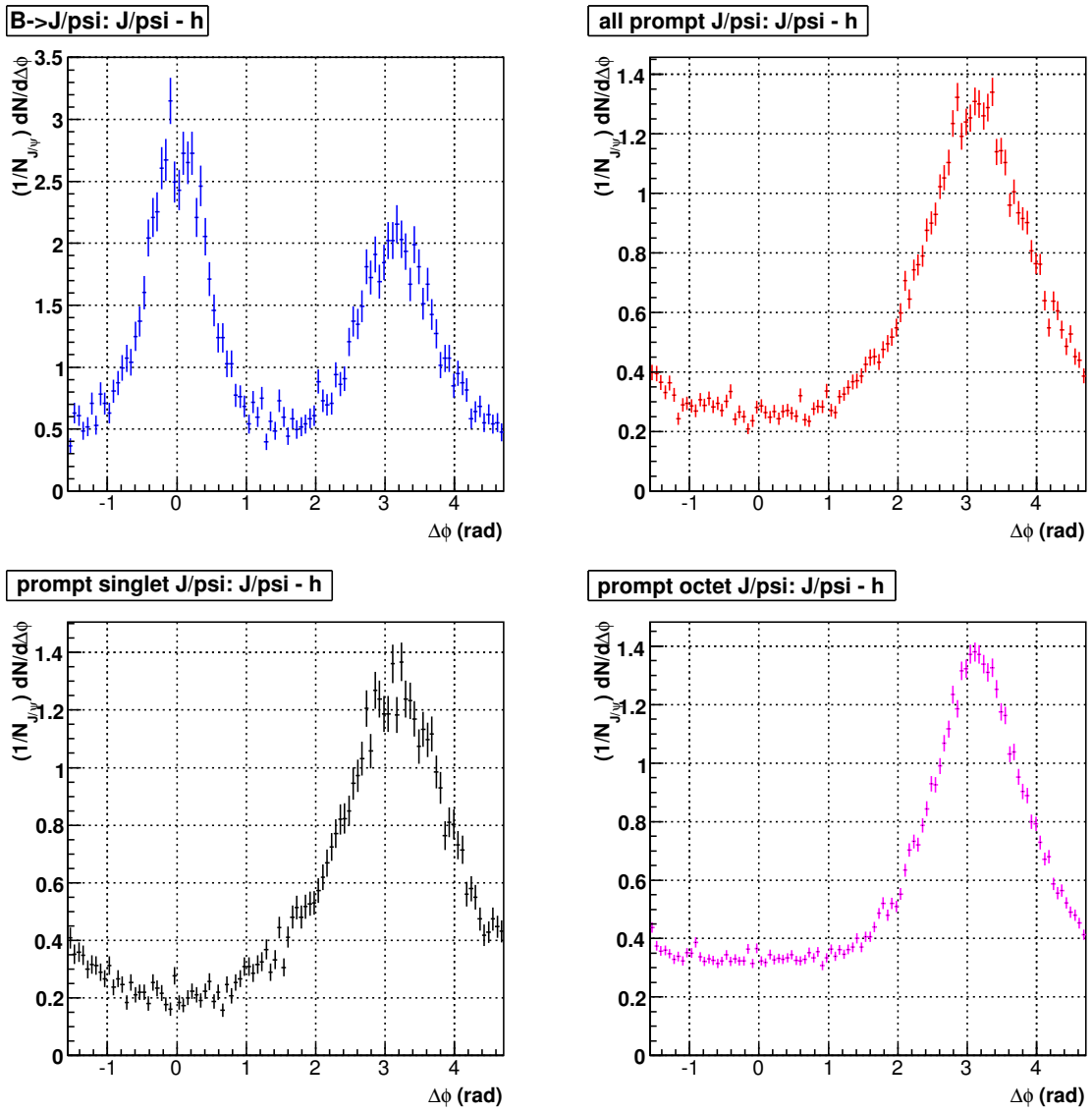

Figure 4.7: J/ψ-hadron correlation functions for J/ψ from B-meson decay (upper-left), prompt J/ψ (upper-right), prompt singlet (lower-left), prompt octet (lower-right) J/ψ.

CHAPTER 5

Results and Discussion

5.1 J/ψ p_T Spectra

We measured the high p_T J/ψ through its dielectron decay channel with a decay branch ratio of 5.9%. The left panels of Fig. 5.1 show the high p_T J/ψ invariant mass distributions in $p+p$ and Cu + Cu collisions at 200 GeV. The signal to background ratio is quite good and the statistics are listed in Tab. 3.4. The J/ψ line shape from simulation is shown as dashed line in Fig. 5.1.a. The right panel of Fig. 5.1.c shows the J/ψ p_T spectra in $p+p$ and Cu + Cu collisions. The p_T spectrum in $p+p$ collisions is extended to 14 GeV/c, which provides a good reference to the J/ψ measurements in heavy ion collisions and to theory calculations to understand the J/ψ production mechanism.

As discussed in the introduction chapter, whether the direct J/ψ is produced through either a color-singlet (CS) or color-octet (CO) transition is still a open question. The comparison of the p_T spectra to the model calculations may shed light on it. The color singlet model (CSM) described the photoproduction of J/ψ and Υ at the CERN-EMC [BJ81] and hadronic production at the CERN-ISR [BR81], but unpredicted the J/ψ p_T spectra at the Tevatron-CDF by a factor of ~ 30, especially at high p_T. The color octet model (COM) was introduced in the framework of NRQCD and provided a good description of J/ψ spectra at that energy. The calculation was also performed for RHIC energy in Ref. [CLN04, NLC03]. It concluded that the color octet production mechanism is also dominant at RHIC energy and reproduces J/ψ p_T distribution measured by PHENIX [Adl04a]. The PHENIX data was limited at $p_T < 4$ GeV/c with

large uncertainty while the calculation is only valid for $p_T > 2$ GeV/c. Therefore the PHENIX data only provided a marginal constraint on the NRQCD calculations. It is worthwhile to test the model with our p_T spectrum which has been extended to much higher p_T ($p_T \sim 14$ GeV/c) with relative smaller uncertainty. The solid line in Fig. 5.1 shows the same Leading Order (LO) NRQCD calculation extended to 15 GeV/c by Gouranga Nayak [CLN04, NLC03]. The feeddown contributions are not included in this calculation. It describes our data well up to 15 GeV/c, and leaves little room for feed-down from ψ', χ_c and B. Keep in mind that the NRQCD still can not reproduce the polarization measurement at Tevatron [Abu07]. The natural interpretation of such a failure of NRQCD is that the charmonium system is too light for relativistic effects to be neglected and that the quark-velocity expansion (v) in NRQCD may not be applicable for the rather "light" $c\bar{c}$ system.

On the other hand, the CSM describe Υ spectra at Tevatron and qualitatively reproduces its polarization after including next-to-leading order (NLO) corrections [ACL08]. The agreement is better after including α_s^5 contributions (NNLO*) [Lan08]. It also describes PHENIX J/ψ spectra at low and intermediate p_T [Ada07a] after including the s-channel cut contribution [Lan08]. The gray band in Fig. 5.1 shows the prediction from the NNLO* CS at high p_T. The band takes into account the uncertainty due to scale parameters and charm quark mass. It predicts a steeper p_T dependence compared to the NRQCD CS+CO, describes the spectra at intermediate p_T and underpredicts at higher p_T bins, which is mostly due to the CS genuine $1/p_T^8$ scaling [Lan08].

The J/ψ inclusive cross section in RHIC $p+p$ collisions was also calculated in the k_t-factorization approach, including direct CS J/ψ and feeddowns from ψ', χ_c and B mesons. It describes PHENIX spectra at low p_T ($p_T < 5$ GeV/c) and our spectra at $5 < p_T < 10$ GeV/c. The prediction is close to the NRQCD calculation. But it requires a large k_t factor and the contribution from χ_c mesons (mostly χ_{c2J}) is high (larger than the direct J/ψ production).

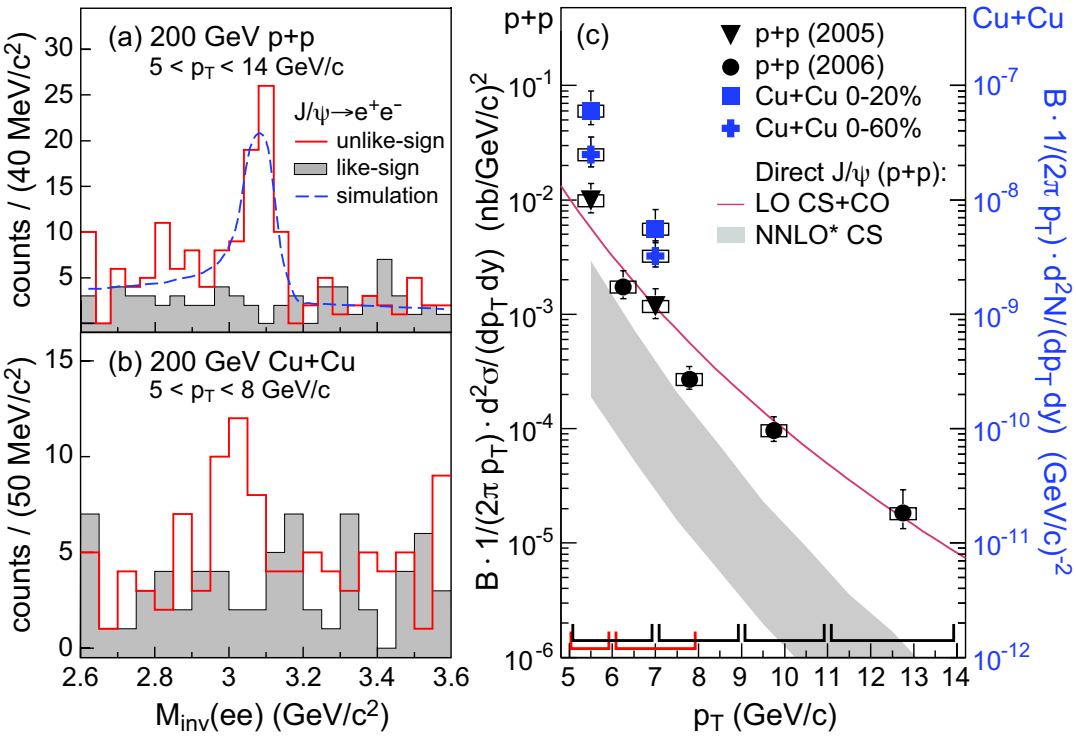

Figure 5.1: **Left:** The invariant e^+e^- mass distribution in (a) $p+p$ and (b) Cu + Cu collisions. The boxes show the systematic uncertainty. Solid lines and grey bands represent distributions of unlike and like-sign pairs, respectively. The dashed line depicts the J/ψ line shape from simulations.
Right: J/ψ invariant cross section as a function of p_T in $p+p$ and Cu + Cu collisions at $\sqrt{s_{NN}} = 200$ GeV. The bin widths are indicated by the capped lines. The solid line and the shaded band are the LO CS+CO and NNLO* CS direct yield, respectively. Both contain no feed-down contributions.

5.2 J/ψ x_T Scaling

The invariant cross sections for inclusive pion production in high energy $p+p$ collisions have been found to follow the x_T scaling law [Cla78, Ang78, Adl04b]:

$$E\frac{d^3\sigma}{dp^3} = \frac{1}{p_T^n} f(x_T) \tag{5.1}$$

or

$$E\frac{d^3\sigma}{dp^3} = \frac{1}{\sqrt{s}^n} g(x_T), \tag{5.2}$$

where $x_T = 2p_T/\sqrt{s}$ and $f(x_T)$ and $g(x_T)$ are functions of x_T. Similar scaling has been observed in e^+e^- collisions, but with $n = 0$ [Aih88, Bus95, Alb89]. The value of the power n ranges from 4 to 8 [BBK71, BBG72, ORG78]. In the general scaling form $\propto 1/p_T^n$, n depends on the quantum exchange in the hard scattering. In parton models, it is related to the number of point-like constituents taking an active role in the interaction. The value reaches 8 in the case of a quark-meson scattering by exchanging a quark. With the inclusion of QCD, the scaling law follows $1/\sqrt{s}^n$, where n becomes a function of x_T and $\sqrt{s}$. The value of n depends on the evolution of the structure function and fragmentation functions (FFs). $n = 4$ is expected in more basic scattering process (such as in QED) [EF84].

Figure 5.2 shows the x_T distributions of this data and previous J/ψ, pion and proton data from $p+p$ collisions. The J/ψ data [Abe97, Aco05, Alb91, Ada07a, Kou80] cover the range $\sqrt{s} = 30$ GeV to $\sqrt{s} = 1.96$ TeV. The STAR high p_T data covers the range $0.05 < x_T < 0.15$. J/ψ exhibits x_T scaling at only high p_T, similar to the trend for pions and protons. The power parameter n is extracted by compiling and fitting the high p_T ($p_T \gtrsim 5$ GeV/c) data at various center-of-mass energies simultaneously using the function:

$$B \times \frac{d^3\sigma}{dp^3} = A(\sqrt{s})\frac{1}{p_T^n}(1 - x_T)^m, \tag{5.3}$$

where $A(\sqrt{s})$ is a normalization factor. It is found $n = 5.6 \pm 0.2$ for J/ψ, which is smaller than that for pion and proton (6.6 ± 0.1). This suggest that the high p_T J/ψ

production mechanism is likely to originate from a $2 \rightarrow 2$ parton-parton hard scattering. It is also closer to the prediction from CO production ($n \simeq 6$) and much smaller than that from NNLO* CS production ($n \simeq 8$) [Lan08]. This is also evident from Fig. 5.1.

On the other hand, the low p_T J/ψ shows clear deviation from the x_T scaling, very similar to the behavior of the pion and proton yields at $p_T < 2$ GeV/c. Although production of low p_T J/ψ must originate from a hard process due to the mass scale, the subsequent soft process could determine the J/ψ formation and yields. This may explain why the J/ψ suppression in Au + Au collisions at RHIC is stronger at forward rapidity than at midrapidity [Ada07b]. This observation may strengthen the recent theoretical development on J/ψ production mechanism [Kha08a, Kha08b].

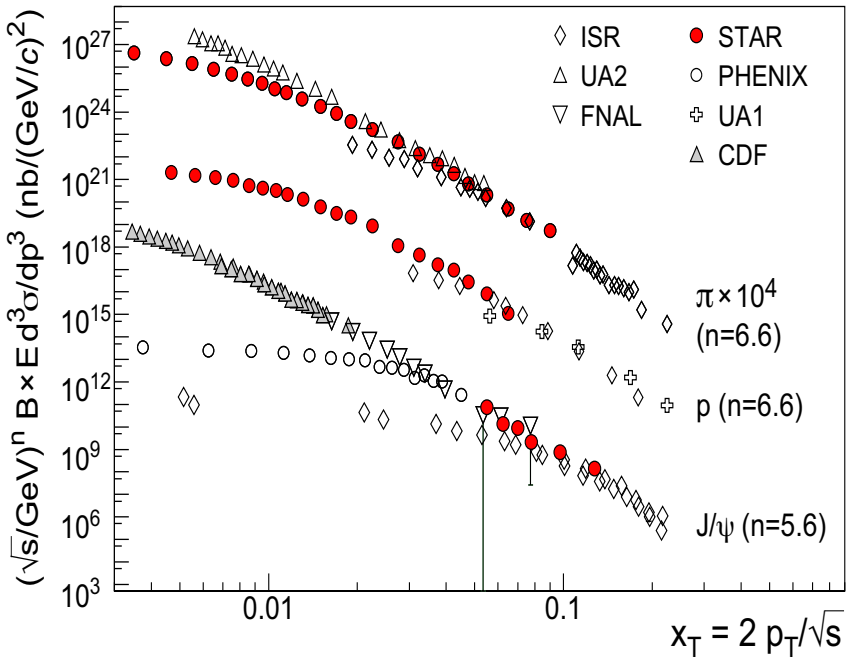

Figure 5.2: x_T distributions of pions, protons and J/ψs. The pion and proton results are from [Ban82, Ada06, Ada05d, Alp75, Ant79]. The J/ψ results from other measurements are from CDF [Aco05, Abe97], UA1 [Alb91], PHENIX [Ada07a], and ISR [Kou80].

5.3 J/ψ Nuclear Modification Factor (R_{AA})

The nuclear modification factor $R_{AA}(p_T)$, the ratio of the inclusive hadron yield in nuclear collisions to that in $p+p$ collisions scaled by the underlying number of binary nucleon-nucleon collision, measures medium induced effects on inclusive particle production. In the absence of such effects, R_{AA} is unity for hard precesses.

The high p_T J/ψ p_T spectra in 0-20% and 0-60% Cu + Cu are shown in Fig 5.1.c. The J/ψ R_{AA} at high p_T in 0-20% and 0-60% Cu + Cu collisions at 200 GeV are calculated and shown in Fig. 5.3. The low p_T J/ψ R_{AA} in 0-20% Cu + Cu collisions from PHENIX [Ada08] is also shown for comparison. The R_{AA} for J/ψ is seen to increase with increasing p_T. The average of the two STAR 0-20% data points at high p_T is $\langle R_{AA}\rangle = 1.4 \pm 0.4(stat.) \pm 0.2(syst.)$. PHENIX R_{AA} result in Cu + Cu is limited at $p_T < 5$ GeV/c, mostly due to the low statistics in $p+p$ collisions. Their Cu + Cu data is available at high p_T. Utilizing the STAR Cu + Cu and $p+p$ data and PHENIX Cu + Cu data at high p_T gives $\langle R_{AA}\rangle = 1.1 \pm 0.3(stat.) \pm 0.2(syst.)$ for $p_T > 5$ GeV/c. Both results are consistent with unity and differ by two standard deviations from PHENIX measurement at low p_T ($R_{AA} = 0.52 \pm 0.05$ [Ada08]). A notable conclusion from these data is that J/ψ is the only hadron measured in RHIC heavy ion collisions that does not exhibit significant high p_T suppression. However, for the J/ψ population in this analysis, the initial scattering partons have an average momentum fraction of ~ 0.1 (see also Fig. 5.2), suggesting that initial stat effects such as anti-shadowing may contribute to increasing R_{AA} with increasing p_T [Vog05].

The dashed curve in Fig. 5.3 shows the prediction of an AdS/CFT-based calculation, in which the J/ψ is embedded in a hydrodynamic model [Gun08] and the J/ψ dissociation temperature decreases with increasing velocity according to Ref. [LRU07]. Its p_T dependence is at variance with that of data. The dotted line shows the prediction of a two-component model including color screening, hadronic phase dissociation, statistical $c\bar{c}$ coalescence at the hadronization transition, J/ψ formation time effects, and B-meson feed-down [ZR07]. It describes the overall trend of the data

but underpredicts R_{AA} at high p_T.

The other calculations in Fig. 5.3 provide a comparison to open charm R_{AA}. The solid line is based on the WHDG model for charm quark energy loss, with assumed medium gluon density $dN_g/dy = 254$ for 0-20% Cu + Cu [Wic07]. The dash-dotted line shows a GLV model calculation for D-meson energy loss, with $dN_g/dy = 275$ [AV07]. Both models, which correctly describe heavy flavor suppression in Au + Au collisions, predict charm meson suppression of a factor ~ 2 at $p_T > 5$ GeV/c. This is in contrast to the J/ψ R_{AA}, which is a measurement of hidden charm production. This comparison suggests that high p_T J/ψ production does not proceed dominantly via a channel carrying color. However, other effects may compensate the loss in this p_T range [ZR07].

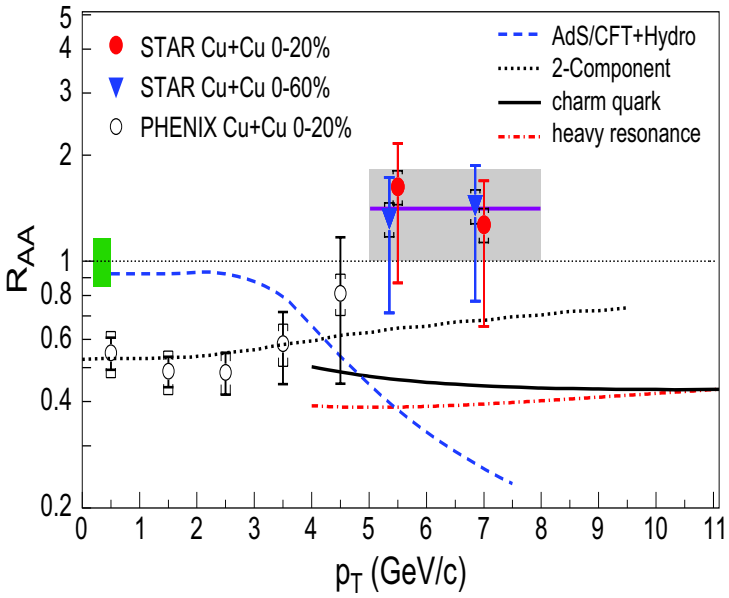

Figure 5.3: J/ψ R_{AA} as a function of p_T. The caps show the systematic uncertainty. The solid line and the band in the middle represent the average of STAR 0-20% results and its error. The box on the left reflects the normalization uncertainty including 14% from the $p+p$ results and 7% from the number of binary collisions. The curves are calculations based on various models described in detail in the text.

5.4 J/ψ-hadron Correlation

Thanks to the good S/B ratio, we measured the azimuthal correlation between high p_T J/ψ and charged hadrons in 200 GeV $p+p$ collisions. Since the correlation functions in 2005 and 2006 data are quite similar although the p_T coverage is a little different, we combined the correlation function from these two datasets. The combined results are shown in Fig. 5.4. There is no significant enhancement in the near-side correlated yield ($\Delta\phi \sim 0$), in contrast to dihadron correlation measurements [Ada05a], where the amplitude of the near side jet-like peak is significant and comparable to that on the away side.

Since the Monte Carlo simulations show a strong near side correlation if the J/ψ is produced from B-meson decay [Alb91, Alb88], these results can be used to constrain the B-meson contributions to J/ψ production. The contribution to the J/ψ-hadron correlation from B-meson decay and prompt J/ψ were simulated with the same kinematic acceptance in PYTHIA events as discuss in 4.4. The correlation functions from data can be decomposed as:

$$C_{all}(\Delta\phi) = \frac{D_{prompt}(\Delta\phi) + D_{B\to J/\psi}(\Delta\phi)}{N_{prompt} + N_{B\to J/\psi}} \tag{5.4}$$

where $C(\Delta\phi)$ is the correlation function and $D(\Delta\phi)$ is the raw correlation distribution (before normalization). It can be rewritten as:

$$C_{all}(\Delta\phi) = \frac{N_{prompt} \times C_{prompt}(\Delta\phi) + N_{B\to J/\psi} \times D_{B\to J/\psi}(\Delta\phi)}{N_{prompt} + N_{B\to J/\psi}} \tag{5.5}$$

$$r \equiv N_{B\to J/\psi}/(N_{prompt} + N_{B\to J/\psi}) \tag{5.6}$$

$$C_{all}(\Delta\phi) = r \times C_{prompt}(\Delta\phi) + (1-r) \times C_{B\to J/\psi}(\Delta\phi) \tag{5.7}$$

The solid curve in Fig. 5.4 shows the fit result with $\chi^2/ndf = 27/19$. The dashed and dot-dashed lines depict the contributions from prompt J/ψ and J/ψ from B-meson decay. The fraction of B-meson feeddown contribution to the inclusive J/ψ yields at $p_T > 5$ GeV/c is found to be $13 \pm 5\%$. The simulation also shows that the correlation

function from fragmentation has large peaks on both near side and away side correlation. This indicates the jet fragmentation function contribution is small.

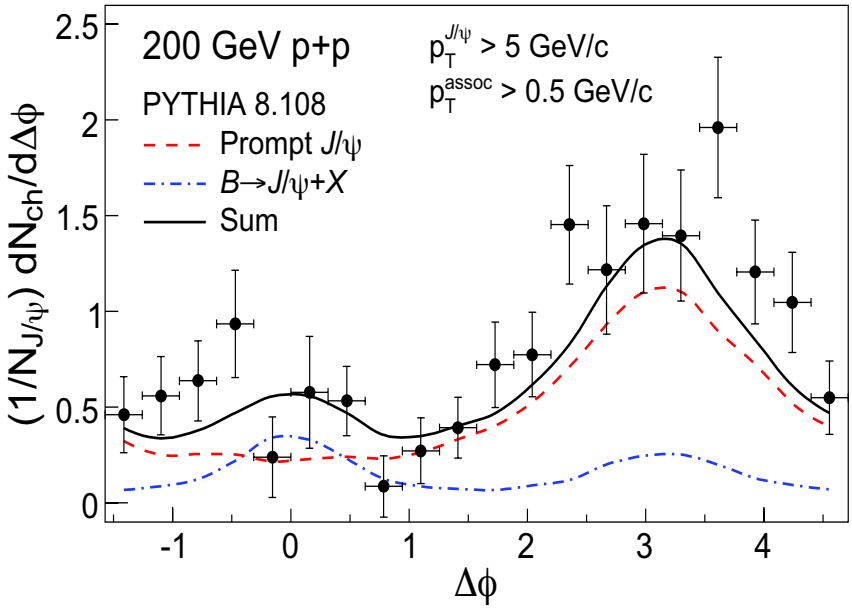

Figure 5.4: J/ψ-hadron azimuthal correlations after background subtraction. The dashed (dot-dashed) curves represent the contributions of J/ψ from prompt and B-meson feed-down obtained from PYTHIA respectively. The solid line shows the sum of them.

The B-meson contribution was also from the comparison of pQCD prediction for B productions with the measured J/ψ inclusive yield. We started with the B spectra from pQCD calculation [CNV05]. The calculation for B spectra at Tevatron from the same model describes the CDF measurement [Aco05]. The B was then decayed into J/ψ in the rest frame of B according the decay form factor measured by CLEO Collaboration [AFK02], and then transfer to the laboratory frame. The resulting J/ψ yield from B were divided by our inclusive J/ψ spectra and shown in Fig 5.5 in open stars. The band shows the uncertainty from the B spectra. It shows that the fraction of J/ψ from B-mesons feeddown at high p_T is sensitive to the B-meson cross section. Since a significant part of J/ψ is from B decay if the pQCD calculation is correct, the combination of inclusive J/ψ spectra and fraction of B-meson contribution from J/ψ-hadron correlation with better statistics can give a good constraint to the B production. Another independent constraint on the B production can be obtained by

combining the non-photonic cross section measurements [Ada05c, JC09, Abe07] and $B \to e/D \to e$ ratio through the correlations between non-photonic electron and charged hadron [Lin07, Wan08].

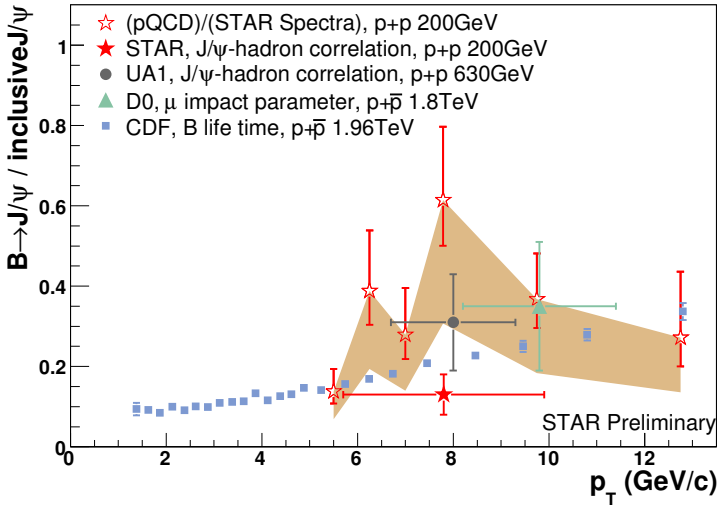

Figure 5.5: Fraction of $B \to J/\psi + X$ over the inclusive J/ψ from different measurement at UA1, STAR, D0 and CDF.

The p_T spectra of associated particle with respect to high p_T J/ψ are also measured and compared to that of high p_T charged hadrons (Fig. 5.6). On the near side, the associated charged particle hadron yields with respect to J/ψ triggers are significantly lower than those with respect to charged hadron triggers. On the away side, the yields of the associated charged hadrons with respect to J/ψ triggers and charged hadron triggers are consistent with each other, which indicates that the hadrons on the away side of J/ψ triggers are from light quark or gluon fragmentation.

5.5 Summary

In summary, we measured the J/ψ spectra from 200 GeV $p+p$ and Cu + Cu collisions at high p_T ($p_T > 5$ GeV/c) at mid-rapidity through the dielectron channel at STAR at RHIC. The high p_T J/ψ production was found to follow the x_T scaling with a beam energy dependent factor $\sim \sqrt{s}^{5.6\pm0.2}$ at high p_T and fails the x_T scaling test at low p_T. The J/ψ nuclear modification factor R_{AA} in Cu + Cu increase from low to high p_T

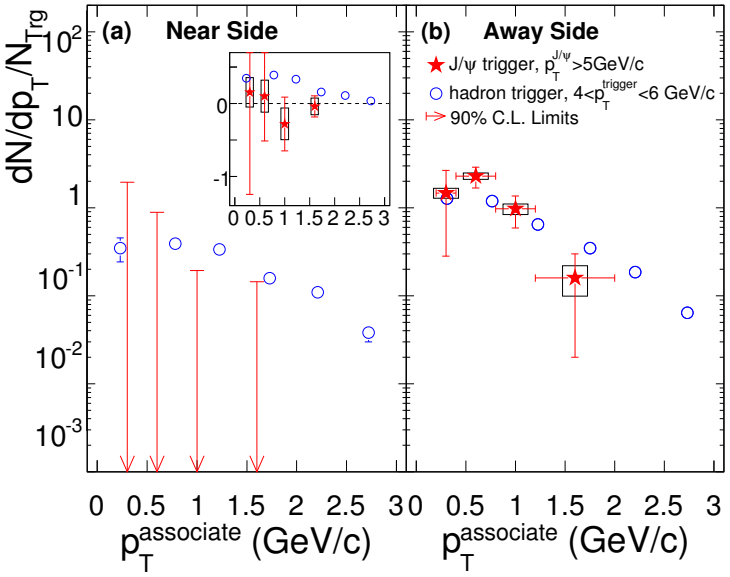

Figure 5.6: Associated charged hadron p_T distribution on the near and away side with respect to high p_T triggers and charged hadrons. The boxes represent the systematic uncertainty. The arrows on the left panel depict the 90% confidence level upper limits. The inset shows the associated particle p_T spectra on the near side in linear scale.

and is consistent with no J/ψ suppression for $p_T > 5$ GeV/c, in contrast to the prediction in a strong coupled liquid. Based on the measurement of azimuthal correlations and the comparison to model calculations, we estimate the fraction of J/ψ from B-meson decay to be $13 \pm 5\%$ at $p_T > 5$ GeV/c.

CHAPTER 6

Outlook

6.1 Detector Upgrades

STAR has proposed several detector upgrades related to this analysis: Data Acquisition (DAQ1000), Time-Of-Flight (TOF), Heavy Flavor Tracker (HFT), Muon Telescope Detector (MTD) and Forward Meson Spectrometer (FMS).

6.1.1 DAQ1000

The TPC is the slowest detector in STAR. Almost all of the other detectors in STAR have data acquisition (DAQ) rate larger than 1000 Hz. While the TPC DAQ rate is limited to < 100 Hz. This prevents us from taking advantage of the increasing high luminosity of RHIC. With the same luminosity, PHENIX can take central Au + Au data at a few kHz and $p + p$ data at approximately 500 kHz. But STAR can only take both $p + p$ and Au + Au data at approximate 80 Hz.

To improve the DAQ rate, STAR has proposed to replace the TPC readout and Data Acquisition electronics by the CERN/ALICE developed chips and fiber optic link in 2005. This upgrade will significantly improve STAR's data taking capabilities and will be beneficial to all of STAR's current and foreseen physics programs. The expected DAQ rate with the new DAQ system is more than 1 kHz, being well matched will the STAR's other detectors. This is where this new project "DAQ1000" names from.

The DAQ1000 increases STAR's data taking rate more than 20 times for minimum bias Au + Au collisions. It will increase the data taking rate by up to 50 times in other collision systems (or energies) where the number of measured tracks in the TPC is

smaller. In the case of rare physics (high p_T particles, jets, forward π^0, J/ψ , Υ etc.), the major benefit of the DAQ1000 is the decrease in the TPC/DAQ deadtime while at the same time maintaining the high rate for soft physics. Due to the current DAQ constraints, STAR is running typically at a 50 Hz rate at 50% associated deadtime. The 50 Hz of events also typically contain about 20-30 Hz of soft physics events (minimum bias) while the other 20 Hz are reserved for the rare triggers. With the DAQ1000, STAR would essentially run deadtimeless thus harvesting two times more rare probes while at the same time acquiring the soft physics. This would be effectively equivalent to a factor of two increase of RHIC's average luminosity.

The DAQ1000 installation has been completed in RHIC 2009 run.

6.1.2 Time-Of-Flight

The proposed full barrel TOF detector would surround the outer edge of the TPC, and cover $-1 < \eta < 1$ and $\sim 2\pi$ in azimuthal. By using the recently developed technology-MRPC, the TOF system can achieve the required timing resolution < 100 ps and the required particle detecting efficiency $> 95\%$. This will significantly improve the STAR PID capability: π/K separation range can be extended from 0.7 GeV/c to 1.6 GeV/c and p/(π, K) separation range can be extended from 1.1 GeV/c to ~ 3 GeV/c.

For electron, the TPC almost have no identification capability at low p_T because the electron dE/dx crosses that of all of the other hadrons at low p_T. Due to the excellent PID capability at low p_T, the TOF can be used to get rid of kaon and proton and suppress pion at low p_T. Figure 6.1 shows the TPC measured dE/dx distribution as a function of p_T with and without the TOF measured $1/\beta$ cut [Ada05c]. The combination of the TOF and the TPC can provide a very good electron ID at low and intermediate p_T. At higher p_T, the BEMC can be used to suppress hadrons. The TOF+TPC+BEMC can provide a continuous electron identification at a large p_T range ($p_T > 0.2$ GeV/c).

This will obviously significantly improve the J/ψ reconstruction at low p_T where the J/ψ is difficult to be triggered at STAR thus can be only reconstructed in minimum

bias events. At higher p_T, the electron identification is mostly from BEMC and TPC, but since the TOF is only sensitive to charge particle, it can be used to reject the neutral particle (γ, π^o etc.) firing the high tower trigger. This can significantly enhance the high tower trigger rate especially at low threshold.

The TOF has 75% coverage in RHIC 2009 run and will have full coverage from RHIC 2010 run.

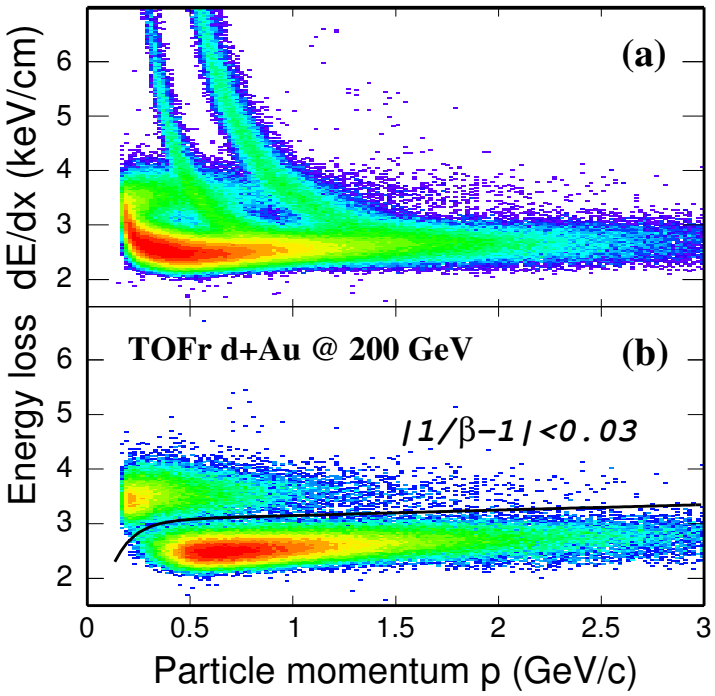

Figure 6.1: dE/dx as a function of p_T in 2003 d + Au run with (a) and without (b) TOF measured $1/\beta$ cut.

6.1.3 Heavy Flavor Tracker

The proposed Heavy Flavor Tracker (HFT) will consist of 4 layers of silicon detectors grouped into two sub-systems with different technologies, guaranteeing increasing resolution when tracking from the TPC and the SSD. The innermost two layers are silicon pixel detector (PIXEL), 2.5 cm away from the interaction point, bringing extremely high precision tracking capabilities to STAR with a resolution of 10 μm at the first layer of the detector, over a large pseudo-rapidity range, and with

complete azimuthal angular coverage. This will enable STAR to perform high precision measurements of heavy quark production over broadest range of phase space, colliding systems and energies.

This detector will significant improve the resolutions of both primary vertex and secondary vertices. The main goal of HFT is the topological reconstruction of D^0 meson ($c\tau = 123\ \mu m$). This precise measurements on D-meson will provide the total charm cross section thus helps the understanding of the charmonuim production mechanism.

The another two main benefits from the HFT for the J/ψ analysis are: 1) topologically reconstruct $B \rightarrow J/\psi + X$; 2) reduce electron background;

The B mesons is one of the main sources of the inclusive J/ψ especially at high p_T. Theorists usually can only provide the prediction for direct J/ψ or prompt J/ψ (including feed-down from ψ' and/or χ_cs). But have the difficult to predict contribution from the B-mesons on the same time. The precise measurement of the $B \rightarrow J/\psi$ fraction will be helpful to extend our knowledge on the J/ψ production mechanism. The B-mesons have $c\tau > 450\ \mu m$, about 4 times of that for D-mesons. The high resolution of primary and secondary vertices provided by the HFT will make the topological reconstruction of $B \rightarrow J/\psi + X$ possible.

The TOF+TPC+EMC can provide a pretty clean electron sample, but they are, to a large extent, background for the J/ψ analysis, especially in heavy ion collisions. They originate from gamma converting into electron-position pairs, in the detector material, from π and η Dalitz decays, and from semi-leptonic decay of heavy quark hadrons. The PIXEL detector of the HFT makes it possible to reject conversion background originating outside the inner PIXEL detector by requiring hits in the PIXEL detector of the HFT. The requirement of hits on both PIXEL layers can reduce the electron from photon conversions by a factor of 16. In additional, the HFT make it possible to reject physics background from semi-leptonic decays of heavy quark hadrons. This background originates from a secondary vertex that is displaced by about 100 μm that can be measured with the high resolution provided by the HFT.

6.1.4 Muon Telescope Detector

Another way to get rid of the background from gamma conversion and π^0, η Dalitz decays is reconstructing the J/ψ through its dimuon channel. So far STAR only have muon capability at $0.17 < p_T < 0.25$ GeV/c from TOF. This is not useful for the J/ψ analysis. STAR is proposing a muon detector, the Muon Telescope Detector (MTD), which will be very suitable for J/ψ analysis.

The MTD is proposed to surround the STAR Magnet, covering $|\eta| < 0.8$ and $\sim 60\%$ of 2π in azimuthal due to gaps between modules, using the BEMC and Magnet steel as hadron absorber. It is also based on the MRPC technique, but with large modules, long stripes and double-ended readout (Long-MRPC). This detector would have timing resolution < 100 ps and spatial resolution ~ 1 cm. The simulation found that the muon detection efficiency at $p_T > 2$ GeV/c is 40-50% including acceptance effect. While for the pion, the efficiency is 0.5-1%. The efficiency for proton is significantly lower than for other hadrons. A prototype installed in 2008 worked very well. It shows that the muon to hadron background ratio can achieve 12:1 even the electronics is not optimized for this detector yet. Even though lots of the muons are secondary muons, from pion and kaon weak decay, the J/ψ analysis is still benefit a lot from this analysis. The upper panel of Fig. 6.2 shows the expected invariant mass distribution of dimuon pair decayed from J/ψ and from background. In d + Au (central Au + Au) collisions, the signal to background ratio for J/ψ at high p_T can reach 7 (2). This signal to background ratio is even much better than what we got from 2006 $p+p$ data through the dielectron channel.

Unlike electron, which radiates energy in the detector material through the bremsstrahlung, the muon rarely interacts with the detector material. Thus the J/ψ and Υ have better mass resolution through the dimuon channel. The lower panel of Fig. 6.2 shows the expected invariant mass distribution for dimuon pairs decayed from different Υ states($\Upsilon(1S)$, $\Upsilon(2S)$ and $\Upsilon(3s)$). Clearly, these states can be separated.

The MTD is only sensitive to muon, its hadron rejection is much higher than that for BEMC. The MTD is a better heavy flavor trigger than BEMC and will enhance the

recorded luminosity a lot. For example, in 2008 d + Au run, the STAR high tower trigger only recorded 0.34 nb^{-1} at $E_T > 2.6$ GeV, 2.1 nb^{-1} at $E_T > 3.6$ GeV, 8.4 nb^{-1} at $E_T > 4.3$, but recorded 33.5 nb^{-1} at $E_T > 8.4$ GeV. The reason we took less integral luminosity at lower threshold is that at lower threshold, the trigger rate is too high for the DAQ and we had to prescale them down with different factors. Lots of high tower triggered data actually are triggered by high p_T hadrons and neutral particles which are useless for the quarkonium analysis. There are lots of room for MTD to take advantage of the full RHIC luminosity, with reasonable trigger efficiency at intermediate and high p_T, to trigger quarknonium. Not only enhance the recorded luminosity, the MTD trigger capability for quarkonium will also significantly reduce the data size and thus allows us to reconstruct the events timely.

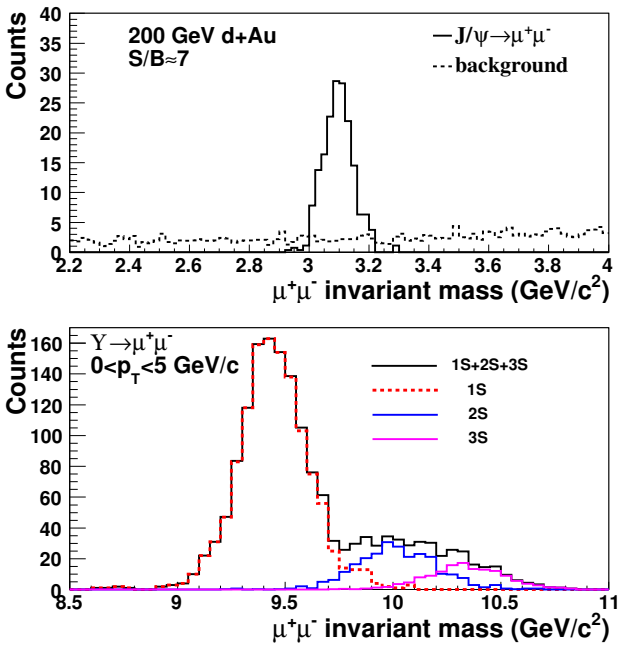

Figure 6.2: The expected di-muon invariant mass distribution from J/ψ and Υ and background for J/ψ in d + Au collisions.

6.1.5 Forward Meson Spectrometer

The PHENIX Collaboration found that the J/ψ suppression is larger in forward rapidity than in mid-rapidity [Ada07b], which is still challenging our understanding on the J/ψ production in heavy ion collisions. One of the possible explanations is the gluon saturation effect [Kha08a, Kha08b], but it is still unclear yet. The J/ψ measurement at forward rapidity at STAR is interesting and needed.

The STAR proposed Forward Meson Spectrometer (FMS) is a electromagnetic calorimeter with complete azimuthal coverage for the pseudorapidity interval $2.5 < \eta < 4.0$. It can be used to reconstruct J/ψ in $0.2 < x_F < 0.8$ with reasonable efficiency. This will extend the phase space of the J/ψ measurements at RHIC.

6.2 J/ψ Measurements in Au + Au Collisions

Our J/ψ R_{AA} measurements in Cu + Cu collisions is the first time to be used as a prob to test the J/ψ production mechanism. It extended our knowledge on the J/ψ production. But due to the smaller system size and lower energy density, the particle suppression is smaller in Cu + Cu than in Au + Au collisions. For example the non-photonic electron R_{AA} at high p_T is around 0.2 in central Au + Au collisions but around 0.5 in central Cu + Cu collisions. Due to the big uncertainty, the J/ψ R_{AA} measurements at high p_T in Au + Au collisions will provide a better constraint on the J/ψ production mechanism than in Cu + Cu collisions.

Table 6.1 shows the thresholds, luminosity of high tower triggered data in RHIC 2007 Au + Au run. In 2007 Au + Au collisions, STAR collected about twice pp-equivalent integrated luminosity of that in 2006 $p + p$ collisions with the similar threshold. Even though the signal to background in Au + Au collisions is a little bit lower than that in $p + p$ collisions, we should still be able to reconstruct the J/ψ at high p_T using the high tower triggered data in 2007 Au + Au triggered data.

In the near future, the upgrade of the RHICII luminosity will allows us improve our

Table 6.1: High tower triggered events in 2007 Au + Au collisions.

Trigger	Threshold	Luminosity	pp-equivalent luminosity
1	$E_T > 4.3$ GeV	50.6 μb^{-1}	2 pb^{-1}
2	$E_T > 5.5$ GeV	505.7 μb^{-1}	19.6 pb^{-1}

statistics a lot. Figure 6.3 shows the expected J/ψ R_{AA} at high p_T with 2 nb^{-1} Au + Au collisions and 50 pb^{-1} $p+p$ collisions compared to PHENIX measurements at low p_T [Ada07b]. With the RHICII high luminosity, we would be able to provide a good J/ψ R_{AA} measurement at high p_T.

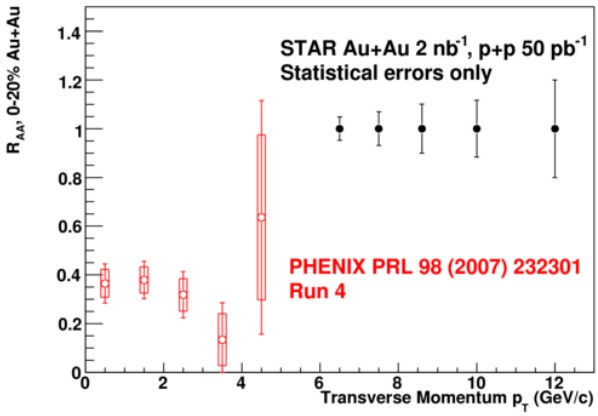

Figure 6.3: The expected J/ψ R_{AA} at high p_T with 2 nb^{-1} Au + Au collisions and 50 pb^{-1} $p+p$ collisions compared to PHENIX measurements at low p_T [Ada07b].

The J/ψ v_2 measurements can be used to investigate whether a J/ψ is produced initially or formed later from the $c\bar{c}$ recombination in a deconfined phase. The PHENIX measured J/ψ v_2 using 2007 Au + Au data but have huge uncertainty [Sil08]. In STAR, due to the about 6 times larger acceptance, we would be able to essentially measure the J/ψ v_2 precisely. From the electron identification from TOF+TPC+EMC, with 1000 M minimum bias Au + Au events, we can reconstruct about 144000 J/ψs and give a 0.3% statistical uncertainty on v_2.

6.3 J/ψ Measurements in d + Au Collisions

The J/ψ suppression in relativistic heavy ion collisions due to the color screening effect was proposed as a signature of QGP formation. But the so-called cold nuclear matter effects, including modification of initial parton distribution functions (shadowing, gluon saturation, anti-shadowing, EMC effect, etc), initial- and final-state partonic multiple scattering, and related initial-state parton energy loss need to accounted for before firm conclusions can be drawn about the effect of the hot medium thought to be created. In fact, there various cold nuclear matter effects are interesting in their own right, notably in terms of hadronization time scales, parton energy loss in matter, and the various initial-stat effects just mentioned. The cold nuclear matter effects are usually studied by using the p+A collisions. The RHIC 2008 d + Au run is very suitable for this purpose.

Table 6.2: J/ψ in 2008 d + Au collisions.

Item	HT0	HT1	HT2
Threshold (GeV)	2.6	3.6	4.3
Integrated Luminosity (nb^{-1})	0.34	2.1	8.4
pp-equivalent Luminosity (pb^{-1})	0.14	0.8	3.3
J/ψ Signals	71 ± 15	120 ± 16	194 ± 20
Significance (σ)	4.3	7.3	9.5

In 2008 d + Au run, STAR reduced the material budget inside the TPC by a factor of ~ 10 by removing the SVT and SSD. The sample integrated luminosity with different thresholds are list in 6.2. Figure 6.4 shows the J/ψ invariant mass distribution and p_T coverage from 2008 d + Au data. We observed about 420 J/ψ signals at $p_T > 2.5$ GeV/c with significance = 13. This is the most significant J/ψ signal observed in STAR so far, even at such a high p_T range. The line shape is also better due to the removing material. The raw p_T distribution is shown on the right panel of Fig. 6.4. The efficiency uncorrected p_T spectra and the expected statistical uncertainties on the spectra from different triggers are shown in Fig. 6.5. The number of signals and significances are list in Tab. 6.4. With such a good signal, we should be able to provide a very good

constraint on the cold nuclear matter effects on the J/ψ production.

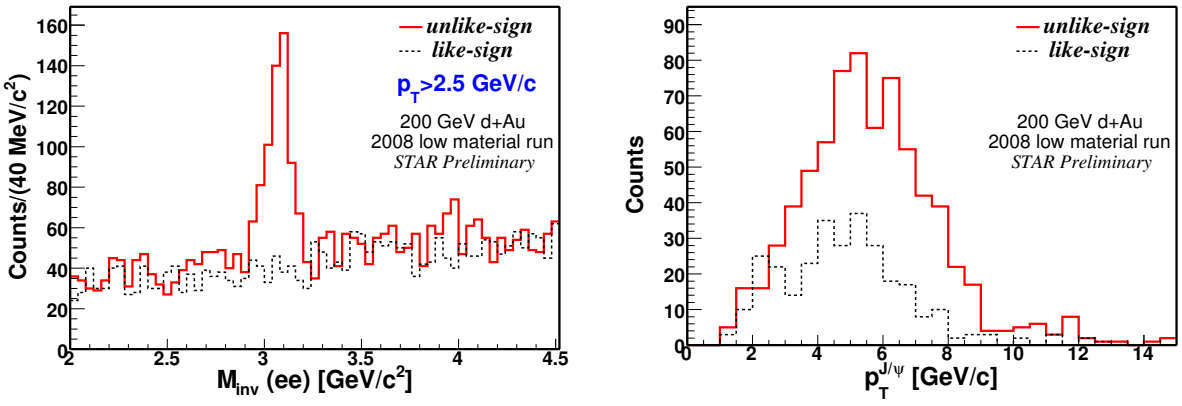

Figure 6.4: **Left:** Invariant mass distribution of unlike-sign (solid line) and like-sign (dashed line) electron pairs from 2008 d + Au data.
Right: Raw p_T distribution of unlike-sign (solid line) and like-sign (dashed line) electron pairs with $2.9 < M_{inv}(ee) < 3.2$ GeV/c^2

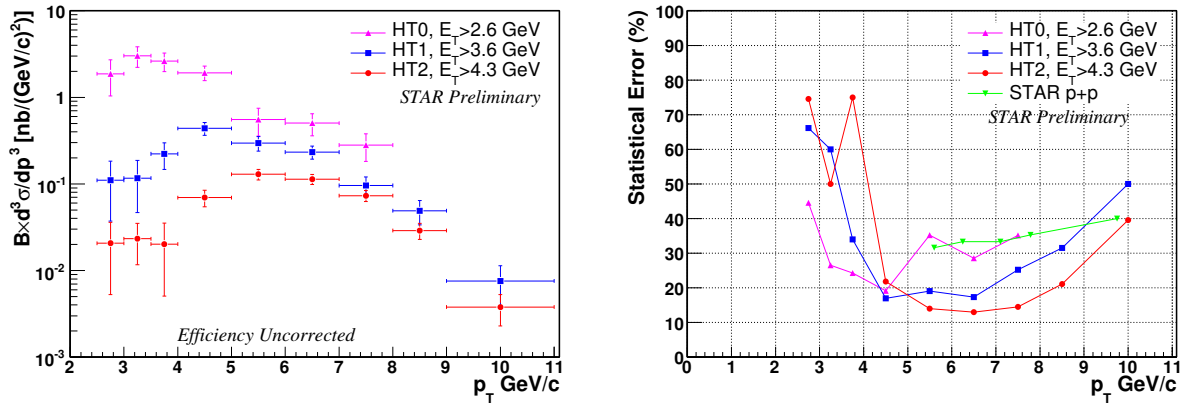

Figure 6.5: **Left:** J/ψ raw p_T spectra in 2008 d + Au collisions from different triggers.
Right: Expected statistical uncertainties for J/ψ p_T spectra in 2008 d + Au collisions.

Figure 6.6 shows the J/ψ-hadron azimuthal correlation function in 2008 d + Au collisions. The curve depicts the constant+Gaussian function fit. The Gaussian function represent the peak on the away side. It confirms the $p+p$ results, no significant near side correlation on the near side. But the high statistics in 2008 d + Au data will allow us to do the correlation study in more detail.

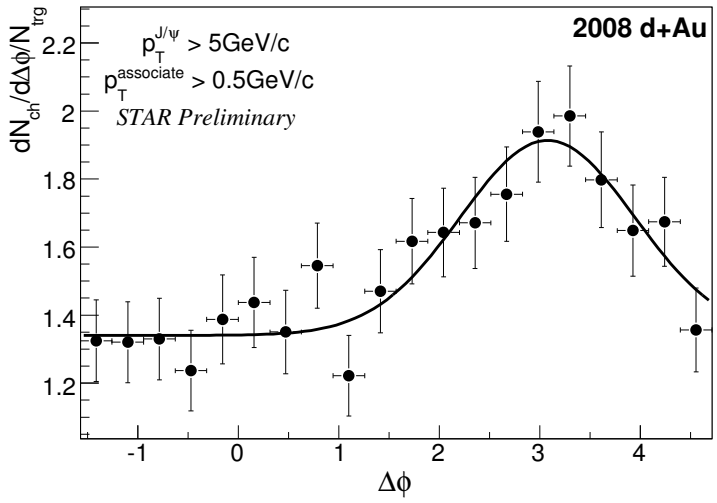

Figure 6.6: J/ψ-hadron azimuthal correlation function in 2008 d + Au collisions, the curve depicts a constant+Gaussian function fit.

6.4 Reconstruction of Other Charmonium States

To date, people only reconstructed J/ψ and ψ' through dielectron and dimuon channels and χ_cs through the $\gamma J/\psi$ channel at RHIC. The ψ' and χ_cs are only used to estimate the feeddown for J/ψ with large uncertainty [Oda08]. The different charmonium states is unnecessary to have the same production mechanism and same behavior in cold and hot matter. The direct measurements of these lowest states of charmonium are of great interests.

The ground state of charmonium, η_c, is mostly measured in low energy e^+e^- collisions through the decays of J/ψs and B decays and diphoton channel, focusing on the mass, width, and decay branching ratios [Bra04]. The η_c reconstruction in high energy $p+p$ and/or heavy ion collisions will provide additional information on its production. The $\eta_c \to p\bar{p}$ branching ratio is $(1.3 \pm 0.4) \times 10^{-3}$, about 5 times of that for the diphoton channel (BR=$(2.8 \pm 0.9) \times 10^{-4}$). In STAR, the TOF can identify proton up to 3 GeV/c. At high p_T, the proton dE/dx measured by TPC is about 1σ away from that for kaon and $> 2\sigma$ away from that for pion. With the large acceptance, STAR may try to reconstruct η_c through the diproton channel. RHIC is running 500 GeV $p+p$ collisions this year (2009), the quarkonium total cross section is believed to be ≥ 2 times

of that in 200 $p+p$ collisions. With 75% TOF coverage, this data is a great chance for η_c searching at RHIC.

The χ_cs are usually reconstructed though the $\gamma J/\psi$ channel. In the reconstructed χ_cs, there is few χ_{c0} due to its small branching ratio to $\gamma J/\psi$ (BR=(1.30 ± 0.11)%). The finding of the soft photon efficiently with good resolution is a big challenge to the EMC. This problem is more crucial in STAR, where the EMC is designed for high p_T physics and difficult to identify low energy photon. However, the STAR TPC+TOF can identify pion and kaon up to 1.6 GeV/c and proton up to 3 GeV/c with > 70% efficiency including tracking and PID efficiency. It is worthwhile to try to reconstruct the χ_cs through the hadronic channels.

Table 6.3: The Branching Ratio (BR) of different charmonium decay channels.

Charmonium	$\gamma J/\psi$	$\pi^+\pi^-$ ($\times 10^{-3}$)	K^+K^- ($\times 10^{-3}$)	$p\bar{p}$ ($\times 10^{-3}$)
η_c				(1.3 ± 0.4)
J/ψ		0.147 ± 0.023	0.146 ± 0.026	2.17 ± 0.08
χ_{c0}	(1.3 ± 0.11)%	7.2 ± 0.6	5.4 ± 0.6	0.224 ± 0.027
χ_{c1}	(35.6 ± 1.9)%			0.0067 ± 0.005
χ_{c2}	(20.2 ± 1.0)%		0.77 ± 0.14	0.066 ± 0.005
	e^+e^- ($\times 10^{-3}$)	$J/\psi\pi^+\pi^-$	$p\bar{p}$ ($\times 10^{-4}$)	
ψ'	7.35 ± 0.18	(31.8 ± 0.6)%	1.28 ± 0.35	

Table 6.3 shows the branching ratio of χ_cs decay into $\pi^+\pi^-$, K^+K^- and $p\bar{p}$. For χ_{c0}, the BR to $\pi^+\pi^-$ and K^+K^- is about 1/10 of the $J/\psi \to e^+e^-$. But BR of $\chi_{c0} \to \gamma J/\psi$ is only 1.3%. The BR for $\chi_{c0} \to \pi^+\pi^-$ *or* K^+K^- is ~ 10 times of that for $\chi_{c0} \to \gamma J/\psi \to \gamma e^+e^-$ *or* $\gamma\mu^+\mu^-$. For χ_{c1} and χ_{c2}, they mass difference is too small and usually can not be separated through the $\gamma J/\psi$ channel. But in K^+K^- (or even $p\bar{p}$) channel, χ_{c1}'s decay BR is much smaller than that for χ_{c2}, thus only the χ_{c2} is possible to show up on the invariant mass distribution. The reconstruction of the χ_{c0} and χ_{c2} through the hadronic channels by using TOF+TPC should be great.

For ψ', two different channels can be used to reconstruct it. The first one is the same as the J/ψ reconstruction: $\psi' \to e^+e^-$ or $\psi' \to \mu^+\mu^-$. The second one is $\psi' \to J/\psi\pi^+\pi^-$, $J/\psi \to e^+e^-$ or $J/\psi \to \mu^+\mu^-$. The BRs are list in Tab. 6.3. It is about

0.7% for the first channel and about 2% for the second channel. The second one maybe better since its $\Delta M = M_{\psi'} - M_{J/\psi} - 2M_{\pi} = 31$ MeV/c^2, thus give a very narrow mass peak and its resolution is insensitive to the momentum resolution of the daughter particles.

With the large acceptance of STAR, much higher luminosity of the RHICII and excellent PID capability of the combination of the TPC, TOF and EMC, it is a great chance to try to reconstruct these charmoinum states at STAR in high energy $p + p$ and heavy ion collisions to extend our understanding on the different charmonium states production mechanisms and the modifications from the cold and hot medium.

APPENDIX A

Presentations and Publication List

Presentations

- *J/ψ measurements at STAR*
  25th Winter Workshop on Nuclear Dynamics, Big Sky, Mentana, USA, 02/06/2009.

- *Quarkonia measurements in STAR*
  Understanding QGP through Spectra Functions and Euclidean Correlators (RIKEN BNL Research Center Workshop, Upton, New York, USA, 04/25/2008.

- *J/ψ production at high p_T in $p+p$ and Åcollisions at STAR*
  20th International Conference on Nucleus Nucleus Collisions (Quark Matter 2008), Jaipur, India, 02/09/2008.

- *High p_T J/ψ production in $p+p$ collisions at $\sqrt{s_{NN}}$ =200 GeV*
  2007 Annual Meeting of the Division of Nuclear Physics of the American Physical Society, Newport News, Virginia, USA, 10/12/2007.

- *Spin alignment of vector meson in heavy ion collisions at RHIC*
  International Workshop on Hadron Physics and Property of High Baryon Density Matter, Lanzhou, Shanxi, China, 11/24/2006

Publication List

- *Spin alignment measurements of the $K^\star$ and ϕ meson at RHIC*

B.I. Abelev *et al.* (STAR Collaboration), Phys. Rev. **C77**, 061902(R) (2008)
Principal Authors: Jinhui Chen, Xin Dong, Jingguo Ma, Ilya Selyuchankov, Zebo Tang.

- *J/ψ production at high p_T in $p+p$ and Åcollisions at STAR*
  Zebo Tang (for STAR Collaboration), J. Phys. G: Nucl. Part Phys. **35**, 104135 (2008)

- *R&D of the Endcap TOF Detector for BESIII*
  TANG Ze-bo, LI Xin, AN Shao-Hui CHEN Hong-Fang, HENG Yue-Kun, LI Cheng, SHAO Ming, SUN Yong-Jie, WANG Yi-Fang, WU Chong, ZENG Hui, ZHAO Li, ZHAO Xiao-Jian, HEP&NP 2006,**20(5)** 445

- *Spectra and radial flow at RHIC with Tsallis statistics in a Blast-Wave description*
  Zebo Tang, Yichun Xu, Lijuan Ruan, Gene van Buren, Fuqiang Wang, Zhangbu Xu, arXiv:0812.1609 (submitted to PRC(rapid communication))

- *Spin alignment of vector meson $K^{*0}(892)$ and $\phi(1020)$ in Au+Au and p+p collisions at $\sqrt{s_{NN}}$ =200 GeV*
  TANG Ze-bo (for STAR Collaboration), HEP&NP 2007, **31(12)** 1192

- *$K^{\star}(892)$ production in Au+Au collisions at RHIC*
  Xin Dong, Zebo Tang, Sadhana Dash, (for STAR Collaboration), IJMPE 2007,**16(7/8)** 2103-2109

- *Effect of light transmission characteristic of scintillator on the intrinsic time resolution of ETOF*
  LI Xin, TANG Ze-bo, CHEN Hong-Fang, LI Cheng, SHAO Ming, HEP&NP 2006,**30(10)** 1001

- *Upgrade of the calibration procedure for a STAR time-of-flight detector with new electronics*
  Ming Shao, Xin Dong, Zebo Tang, Yichun Xu, Min Huang, Cheng Li, Hongfang Chen, Yan Lv and Yifei Zhang, Meas. Sci. Technol. **20** (2009) 025102

- *Improvement of resonance reconstruction with time-of-flight detector at STAR experiment*

  Yichun Xu, Xin Dong, Ziping Zhang, Zebo Tang and Ming Shao, Nucl. Instr. & Meth. **A596** (2008) 186-189

- *Monte Carlo simulation of BESIII end-cap TOF*

  LI Xin, WU Chong, AN Shao-hui, TANG Ze-Bo, CHEN Hong-Fang, LI Cheng, HEP&NP 2005, **29(6)** 586

- *Study on MRPC-TOF timing properties and calibration methods*

  LI Liang, SHAO Ming, CHEN Hong-Fang, LI Cheng, TANG Ze-Bo, DONG Xin, WANG Xiao-Lian, HEP&NP, 2007,**31(06)** 576

- *Correlation between particle ionization energy loss in MRPC and its signal amplitude*

  LI Xin, SHAO Ming, LI Cheng, CHEN Hong-Fang, TANG Ze-Bo, HEP&NP, 2007,**31(04)** 377

- *Testing the time resolution of the BESIII end-cap TOF detectors*

  S. H. An, C. Li, M. Shao, Y. K. Heng, H. F. Chen, X. Li, Z. J. Sun, Z. B. Tang, C. Wu, Y. F. Wang, Meas. Sci. Technol. **17**(2006) 2650

- *New Prototype multi-gap resistive plate chambers with long strips*

  Y.J. Sun, C. Li, M. Shao, B. Gui, Y.E. Zhao, H.F. Chen, Z.B. Xu, L.J. Ruan, G.J. Lin, X. Wang, Y. Wang, Z.B. Tang, G. Eppley, P. Fachini, M. Kohl, J. Liu, W.J. Llope, R. Majka, T. Nussbaun, E. Ramberg, T. Sakuma, F. Simon, N. Smirnov, B. Surrow and D. Underwood, Nucl. Instr. & Meth. **A593** (2008) 307-313

- *Calibration of ionization energy loss at relativistic rise with STAR Time Projection Chamber*

  Yichun Xu, Olga Barannikova, Hans Bichsel, Xin Dong, Patricia Fachini, Yuri Fisyak, Adam Kocolosky, Bedanga Mohanty, Pawan Netrakanti, Lijuan Ruan,

Maria Cristina Suarez, Zebo Tang, Gene van Buren, Zhangbu Xu, arXiv:0807.4304 (submitted to Nucl. Instr. & Meth.)

- *Beam-Energy and System-Size Dependence of Dynamical Net Charge Fluctuations* B.I. Abelev et al., (STAR Collaboration), Phys.Rev.**C79**:024906 (2009), e-Print: arXiv:0807.3269

- *Indications of Conical Emission of Charged Hadrons at RHIC* B.I. Abelev et al., (STAR Collaboration), Phys.Rev.Lett.**102**:052302 (2009), e-Print: arXiv:0805.0622

- *Forward Neutral Pion Transverse Single Spin Asymmetries in p+p Collisions at* $\sqrt{s}$ *= 200 GeV.* B.I. Abelev et al., (STAR Collaboration), Phys.Rev.Lett.**101**:222001 (2008), e-Print: arXiv:0801.2990

- *Centrality dependence of charged hadron and strange hadron elliptic flow from* $\sqrt{s_{NN}}$ *= 200 GeV Au + Au collisions* B.I. Abelev et al., (STAR Collaboration), Phys.Rev.**C77**:054901 (2008), e-Print: arXiv:0801.3466

- ρ^0 *photoproduction in ultraperipheral relativistic heavy ion collisions at* $\sqrt{s_{NN}}$ *=200 GeV* B.I. Abelev et al., (STAR Collaboration), Phys.Rev.**C77**:034910 (2008), e-Print: arXiv:0712.3320

- *Enhanced strange baryon production in Au + Au collisions compared to p + p at* $\sqrt{s_{NN}}$ *= 200 GeV* B.I. Abelev et al., (STAR Collaboration), Phys.Rev.**C77**:044908 (2008), e-Print: arXiv:0705.2511

References

[Abe97] F. Abe et al. "J/ψ and $\psi(2S)$ production in $p\bar{p}$ collisions at $\sqrt{s} = 1.8$ TeV." *Phys. Rev. Lett.*, **79**:572–577, 1997.

[Abe02] K. Abe et al. "Observation of double c anti-c production in e+ e- annihilation at s**(1/2) approx. 10.6-GeV." *Phys. Rev. Lett.*, **89**:142001, 2002.

[Abe07] B. I. Abelev et al. "Transverse momentum and centrality dependence of high-pt non-photonic electron suppression in Au+Au collisions at $\sqrt{s_{NN}} =$ 200 GeV." *Phys. Rev. Lett.*, **98**:192301, 2007.

[Abe08a] B. I. Abelev et al. "Charmed hadron production at low transverse momentum in Au+Au collisions at RHIC." 2008.

[Abe08b] B. I. Abelev et al. "Systematic Measurements of Identified Particle Spectra in pp, d+Au and Au+Au Collisions from STAR." 2008.

[Abu07] A. Abulencia et al. "Polarization of J/ψ and ψ_{2S} mesons produced in $p\bar{p}$ collisions at $\sqrt{s} = 1.96$-TeV." *Phys. Rev. Lett.*, **99**:132001, 2007.

[Ack03] K. H. Ackermann et al. "The forward time projection chamber (FTPC) in STAR." *Nucl. Instrum. Meth.*, **A499**:713–719, 2003.

[ACL08] P. Artoisenet, John M. Campbell, J. P. Lansberg, F. Maltoni, and F. Tramontano. "υ Production at Fermilab Tevatron and LHC Energies." *Phys. Rev. Lett.*, **101**:152001, 2008.

[Aco05] Darin E. Acosta et al. "Measurement of the J/ψ meson and $b-$hadron production cross sections in $p\bar{p}$ collisions at $\sqrt{s} = 1960$ GeV." *Phys. Rev.*, **D71**:032001, 2005.

[Ada03] John Adams et al. "Transverse momentum and collision energy dependence of high p(T) hadron suppression in Au + Au collisions at ultrarelativistic energies." *Phys. Rev. Lett.*, **91**:172302, 2003.

[Ada05a] John Adams et al. "Distributions of charged hadrons associated with high transverse momentum particles in p p and Au + Au collisions at s(NN)**(1/2) = 200-GeV." *Phys. Rev. Lett.*, **95**:152301, 2005.

[Ada05b] John Adams et al. "Experimental and theoretical challenges in the search for the quark gluon plasma: The STAR collaboration's critical assessment of the evidence from RHIC collisions." *Nucl. Phys.*, **A757**:102–183, 2005.

[Ada05c] John Adams et al. "Open charm yields in d + Au collisions at s(NN)**(1/2) = 200-GeV." *Phys. Rev. Lett.*, **94**:062301, 2005.

[Ada05d] John Adams et al. "Pion, kaon, proton and anti-proton transverse momentum distributions from p + p and d + Au collisions at s(NN)**1/2 = 200-GeV." *Phys. Lett.*, **B616**:8–16, 2005.

[Ada06] John Adams et al. "Identified hadron spectra at large transverse momentum in p + p and d + Au collisions at s(NN)**(1/2) = 200-GeV." *Phys. Lett.*, **B637**:161–169, 2006.

[Ada07a] A. Adare et al. "J/ψ production versus transverse momentum and rapidity in p^+p collisions at $\sqrt{s}$ = 200-GeV." *Phys. Rev. Lett.*, **98**:232002, 2007.

[Ada07b] A. Adare et al. "J/ψ production vs centrality, transverse momentum, and rapidity in Au + Au collisions at $\sqrt{s_{NN}}$ = 200- GeV." *Phys. Rev. Lett.*, **98**:232301, 2007.

[Ada08] A. Adare et al. "J/ψ Production in $\sqrt{s_{NN}}$ = 200 GeV Cu+Cu Collisions." *Phys. Rev. Lett.*, **101**:122301, 2008.

[Adl04a] S. S. Adler et al. "J/ψ Production from Proton-Proton Collisions at $s = 200GeV$." *Phys. Rev. Lett.*, **92**(5):051802, Feb 2004.

[Adl04b] Stephen Scott Adler et al. "High p_T charged hadron suppression in Au + Au collisions at $\sqrt{s}_{NN}$ = 200 GeV." *Phys. Rev.*, **C69**:034910, 2004.

[AFK02] S. Anderson, V. V. Frolov, Y. Kubota, S. J. Lee, S. Z. Li, R. Poling, A. Smith, C. J. Stepaniak, J. Urheim, Z. Metreveli, K. K. Seth, A. Tomaradze, P. Zweber, S. Ahmed, M. S. Alam, L. Jian, M. Saleem, F. Wappler, E. Eckhart, K. K. Gan, C. Gwon, T. Hart, K. Honscheid, D. Hufnagel, H. Kagan, R. Kass, and T. K. Pedlar. "Measurements of Inclusive $B \to \psi$ Production." *Phys. Rev. Lett.*, **89**(28):282001, Dec 2002.

[Agg03] M. M. Aggarwal et al. "The STAR photon multiplicity detector." *Nucl. Instrum. Meth.*, **A499**:751–761, 2003.

[Ago03] S. Agostinelli et al. "GEANT4: A simulation toolkit." *Nucl. Instrum. Meth.*, **A506**:250–303, 2003.

[Aih88] H. Aihara et al. "Charged hadron inclusive cross-sections and fractions in e^+e^- annihiliation $\sqrt{s}$ = 29 GeV." *Phys. Rev. Lett.*, **61**:1263, 1988.

[Alb88] C. Albajar et al. "HIGH TRANSVERSE MOMENTUM J / psi PRODUCTION AT THE CERN PROTON - ANTI-PROTON COLLIDER." *Phys. Lett.*, **B200**:380, 1988.

[Alb89] H. Albrecht et al. "INCLUSIVE PRODUCTION OF CHARGED PIONS, CHARGED AND NEUTRAL KAONS AND ANTI-PROTONS IN e+ e- ANNIHILATION AT 10-GeV AND IN DIRECT UPSILON DECAYS." *Z. Phys.*, **C44**:547, 1989.

[Alb91] C. Albajar et al. "J / psi and psi-prime production at the CERN p anti-p collider." *Phys. Lett.*, **B256**:112–120, 1991.

[All03] C. E. Allgower et al. "The STAR endcap electromagnetic calorimeter." *Nucl. Instrum. Meth.*, **A499**:740–750, 2003.

[All06] John Allison et al. "Geant4 developments and applications." *IEEE Trans. Nucl. Sci.*, **53**:270, 2006.

[Alp75] B. Alper et al. "Production Spectra of pi+-, K+-, rho+- at Large Angles in Proton Proton Collisions in the CERN Intersecting Storage Rings." *Nucl. Phys.*, **B100**:237, 1975.

[Alv08] B. Alver et al. "System size dependence of two-particle angular correlations in p+p, Cu+Cu and Au+Au collisions." *J. Phys.*, **G35**:104142, 2008.

[Ams08] C. Amsler et al. "Review of particle physics." *Phys. Lett.*, **B667**:1, 2008.

[And03] M. Anderson et al. "The STAR time projection chamber: A unique tool for studying high multiplicity events at RHIC." *Nucl. Instrum. Meth.*, **A499**:659–678, 2003.

[Ang78] A. L. S. Angelis et al. "A Measurement of Inclusive pi0 Production at Large p(T) from p p Collisions at the CERN ISR." *Phys. Lett.*, **B79**:505–510, 1978.

[Ant79] D. Antreasyan et al. "Production of Hadrons at Large Transverse Momentum in 200- GeV, 300-GeV and 400-GeV p p and p n Collisions." *Phys. Rev.*, **D19**:764, 1979.

[Arn03] L. Arnold et al. "The STAR silicon strip detector (SSD)." *Nucl. Instrum. Meth.*, **A499**:652–658, 2003.

[AV07] Azfar Adil and Ivan Vitev. "Collisional dissociation of heavy mesons in dense QCD matter." *Phys. Lett.*, **B649**:139–146, 2007. and I. Vitev private communication.

[Ban82] M. Banner et al. "INCLUSIVE pi0 PRODUCTION AT THE CERN p anti-p COLLIDER." *Phys. Lett.*, **B115**:59, 1982.

[BBG72] Richard Blankenbecler, Stanley J. Brodsky, and J. F. Gunion. "Inclusive Processes at High Transverse Momentum." *Phys. Lett.*, **B42**:461, 1972.

[BBK71] S. M. Berman, J. D. Bjorken, and John B. Kogut. "Inclusive Processes at High Transverse Momentum." *Phys. Rev.*, **D4**:3388, 1971.

[Bed03] M. Beddo et al. "The STAR barrel electromagnetic calorimeter." *Nucl. Instrum. Meth.*, **A499**:725–739, 2003.

[Bel03] R. Bellwied et al. "The STAR silicon vertex tracker: A large area silicon drift detector." *Nucl. Instrum. Meth.*, **A499**:640–651, 2003.

[Ber03] F. Bergsma et al. "The STAR detector magnet subsystem." *Nucl. Instrum. Meth.*, **A499**:633–639, 2003.

[BJ81] Edmond L. Berger and Daniel L. Jones. "Inelastic Photoproduction of J/psi and Upsilon by Gluons." *Phys. Rev.*, **D23**:1521–1530, 1981.

[BO87] J. P. Blaizot and Jean-Yves Ollitrault. "J / PSI MOMENTUM DISTRIBUTION AND LIFETIME OF A QUARK - GLUON PLASMA." *Phys. Lett.*, **B199**:499–503, 1987.

[BR81] R. Baier and R. Ruckl. "Hadronic Production of J/psi and Upsilon: Transverse Momentum Distributions." *Phys. Lett.*, **B102**:364, 1981.

[Bra04] N. Brambilla et al. "Heavy quarkonium physics." 2004.

[Bus95] D. Buskulic et al. "Inclusive pi+-, K+- and (p, anti-p) differential cross-sections at the Z resonance." *Z. Phys.*, **C66**:355–366, 1995.

[Cla78] A. G. Clark et al. "INCLUSIVE pi0 PRODUCTION FROM HIGH-ENERGY P P COLLISIONS AT VERY LARGE TRANSVERSE MOMENTA." *Phys. Lett.*, **B74**:267, 1978.

[CLN04] Fred Cooper, Ming X. Liu, and Gouranga C. Nayak. "J/ψ production in pp collisions at $\sqrt{s}$ = 200-GeV at RHIC." *Phys. Rev. Lett.*, **93**:171801, 2004.

[CNV05] Matteo Cacciari, Paolo Nason, and Ramona Vogt. "QCD predictions for charm and bottom production at RHIC." *Phys. Rev. Lett.*, **95**:122001, 2005.

[Cos08] Mauro R. Cosentino. "J/ψ production in $p + p$ collisions at $\sqrt{s_{NN}}$ =200GeV in the STAR experiment." 2008.

[CPR02] T. M. Cormier, A. I. Pavlinov, M. V. Rykov, V. L. Rykov, and K. E. Shestermanov. "STAR Barrel Electromagnetic Calorimeter absolute calibration using 'minimum ionizing particles' from collisions at RHIC." *Nucl. Instrum. Meth.*, **A483**:734–746, 2002.

[Don] Weijiang Dong. "Measurement of non-photonic electron azimuthal anisotropy nu(s) from Au+Au collisions at s(NN)**(1/2) = 200-GeV." UMI-32-26018.

[Don06] Xin Dong. "The time-Of-flight detector for RHIC / STAR and the related physics." *AIP Conf. Proc.*, **865**:332–337, 2006.

[EF84] Svante Ekelin and Sverker Fredriksson. "LARGE P(T) PROTONS FROM CONSTITUENT DIQUARK SCATTERING." *Phys. Lett.*, **B149**:509, 1984.

[FG72] Harald Fritzsch and Murray Gell-Mann. "Current algebra: Quarks and what else?" *eConf*, **C720906V2**:135–165, 1972.

[Gon] Johan Enmanuel Gonzalez. "J/ψ production in Au + Au collisions at center of mass energy = 200-GeV." UMI-32-35748.

[Gun08] T. Gunji. "Onset of J/ψ melting in quark-gluon fluid at RHIC." *J. Phys.G: Nucl. Part. Phys.*, **35**:104137, 2008.

[HLO03] M. Harrison, T. Ludlam, and S. Ozaki. "RHIC project overview." *Nucl. Instrum. Meth.*, **A499**:235–244, 2003.

[Hor08] Donald Hornback. "Measurements of heavy quark production via single leptons at PHENIX." *J. Phys.*, **G35**:104113, 2008.

[JC09] F. Jin and for the STAR Collaboration. "Measurement of Non-photonic Electrons in p + p Collisions at $\sqrt{s_{NN}} = 200$ GeV with reduced detector material in STAR." 2009.

[Kap08] Jan Kapitan. "Open charm measurement with HFT at STAR." 2008.

[Kha08a] Dmitri Kharzeev et al. "Gluon saturation effects on J/Psi production in heavy ion collisions." 2008.

[Kha08b] Dmitri Kharzeev et al. "J/Psi production in heavy ion collisions and gluon saturation." 2008.

[KKS06] F. Karsch, D. Kharzeev, and H. Satz. "Sequential charmonium dissociation." *Phys. Lett.*, **B637**:75–80, 2006.

[KLP01] F. Karsch, E. Laermann, and A. Peikert. "Quark mass and flavor dependence of the QCD phase transition." *Nucl. Phys.*, **B605**:579–599, 2001.

[Kou80] C. Kourkoumelis et al. "CHARACTERISTICS OF J / psi AND UPSILON PRODUCTION AT THE CERN INTERSECTING STORAGE RINGS." *Phys. Lett.*, **B91**:481, 1980.

[Lan08] J. P. Lansberg. "On the mechanisms of heavy-quarkonium hadroproduction." 2008.

[Lin07] Xiao-yan Lin. "The first measurement of B meson semi-leptonic decay contribution to non-photonic electrons at RHIC." *J. Phys.*, **G34**:S821–826, 2007.

[Llo05] W. J. Llope. "The large-area time-of-flight upgrade for STAR." *Nucl. Instrum. Meth.*, **B241**:306–310, 2005.

[Lon] Hui Long. "Midrapidity lambda and antilambda production in Au+Au collisions at the Relativistic Heavy Ion Collider." UMI-30-63922.

[LRU07] H. Liu, K. Rajagopal, and U.A.Wiedemann. *Phys. Rev. Lett.*, **98**:182301, 2007.

[NLC03] Gouranga C. Nayak, Ming X. Liu, and Fred Cooper. "Color octet contribution to high $p_T J/\psi$ production in pp collisions at $\sqrt{s} = 500$-GeV and 200-GeV at RHIC." *Phys. Rev.*, **D68**:034003, 2003.

[Oda08] Susumu X. Oda. "J/psi production at RHIC-PHENIX." *J. Phys.*, **G35**:104134, 2008.

[ORG78] J. F. Owens, E. Reya, and M. Gluck. "Detailed Quantum Chromodynamic Predictions for High p(T) Processes." *Phys. Rev.*, **D18**:1501, 1978.

[Pak04] P. Pakhlov. "Further study of double charmonium production in e+ e- annihilation at Belle." 2004.

[Rua08] Lijuan Ruan. "Prototype Performance of Novel Muon Telescope Detector at STAR." 2008.

[Sha06] M. Shao et al. "Extensive particle identification with TPC and TOF at the STAR experiment." *Nucl. Instrum. Meth.*, **A558**:419–429, 2006.

[Sha07] A. Shabetai. "The HFT, a Heavy Flavor Tracker for STAR." *Eur. Phys. J.*, **C49**:169–175, 2007.

[Sil08] Catherine Silvestre. "PHENIX first measurement of the J/psi elliptic flow parameter v2 in Au+Au collisions at sqrt(sNN) = 200 GeV." *J. Phys.*, **G35**:104136, 2008.

[Sim08] F. Simon et al. "The Forward GEM Tracker of STAR at RHIC." 2008.

[SMS06] Torbjorn Sjostrand, Stephen Mrenna, and Peter Skands. "PYTHIA 6.4 physics and manual." *JHEP*, **05**:026, 2006.

[Sun08] Y. J. Sun et al. "New Prototype Multi-gap Resistive Plate Chambers with Long Strips." *Nucl. Instrum. Meth.*, **A593**:307–313, 2008.

[Vog05] R. Vogt. "Shadowing and absorption effects on J/psi production in d A collisions." *Phys. Rev.*, **C71**:054902, 2005.

[VPS08] Sergei A. Voloshin, Arthur M. Poskanzer, and Raimond Snellings. "Collective phenomena in non-central nuclear collisions." 2008.

[Wan08] Gang Wang. "Non-photonic electron-hadron correlations at STAR." *J. Phys.*, **G35**:104107, 2008.

[Wic07] Simon Wicks et al. "Elastic, Inelastic, and Path Length Fluctuations in Jet Tomography." *Nucl. Phys.*, **A784**:426–442, 2007. and W. A. Horowitz private communication.

[Xu08] Yi-chun Xu et al. "Calibration of ionization energy loss at relativistic rise with STAR Time Projection Chamber." 2008.

[ZR07] Xingbo Zhao and Ralf Rapp. "Transverse Momentum Spectra of J/ψ in Heavy-Ion Collisions." 2007.